

To be published in the proceedings of the Advanced Study Institute on *Mesoscopic Electron Transport*, edited by L.L. Sohn, L.P. Kouwenhoven, G. Schön (Kluwer 1997).

## **ELECTRON TRANSPORT IN QUANTUM DOTS.**

LEO P. KOUWENHOVEN,<sup>1</sup> CHARLES M. MARCUS,<sup>2</sup>  
PAUL L. MCEUEN,<sup>3</sup> SEIGO TARUCHA,<sup>4</sup> ROBERT M.  
WESTERVELT,<sup>5</sup> AND NED S. WINGREEN<sup>6</sup> (*alphabetical order*).

1. *Department of Applied Physics, Delft University of Technology, P.O.Box 5046, 2600 GA Delft, The Netherlands.*
2. *Department of Physics, Stanford University, Stanford, CA 94305, USA*
3. *Department of Physics, University of California and Materials Science Division, Lawrence Berkeley Laboratory, Berkeley, CA 94720, USA.*
4. *NTT Basic Research Laboratories, 3-1 Morinosoto Wakamiya, Atsugi-shi, Kanagawa 243-01, Japan.*
5. *Division of Applied Sciences and Department of Physics, Harvard University, Cambridge, Massachusetts 02138, USA.*
6. *NEC Research Institute, 4 Independence Way, Princeton, NJ 08540, USA*

### **1. Introduction**

The ongoing miniaturization of solid state devices often leads to the question: “How small can we make resistors, transistors, etc., without changing the way they work?” The question can be asked a different way, however: “How small do we have to make devices in order to get fundamentally new properties?” By “new properties” we particularly mean those that arise from quantum mechanics or the quantization of charge in units of  $e$ ; effects that are only important in small systems such as atoms. “What kind of small electronic devices do we have in mind?” Any sort of clustering of atoms that can be connected to source and drain contacts and whose properties can be regulated with a gate electrode. Practically, the clustering of atoms may be a molecule, a small grain of metallic atoms, or an electronic device that is made with modern chip fabrication techniques. It turns out that such seemingly different structures have quite similar transport properties and that one can explain their physics within one relatively simple framework. In this paper we investigate the physics of electron transport through such small systems.

One type of artificially fabricated device is a quantum dot. Typically, quantum dots are small regions defined in a semiconductor material with a size of order 100 nm [1]. Since the first studies in the late eighties, the physics of quantum dots has been a very active and fruitful research topic. These dots have proven to be useful systems to study a wide range of physical phenomena. We discuss here in separate sections the physics of artificial atoms, coupled quantum systems, quantum chaos, the quantum Hall effect, and time-dependent quantum mechanics as they are manifested in quantum dots. In recent electron transport experiments it has been shown that the same physics also occurs in molecular systems and in small metallic grains. In section 9, we comment on these other nm-scale devices and discuss possible applications.

The name “dot” suggests an exceedingly small region of space. A semiconductor quantum dot, however, is made out of roughly a million atoms with an equivalent number of electrons. Virtually all electrons are tightly bound to the nuclei of the material, however, and the number of free electrons in the dot can be very small; between one and a few hundred. The deBroglie wavelength of these electrons is comparable to the size of the dot, and the electrons occupy discrete quantum levels (akin to atomic orbitals in atoms) and have a discrete excitation spectrum. A quantum dot has another characteristic, usually called the charging energy, which is analogous to the ionization energy of an atom. This is the energy required to add or remove a single electron from the dot. Because of the analogies to real atoms, quantum dots are sometimes referred to as artificial atoms [2]. The atom-like physics of dots is studied not via their interaction with light, however, but instead by measuring their transport properties, that is, by their ability to carry an electric current. Quantum dots are therefore artificial atoms with the intriguing possibility of attaching current and voltage leads to probe their atomic states.

This chapter reviews many of the main experimental and theoretical results reported to date on electron transport through semiconductor quantum dots. We note that other reviews also exist [3]. For theoretical reviews we refer to Averin and Likharev [4] for detailed transport theory; Ingold and Nazarov [5] for the theory of metallic and superconducting systems; and Beenakker [6] and van Houten, Beenakker and Staring [7] for the single electron theory of quantum dots. Recent reviews focused on quantum dots are found in Refs. 8 and 9. Collections of single electron papers can be found in Refs. 10 and 11. For reviews in popular science magazines see Refs. 1, 2, 12-15.

The outline of this chapter is as follows. In the remainder of this section we summarize the conditions for charge and energy quantization effects and we briefly review the history of quantum dots and describe fabrication and measurement methods. A simple theory of electron transport through dots is outlined in section 2. Section 3 presents basic single electron experiments. In

section 4 we discuss the physics of multiple dot systems; e.g. dots in series, dots in parallel, etc. Section 5 describes vertical dots where the regime of very few electrons (0, 1, 2, 3, etc.) in the dot has been studied. In section 6 we return to lateral dots and discuss mesoscopic fluctuations in quantum dots. Section 7 describes the high magnetic field regime where the formation of Landau levels and many-body effects dominate the physics. What happens in dots at very short time scales or high frequencies is discussed in section 8. Finally, applications and future directions are summarized in section 9. We note that sections 2 and 3 serve as introductions and that the other sections can be read independently.

### 1.1. QUANTIZED CHARGE TUNNELING.

In this section we examine the circumstances under which Coulomb charging effects are important. In other words, we answer the question, “How small and how cold should a conductor be so that adding or subtracting a single electron has a measurable effect?” To answer this question, let us consider the electronic properties of the small conductor depicted in Fig. 1.1(a), which is coupled to three terminals. Particle exchange can occur with only two of the terminals, as indicated by the arrows. These source and drain terminals connect the small conductor to macroscopic current and voltage meters. The third terminal provides an electrostatic or capacitive coupling and can be used as a gate electrode. If we first assume that there is no coupling to the source and drain contacts, then our small conductor acts as an island for electrons.

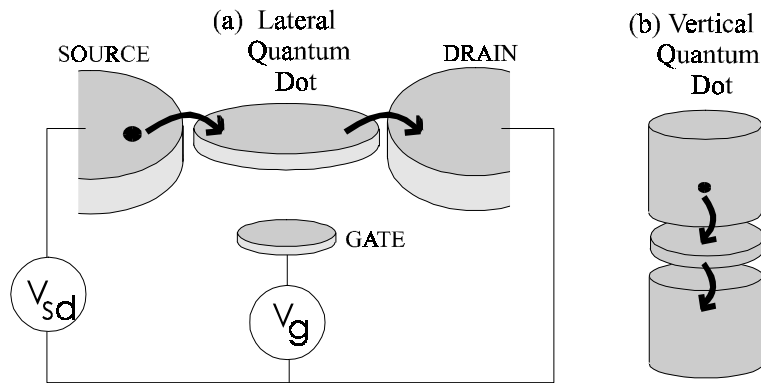


Figure 1.1. Schematic of a quantum dot, in the shape of a disk, connected to source and drain contacts by tunnel junctions and to a gate by a capacitor. (a) shows the lateral geometry and (b) the vertical geometry.

The number of electrons on this island is an integer  $N$ , i.e. the charge on the island is quantized and equal to  $Ne$ . If we now allow tunneling to the source and drain electrodes, then the number of electrons  $N$  adjusts itself until the energy of the whole circuit is minimized.

When tunneling occurs, the charge on the island suddenly changes by the quantized amount  $e$ . The associated change in the Coulomb energy is conveniently expressed in terms of the capacitance  $C$  of the island. An extra charge  $e$  changes the electrostatic potential by the charging energy  $E_C = e^2/C$ . This charging energy becomes important when it exceeds the thermal energy  $k_B T$ . A second requirement is that the barriers are sufficiently opaque such that the electrons are located either in the source, in the drain, or on the island. This means that quantum fluctuations in the number  $N$  due to tunneling through the barriers is much less than one over the time scale of the measurement. (This time scale is roughly the electron charge divided by the current.) This requirement translates to a lower bound for the tunnel resistances  $R_t$  of the barriers. To see this, consider the typical time to charge or discharge the island  $\Delta t = R_t C$ . The Heisenberg uncertainty relation:  $\Delta E \Delta t = (e^2/C) R_t C > h$  implies that  $R_t$  should be much larger than the resistance quantum  $h/e^2 = 25.813 \text{ k}\Omega$  in order for the energy uncertainty to be much smaller than the charging energy. To summarize, the two conditions for observing effects due to the discrete nature of charge are [3,4]:

$$R_t \gg h/e^2 \quad (1.1a)$$

$$e^2/C \gg k_B T \quad (1.1b)$$

The first criterion can be met by weakly coupling the dot to the source and drain leads. The second criterion can be met by making the dot small. Recall that the capacitance of an object scales with its radius  $R$ . For a sphere,  $C = 4\pi\epsilon_r\epsilon_0 R$ , while for a flat disc,  $C = 8\epsilon_r\epsilon_0 R$ , where  $\epsilon_r$  is the dielectric constant of the material surrounding the object.

While the tunneling of a single charge changes the electrostatic energy of the island by a discrete value, a voltage  $V_g$  applied to the gate (with capacitance  $C_g$ ) can change the island's electrostatic energy in a continuous manner. In terms of charge, tunneling changes the island's charge by an integer while the gate voltage induces an effective continuous charge  $q = C_g V_g$  that represents, in some sense, the charge that the dot would like to have. This charge is continuous even on the scale of the elementary charge  $e$ . If we sweep  $V_g$  the build up of the induced charge will be compensated in periodic intervals by tunneling of discrete charges onto the dot. This competition between continuously induced charge and discrete compensation leads to so-called

*Coulomb oscillations* in a measurement of the current as a function of gate voltage at a fixed source-drain voltage.

An example of a measurement [16] is shown in Fig. 1.2(a). In the valley of the oscillations, the number of electrons on the dot is fixed and necessarily equal to an integer  $N$ . In the next valley to the right the number of electrons is increased to  $N+1$ . At the crossover between the two stable configurations  $N$  and  $N+1$ , a "charge degeneracy" [17] exists where the number can alternate between  $N$  and  $N+1$ . This allowed fluctuation in the number (i.e. according to the sequence  $N \rightarrow N+1 \rightarrow N \rightarrow \dots$ ) leads to a current flow and results in the observed peaks.

An alternative measurement is performed by fixing the gate voltage, but varying the source-drain voltage  $V_{sd}$ . As shown in Fig. 1.2(b) [18] one observes in this case a non-linear current-voltage characteristic exhibiting a *Coulomb staircase*. A new current step occurs at a threshold voltage ( $\sim e^2/C$ ) at which an extra electron is energetically allowed to enter the island. It is seen in Fig. 1.2(b) that the threshold voltage is periodic in gate voltage, in accordance with the Coulomb oscillations of Fig. 1.2(a).

## 1.2. ENERGY LEVEL QUANTIZATION.

Electrons residing on the dot occupy quantized energy levels, often denoted as OD-states. To be able to resolve these levels, the energy level spacing  $\Delta E \gg k_B T$ . The level spacing at the Fermi energy  $E_F$  for a box of size  $L$  depends on

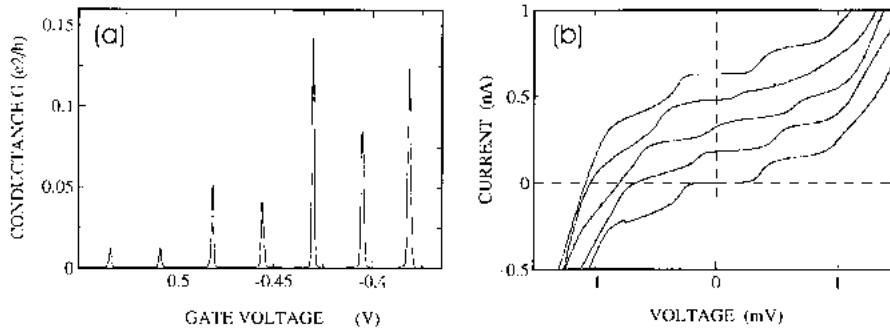


Figure 1.2(a). An example of a measurement of Coulomb oscillations to illustrate the effect of single electron charges on the macroscopic conductance. The conductance is the ratio  $I/V_{sd}$  and the period in gate voltage  $V_g$  is about  $e/C_g$ . (From Nagamune *et al.* [16].) (b) An example of a measurement of the Coulomb staircase in  $I-V_{sd}$  characteristics. The different curves have an offset for clarity ( $I = 0$  occurs at  $V_{sd} = 0$ ) and are taken for five different gate voltages to illustrate periodicity in accordance with the oscillations shown in (a). (From Kouwenhoven *et al.* [18].)

the dimensionality. Including spin degeneracy, we have:

$$\Delta E = (N/4)\hbar^2\pi^2/mL^2 \quad 1\text{D} \quad (1.2a)$$

$$= (1/\pi)\hbar^2\pi^2/mL^2 \quad 2\text{D} \quad (1.2b)$$

$$= (1/3\pi^2 N)^{1/3}\hbar^2\pi^2/mL^2 \quad 3\text{D} \quad (1.2c)$$

The characteristic energy scale is thus  $\hbar^2\pi^2/mL^2$ . For a 1D box, the level spacing grows for increasing  $N$ , in 2D it is constant, while in 3D it decreases as  $N$  increases. The level spacing of a 100 nm 2D dot is  $\sim 0.03$  meV, which is large enough to be observable at dilution refrigerator temperatures of  $\sim 100$  mK  $= \sim 0.0086$  meV. Electrons confined at a semiconductor hetero interface can effectively be two-dimensional. In addition, they have a small effective mass that further increases the level spacing. As a result, dots made in semiconductor heterostructures are true artificial atoms, with both observable quantized charge states and quantized energy levels. Using 3D metals to form a dot, one needs to make dots as small as  $\sim 5$  nm in order to observe atom-like properties. We come back to metallic dots in section 9.

The fact that the quantization of charge and energy can drastically influence transport through a quantum dot is demonstrated by the Coulomb oscillations in Fig. 1.2(a) and the Coulomb staircase in Fig. 1.2(b). Although we have not yet explained these observations in detail (see section 2), we note that one can obtain spectroscopic information about the charge state and energy levels of the dot by analyzing the precise shape of the Coulomb oscillations and the Coulomb staircase. In this way, single electron transport can be used as a spectroscopic tool.

### 1.3. HISTORY, FABRICATION, AND MEASUREMENT TECHNIQUES.

Single electron quantization effects are really nothing new. In his famous 1911 experiments, Millikan [19] observed the effects of single electrons on the falling rate of oil drops. Single electron tunneling was first studied in solids in 1951 by Gorter [20], and later by Giaever and Zeller in 1968 [21], and Lambe and Jaklevic in 1969 [22]. These pioneering experiments investigated transport through thin films consisting of small grains. A detailed transport theory was developed by Kulik and Shekhter in 1975 [23]. Much of our present understanding of single electron charging effects was already developed in these early works. However, a drawback was the averaging effect over many grains and the limited control over device parameters. Rapid progress in device control was made in the mid 80's when several groups began to fabricate small systems using nanolithography and thin-film processing. The new

technological control, together with new theoretical predictions by Likharev [24] and Mullen *et al.* [25], boosted interest in single electronics and led to the discovery of many new transport phenomena. The first clear demonstration of controlled single electron tunneling was performed by Fulton and Dolan in 1987 [26] in an aluminum structure similar to the one in Fig. 1(a). They observed that the macroscopic current through the two junction system was extremely sensitive to the charge on the gate capacitor. These are the so-called Coulomb oscillations. This work also demonstrated the usefulness of such a device as a *single-electrometer*, i.e. an electrometer capable of measuring single charges. Since these early experiments there have been many successes in the field of metallic junctions which are reviewed in other chapters of this volume.

The advent of the scanning tunneling microscope (STM) [27] has renewed interest in Coulomb blockade in small grains. STMs can both image the topography of a surface and measure local current-voltage characteristics on an atomic distance scale. The charging energy of a grain of size  $\sim 10$  nm can be as large as 100 meV, so that single electron phenomena occur up to room temperature in this system [28]. These charging energies are 10 to 100 times larger than those obtained in artificially fabricated Coulomb blockade devices. However, it is difficult to fabricate these naturally formed structures in self-designed geometries (e.g. with gate electrodes, tunable barriers, etc.). There have been some recent successes [29,30] which we discuss in section 9.

Effects of quantum confinement on the electronic properties of semiconductor heterostructures were well known prior to the study of quantum dots. Growth techniques such as molecular beam epitaxy, allows fabrication of quantum wells and heterojunctions with energy levels that are quantized along the growth ( $z$ ) direction. For proper choice of growth parameters, the electrons are fully confined in the  $z$ -direction (i.e. only the lowest 2D eigenstate is occupied by electrons). The electron motion is free in the  $x$ - $y$  plane. This forms a two dimensional electron gas (2DEG).

Quantum dots emerge when this growth technology is combined with electron-beam lithography to produce confinement in all three directions. Some of the earliest experiments were on GaAs/AlGaAs resonant tunneling structures etched to form sub-micron pillars. These pillars are called vertical quantum dots because the current flows along the  $z$ -direction [see for example Fig. 1.1(b)]. Reed *et al.* [31] found that the  $I$ - $V$  characteristics reveal structure that they attributed to resonant tunneling through quantum states arising from the lateral confinement.

At the same time as the early studies on vertical structures, gated AlGaAs devices were being developed in which the transport is entirely in the plane of the 2DEG [see Fig. 1.1(a)]. The starting point for these devices is a 2DEG at

the interface of a GaAs/AlGaAs heterostructure. The only mobile electrons at low temperature are confined at the GaAs/AlGaAs interface, which is typically  $\sim 100$  nm below the surface. Typical values of the 2D electron density are  $n_s \sim (1 - 5) \cdot 10^{15} \text{ m}^{-2}$ . To define the small device, metallic gates are patterned on the surface of the wafer using electron beam lithography [32]. Gate features as small as 50 nm can be routinely written. Negative voltages applied to metallic surface gates define narrow wires or tunnel barriers in the 2DEG. Such a system is very suitable for quantum transport studies for two reasons. First, the wavelength of electrons at the Fermi energy is  $\lambda_F = (2\pi/n_s)^{1/2} \sim (80 - 30)$  nm, roughly 100 times larger than in metals. Second, the mobility of the 2DEG can be as large as  $1000 \text{ m}^2\text{V}^{-1}\text{s}^{-1}$ , which corresponds to a transport elastic mean free path of order 100  $\mu\text{m}$ . This technology thus allows fabrication of devices which are much smaller than the mean free path; electron transport through the device is *ballistic*. In addition, the device dimensions can be comparable to the electron wavelength, so that quantum confinement is important. The observation of quantized conductance steps in short wires, or quantum point contacts, demonstrated quantum confinement in two spatial directions [33,34]. Later work on different gate geometries led to the discovery of a wide variety of mesoscopic transport phenomena [35]. For instance, coherent resonant transmission was demonstrated through a quantum dot [36] and through an array of quantum dots [37]. These early dot experiments were performed with barrier conductances of order  $e^2/h$  or larger, so that the effects of charge quantization were relatively weak.

The effects of single-electron charging were first reported in semiconductors in experiments on narrow wires by Scott-Thomas *et al.* [38]. With an average conductance of the wire much smaller than  $e^2/h$ , their measurements revealed a periodically oscillating conductance as a function of a voltage applied to a nearby gate. It was pointed out by van Houten and Beenakker [39], along with Glazman and Shekhter [17], that these oscillations arise from single electron charging of a small segment of the wire, delineated by impurities. This pioneering work on “accidental dots” [38,40-43] stimulated the study of more controlled systems.

The most widely studied type of device is a lateral quantum dot defined by metallic surface gates. Fig. 1.3 shows an SEM micrograph of a typical device [44]. The tunnel barriers between the dot and the source and drain 2DEG regions can be tuned using the left and right pair of gates. The dot can be squeezed to smaller size by applying a potential to the center pair of gates. Similar gated dots, with lithographic dimensions ranging from a few  $\mu\text{m}$  down to  $\sim 0.3 \mu\text{m}$ , have been studied by a variety of groups. The size of the dot formed in the 2DEG is somewhat smaller than the lithographic size, since the 2DEG is typically depleted 100 nm away from the gate.

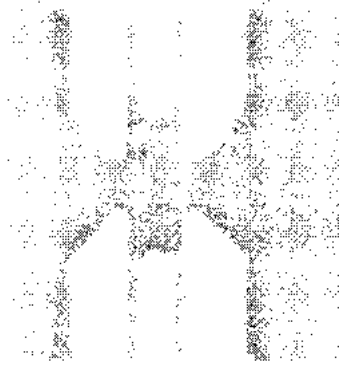


Figure 1.3. A scanning electron microscope (SEM) photo of a typical lateral quantum dot device (600 x 300 nm) defined in a GaAs/AlGaAs heterostructure. The 2DEG is ~100 nm below the surface. Negative voltages applied to the surface gates (i.e. the light areas) deplete the 2DEG underneath. The resulting dot contains a few electrons which are coupled via tunnel barriers to the large 2DEG regions. The tunnel barriers and the size of the dot can be tuned individually with the voltages applied to the left/right pair of gates and to the center pair, respectively. (From Oosterkamp *et al.* [44].)

We can estimate the charging energy  $e^2/C$  and the quantum level spacing  $\Delta E$  from the dimensions of the dot. The total capacitance  $C$  (i.e. the capacitance between the dot and all other pieces of metal around it, plus contributions from the self-capacitance) should in principle be obtained from self-consistent calculations [45-47]. A quick estimate can be obtained from the formula given previously for an isolated 2D metallic disk, yielding  $e^2/C = e^2/(8\epsilon_r\epsilon_0R)$  where  $R$  is the disk radius and  $\epsilon_r = 13$  in GaAs. For example, for a dot of radius 200 nm, this yields  $e^2/C = 1$  meV. This is really an upper limit for the charging energy, since the presence of the metal gates and the adjacent 2DEG increases  $C$ . An estimate for the single particle level spacing can be obtained from Eq. 1.2(b),  $\Delta E = \hbar^2/m^*R^2$ , where  $m^* = 0.067m_e$  is the effective mass in GaAs, yielding  $\Delta E = 0.03$  meV.

To observe the effects of these two energy scales on transport, the thermal energy  $k_B T$  must be well below the energy scales of the dot. This corresponds to temperatures of order 1 K ( $k_B T = 0.086$  meV at 1K). As a result, most of the transport experiments have been performed in dilution refrigerators with base temperatures in the 10 - 50 mK range. The measurement techniques are fairly standard, but care must be taken to avoid spurious heating of the electrons in the device. Since it is a small, high resistance object, very small noise levels can cause significant heating. With reasonable precautions (e.g. filtering at low

temperature, screened rooms, etc.), effective electron temperatures in the 50 - 100 mK range can be obtained.

It should be noted that other techniques like far-infrared spectroscopy on arrays of dots [48] and capacitance measurements on arrays of dots [49] and on single dots [50] have also been employed. Infrared spectroscopy probes the collective plasma modes of the system, yielding very different information than that obtained by transport. Capacitance spectroscopy, on the other hand, yields nearly identical information, since the change in the capacitance due to electron tunneling on and off a dot is measured. Results from this single-electron capacitance spectroscopy technique are presented in sections 5 and 7.

## 2. Basic theory of electron transport through quantum dots.

This section presents a theory of transport through quantum dots that incorporates both single electron charging and energy level quantization. We have chosen a rather simple description which still explains most experiments. We follow Korotkov *et al.* [51], Meir *et al.* [52], and Beenakker [6], who generalized the charging theory for metal systems to include 0D-states. This section is split up into parts that separately discuss (2.1) the period of the Coulomb oscillations, (2.2) the amplitude and lineshape of the Coulomb oscillations, (2.3) the Coulomb staircase, and (2.4) related theoretical work.

### 2.1. PERIOD OF COULOMB OSCILLATIONS.

Fig. 2.1(a) shows the potential landscape of a quantum dot along the transport direction. The states in the leads are filled up to the electrochemical potentials  $\mu_{left}$  and  $\mu_{right}$  which are connected via the externally applied source-drain voltage  $V_{sd} = (\mu_{left} - \mu_{right})/e$ . At zero temperature (and neglecting co-tunneling [53]) transport occurs according to the following rule: *current is (non) zero when the number of available states on the dot in the energy window between  $\mu_{left}$  and  $\mu_{right}$  is (non) zero*. The number of available states follows from calculating the electrochemical potential  $\mu_{dot}(N)$ . This is, by definition, the minimum energy for adding the  $N$ th electron to the dot:  $\mu_{dot}(N) \equiv U(N) - U(N-1)$ , where  $U(N)$  is the total ground state energy for  $N$  electrons on the dot at zero temperature.

To calculate  $U(N)$  from first principles is quite difficult. To proceed, we make several assumptions. First, we assume that the quantum levels can be calculated independently of the number of electrons on the dot. Second, we parameterize the Coulomb interactions among the electrons in the dot and between electrons in the dot and those somewhere else in the environment (as

in the metallic gates or in the 2DEG leads) by a capacitance  $C$ . We further assume that  $C$  is independent of the number of electrons on the dot. This is a reasonable assumption as long as the dot is much larger than the screening length (i.e. no electric fields exist in the interior of the dot). We can now think of the Coulomb interactions in terms of the circuit diagram shown in Fig. 2.2. Here, the total capacitance  $C = C_l + C_r + C_g$  consists of capacitances across the barriers,  $C_l$  and  $C_r$ , and a capacitance between the dot and gate,  $C_g$ . This simple model leads in the linear response regime (i.e.  $V_{sd} \ll \Delta E/e$ ,  $e/C$ ) to an electrochemical potential  $\mu_{dot}(N)$  for  $N$  electrons on the dot [18]:

$$\mu_{dot}(N) = E_N + \frac{(N - N_0 - 1/2) e^2}{C} - e \frac{C_g}{C} V_g \quad (2.1)$$

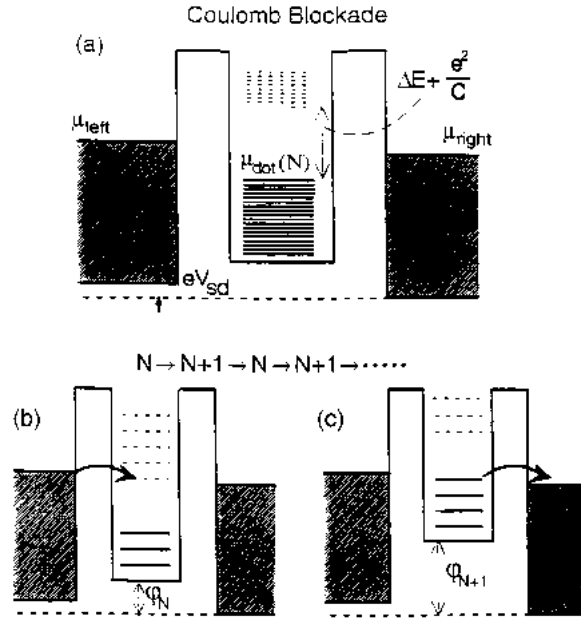


Figure 2.1. Potential landscape through a quantum dot. The states in the 2D reservoirs are filled up to the electrochemical potentials  $\mu_{left}$  and  $\mu_{right}$  which are related via the external voltage  $V_{sd} = (\mu_{left} - \mu_{right})/e$ . The discrete 0D-states in the dot are filled with  $N$  electrons up to  $\mu_{dot}(N)$ . The addition of one electron to the dot would raise  $\mu_{dot}(N)$  (i.e. the highest solid line) to  $\mu_{dot}(N+1)$  (i.e. the lowest dashed line). In (a) this addition is blocked at low temperature. In (b) and (c) the addition is allowed since here  $\mu_{dot}(N+1)$  is aligned with the reservoir potentials  $\mu_{left}$ ,  $\mu_{right}$  by means of the gate voltage. (b) and (c) show two parts of the sequential tunneling process at the same gate voltage. (b) shows the situation with  $N$  and (c) with  $N+1$  electrons on the dot.

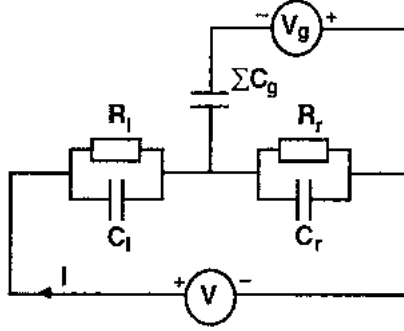


Figure 2.2. Circuit diagram in which the tunnel barriers are represented as a parallel capacitor and resistor. The different gates are represented by a single capacitor  $\Sigma C_g$ . The charging energy in this circuit is  $e^2/(C_l + C_r + \Sigma C_g)$ .

This is of the general form  $\mu_{dot}(N) = \mu_{ch}(N) + e\phi_N$ , i.e. the *electrochemical* potential is the sum of the *chemical* potential  $\mu_{ch}(N) = E_N$ , and the *electrostatic* potential  $e\phi_N$ . The single-particle state  $E_N$  for the  $N$ th electron is measured from the bottom of the conduction band and depends on the characteristics of the confinement potential. The electrostatic potential  $\phi_N$  contains a discrete and a continuous part. In our definition the integer  $N$  is the number of electrons at a gate voltage  $V_g$  and  $N_o$  is the number at zero gate voltage. The continuous part in  $\phi_N$  is proportional to the gate voltage. At fixed gate voltage, the number of electrons on the dot  $N$  is the largest integer for which  $\mu_{dot}(N) < \mu_{left} \equiv \mu_{right}$ . When, at fixed gate voltage, the number of electrons is changed by one, the resulting change in electrochemical potential is:

$$\mu_{dot}(N+1) - \mu_{dot}(N) = \Delta E + \frac{e^2}{C} \quad (2.2)$$

The *addition energy*  $\mu_{dot}(N+1) - \mu_{dot}(N)$  is large for a small capacitance and/or a large energy splitting  $\Delta E = E_{N+1} - E_N$  between 0D-states. It is important to note that the many-body contribution  $e^2/C$  to the energy gap of Eq. (2.2) exists only at the Fermi energy. Below  $\mu_{dot}(N)$ , the energy states are only separated by the single-particle energy differences  $\Delta E$  [see Fig. 2.1(a)]. These energy differences  $\Delta E$  are the *excitation energies* of a dot with constant number  $N$ .

A non-zero addition energy can lead to a blockade for tunneling of electrons on and off the dot, as depicted in Fig. 2.1(a), where  $N$  electrons are localized on the dot. The  $(N+1)$ th electron cannot tunnel on the dot, because the resulting electrochemical potential  $\mu_{dot}(N+1)$  is higher than the potentials of

the reservoirs. So, for  $\mu_{dot}(N) < \mu_{left}, \mu_{right} < \mu_{dot}(N+1)$  the electron transport is blocked, which is known as the *Coulomb blockade*.

The Coulomb blockade can be removed by changing the gate voltage, to align  $\mu_{dot}(N+1)$  between  $\mu_{left}$  and  $\mu_{right}$ , as illustrated in Fig. 2.1(b) and (c). Now, an electron can tunnel from the left reservoir on the dot [since,  $\mu_{left} > \mu_{dot}(N+1)$ ]. The electrostatic increase  $e\phi(N+1) - e\phi(N) = e^2/C$  is depicted in Fig. 2.1(b) and (c) as a change in the conduction band bottom. Since  $\mu_{dot}(N+1) > \mu_{right}$ , one electron can tunnel off the dot to the right reservoir, causing the electrochemical potential to drop back to  $\mu_{dot}(N)$ . A new electron can now tunnel on the dot and repeat the cycle  $N \rightarrow N+1 \rightarrow N$ . This process, whereby current is carried by successive discrete charging and discharging of the dot, is known as *single electron tunneling*, or *SET*.

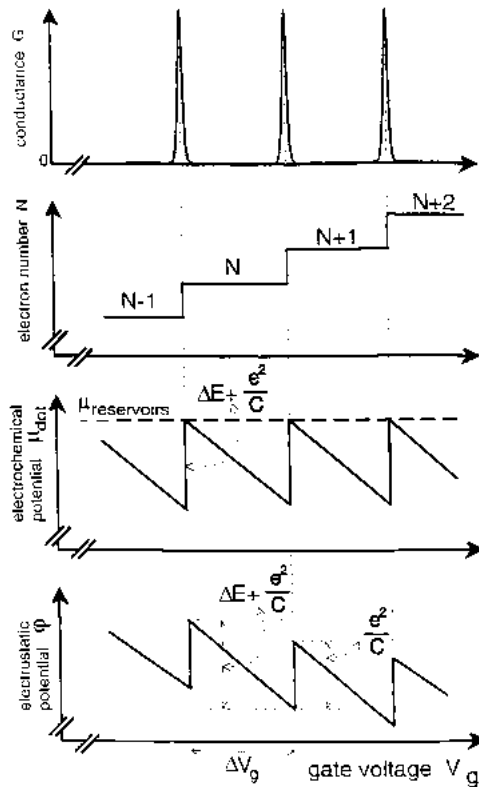


Figure 2.3. Schematic comparison, as a function of gate voltage, between (a) the Coulomb oscillations in the conductance  $G$ , (b) the number of electrons in the dot ( $N+i$ ), (c) the electrochemical potential in the dot  $\mu_{dot}(N+i)$ , and (d) the electrostatic potential  $\phi$ .

On sweeping the gate voltage, the conductance oscillates between zero (Coulomb blockade) and non-zero (no Coulomb blockade), as illustrated in Fig. 2.3. In the case of zero conductance, the number of electrons  $N$  on the dot is fixed. Fig. 2.3 shows that upon going across a conductance maximum (a),  $N$  changes by one (b), the electrochemical potential  $\mu_{dot}$  shifts by  $\Delta E + e^2/C$  (c), and the electrostatic potential  $e\phi$  shifts by  $e^2/C$  (d). From Eq. (2.1) and the condition  $\mu_{dot}(N, V_g) = \mu_{dot}(N+1, V_g + \Delta V_g)$ , we get for the distance in gate voltage  $\Delta V_g$  between oscillations [18]:

$$\Delta V_g = \frac{C}{eC_g} \left( \Delta E + \frac{e^2}{C} \right) \quad (2.3a)$$

and for the position of the  $N$ th conductance peak:

$$V_g(N) = \frac{C}{eC_g} \left( E_N + (N - \frac{1}{2}) \frac{e^2}{C} \right) \quad (2.3b)$$

For vanishing energy splitting  $\Delta E \cong 0$ , the classical capacitance-voltage relation for a single electron charge  $\Delta V_g = e/C_g$  is obtained; the oscillations are periodic. Non-vanishing energy splitting results in nearly periodic oscillations. For instance, in the case of spin-degenerate states two periods are, in principle, expected. One corresponds to electrons  $N$  and  $N+1$  having opposite spin and being in the same spin-degenerate 0D-state, and the other to electrons  $N+1$  and  $N+2$  being in different 0D-states.

## 2.2. AMPLITUDE AND LINESHAPE OF COULOMB OSCILLATIONS.

We now consider the detailed shape of the oscillations and, in particular, the dependence on temperature. We assume that the temperature is greater than the quantum mechanical broadening of the 0D energy levels  $h\Gamma \ll k_B T$ . We return to this assumption later. We distinguish three temperature regimes:

- (1)  $e^2/C \ll k_B T$ , where the discreteness of charge cannot be discerned.
- (2)  $\Delta E \ll k_B T \ll e^2/C$ , the *classical or metallic Coulomb blockade* regime, where many levels are excited by thermal fluctuations.
- (3)  $k_B T \ll \Delta E < e^2/C$ , the *quantum Coulomb blockade* regime, where only one or a few levels participate in transport.

In the high temperature limit,  $e^2/C \ll k_B T$ , the conductance is independent of the electron number and is given by the Ohmic sum of the two barrier conductances  $1/G = 1/G_\infty = 1/G_{left} + 1/G_{right}$ . This high temperature

conductance  $G_\infty$  is independent of the size of the dot and is characterized completely by the two barriers.

The classical Coulomb blockade regime can be described by the so-called “orthodox” Coulomb blockade theory [4, 5, 23]. Fig. 2.4(a) shows a calculated plot of Coulomb oscillations at different temperatures for energy-independent barrier conductances and an energy-independent density of states. The Coulomb oscillations are visible for temperatures  $k_B T < 0.3e^2/C$  (curve c). The lineshape of an individual conductance peak is given by [6, 23]:

$$\frac{G}{G_\infty} = \frac{\delta/k_B T}{2 \sinh(\delta/k_B T)} \approx \frac{1}{2} \cosh^{-2} \left( \frac{\delta}{2.5 k_B T} \right) \quad \text{for } h\Gamma, \Delta E \ll k_B T \ll e^2/C \quad (2.4)$$

$\delta$  measures the distance to the center of the peak in units of energy, which expressed in gate voltage is  $\delta = e(C_g/C) \cdot |V_{g,res} - V_g|$ , with  $V_{g,res}$  the gate voltage at resonance. The width of the peaks are linear in temperature as long as  $k_B T \ll e^2/C$ . The peak maximum  $G_{max}$  is independent of temperature in this regime (curves a and b) and equal to half the high temperature value  $G_{max} = G_\infty / 2$ . This conductance is half the Ohmic addition value because of the effect of correlations: since an electron must first tunnel off before the next can tunnel on, the probability to tunnel through the dot decreases to one half.

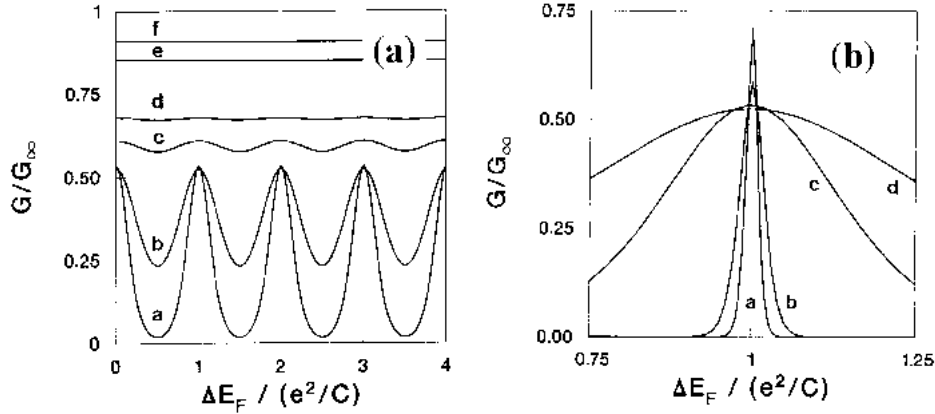


Figure 2.4. Calculated temperature dependence of the Coulomb oscillations as a function of Fermi energy in the classical regime (a) and in the quantum regime (b). In (a) the parameters are  $\Delta E = 0.01e^2/C$  and  $k_B T/(e^2/C) = 0.075$  [a], 0.15 [b], 0.3 [c], 0.4 [d], 1 [e], and 2 [f]. In (b) the parameters are  $\Delta E = 0.01e^2/C$  and  $k_B T/\Delta E = 0.5$  [a], 1 [b], 7.5 [c], and 15 [d]. (From van Houten, Beenakker and Staring [7].)

In the quantum Coulomb blockade regime, tunneling occurs through a single level. The temperature dependence calculated by Beenakker [6] is shown in Fig. 2.4(b). The single peak conductance is given by:

$$\frac{G}{G_\infty} = \frac{\Delta E}{4k_B T} \cosh^{-2}\left(\frac{\delta}{2k_B T}\right) \quad \text{for } h\Gamma \ll k_B T \ll \Delta E, e^2/C \quad (2.5)$$

with the assumption that  $\Delta E$  is independent of  $E$  and  $N$ . The lineshape in the classical and quantum regimes are virtually the same, except for the different ‘effective temperatures’. However, the peak maximum  $G_{max} = G_\infty \cdot (\Delta E/4k_B T)$  decreases linearly with increasing temperature in the quantum regime, while it is constant in the classical regime. This distinguishes a quantum peak from a classical peak.

The temperature dependence of the peak height is summarized in Fig. 2.5. On decreasing the temperature, the peak maximum first decreases down to half the Ohmic value. On entering the quantum regime, the peak maximum increases and starts to exceed the Ohmic value. Thus, at intermediate temperatures, Coulomb correlations reduce the conductance maximum below the Ohmic value, while at low temperatures, quantum phase coherence results in a resonant conductance exceeding the Ohmic value.

Above we discussed the temperature dependence of an individual conductance peak and how it can be used to distinguish the classical from the quantum regimes. Comparing the heights of different peaks at a single temperature (i.e. in a single gate voltage trace) can also distinguish classical from quantum peaks. Classical peaks all have the same height  $G_{max} = G_\infty/2$ .

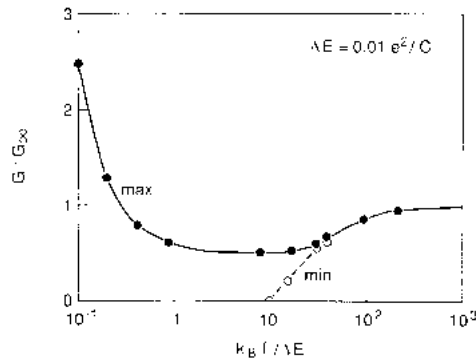


Figure 2.5 Calculated temperature dependence of the maxima and minima of the Coulomb oscillations for  $h\Gamma \ll k_B T$  and  $\Delta E = 0.01 e^2/C$ . (From van Houten, Beenakker and Staring [7].)

(In semiconductor dots the peak heights slowly change since the barrier conductances change with gate voltage.) On the other hand, in the quantum regime, the peak height depends sensitively on the coupling between the levels in the dot and in the leads. This coupling can vary strongly from level to level. Also, as can be seen from  $G_{max} = G_{\infty}(\Delta E/4k_B T)$ , the  $N$ th peak probes the specific excitation spectrum around  $\mu_{dot}(N)$  when the temperatures  $k_B T \sim \Delta E$  [45]. The quantum regime therefore usually shows randomly varying peak heights. This is discussed in section 6.

An important assumption for the above description of tunneling in both the quantum and classical Coulomb blockade regimes is that the barrier conductances are small:  $G_{left,right} \ll e^2/h$ . This assumption implies that the broadening  $h\Gamma$  of the energy levels in the dot due to the coupling to the leads is much smaller than  $k_B T$ , even at low temperatures. The charge is well defined in this regime and quantum fluctuations in the charge can be neglected (i.e. the quantum probability to find a particular electron on the dot is either zero or one). This statement is equivalent to the requirement that only first order tunneling has to be taken into account and higher order tunneling via virtual intermediate states can be neglected [53]. A treatment of the regime  $k_B T \sim h\Gamma$  involves the inclusion of higher order tunneling processes. Such complicated calculations have recently been performed [54-56]. For simplicity, we discuss this regime by considering non-interacting electrons and equal barriers. Then the zero temperature conductance is given by the well-known Breit-Wigner formula [57]:

$$G_{BW} = \frac{2e^2}{h} \frac{(h\Gamma)^2}{(h\Gamma)^2 + \delta^2} \quad \text{for } T = 0, e^2/C \ll h\Gamma, \Delta E \quad (2.6)$$

The on-resonance peak height (i.e. for  $\delta = 0$ ) is equal to the conductance quantum  $2e^2/h$ ; the factor 2 results from spin-degeneracy. The finite temperature conductance follows from  $G = \int dE \cdot G_{BW} \cdot (-\partial f/\partial E)$ , where  $f(E)$  is the Fermi-Dirac function. Although the electron-electron interactions are ignored, it will be shown in the experimental section that Coulomb peaks in the regime  $k_B T \sim h\Gamma$  have the Lorentzian lineshape of Eq. (2.6).

### 2.3. NON-LINEAR TRANSPORT.

In addition to the linear-response Coulomb oscillations, one can obtain information about the relevant energy scales of the dot by measuring the non-linear dependence of the current on the source-drain voltage  $V_{sd}$ . Following the rule that the current depends on the number of available states in the window  $eV_{sd} = \mu_{left} - \mu_{right}$ , one can monitor changes in the number of available states

when increasing  $V_{sd}$ . To discuss non-linear transport it is again helpful to distinguish the classical and the quantum Coulomb blockade regime.

In the classical regime, the current is zero as long as the interval between  $\mu_{left}$  and  $\mu_{right}$  does not contain a charge state [i.e. when  $\mu_{dot}(N) < \mu_{right}$ ,  $\mu_{left} < \mu_{dot}(N+1)$ ] as in Fig. 2.1(a)]. On increasing  $V_{sd}$ , current starts to flow when either  $\mu_{left} > \mu_{dot}(N+1)$  or  $\mu_{dot}(N) > \mu_{right}$ , depending on how the voltage drops across the two barriers. One can think of this as opening a charge channel, corresponding to either the  $N \rightarrow (N+1)$  [this example is shown in Fig. 2.6] or the  $(N-1) \rightarrow N$  transition. On further increasing  $V_{sd}$ , a second channel will open up when *two* charge states are contained between  $\mu_{left}$  and  $\mu_{right}$ . The current then experiences a second rise.

For an asymmetric quantum dot with unequal barriers, the voltage across the device drops mainly across the less-conducting barrier. For strong asymmetry, the electrochemical potential of one of the reservoirs is essentially fixed relative to the charge states in the dot, while the electrochemical potential of the other reservoir moves in accordance with  $V_{sd}$ . In this asymmetric case, the current changes are expected to appear in the  $I$ - $V_{sd}$  characteristics as pronounced steps, the so-called *Coulomb staircase* [3, 4, 23]. The current steps  $\Delta I$  occur at voltage intervals  $\Delta V_{sd} \approx e/C$ . In a region of constant current, the topmost charge state is nearly always full or nearly always empty depending on whether the reservoir with the higher electrochemical potential is coupled to the dot via the small barrier or via the large barrier, respectively. In the example depicted in Fig. 2.6 the  $(N+1)$  charge state is nearly always occupied.

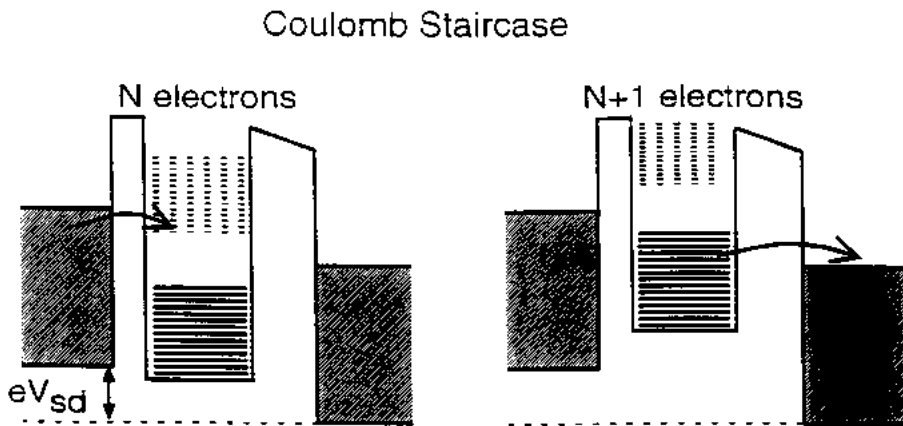


Figure 2.6. Energy diagram to indicate that for larger source-drain voltage  $V_{sd}$  the empty states above the Coulomb gap can be occupied. This can result in a Coulomb staircase in current-voltage characteristic [see Fig. 1.2(b)]

Reversing the sign of  $V_{sd}$  would leave the  $(N+1)$  charge state nearly always empty.

In the quantum regime a finite source-drain voltage can be used to perform spectroscopy on the discrete energy levels [51]. On increasing  $V_{sd}$  we can get two types of current changes. One corresponds to a change in the number of charge states in the source-drain window, as discussed above. The other corresponds to changes in the number of energy levels which electrons can choose for tunneling on or off the dot. The voltage difference between current changes of the first type measures the addition energy while the voltage differences between current changes of the second type measures the excitation energies. More of this spectroscopy method will be discussed in the experimental section 3.2.

#### 2.4. OVERVIEW OTHER THEORETICAL WORKS.

The theory outlined above represent a highly simplified picture of how electrons on the dot interact with each other and with the reservoirs. In particular, we have made two simplifications. First, we have assumed that the coupling to the leads does not perturb the levels in the dot. Second, we have represented the electron-electron interactions by a constant capacitance parameter. Below, we briefly comment on the limitations of this picture, and discuss more advanced and more realistic theories.

A non-zero coupling between dot and reservoirs is included by assuming an intrinsic width  $\hbar\Gamma$  of the energy levels. A proper calculation of  $\hbar\Gamma$  should not only include direct elastic tunnel events but also tunneling via intermediate states at other energies. Such higher order tunneling processes are referred to as co-tunneling events [53]. They become particularly important when the barrier conductances are not much smaller than  $e^2/h$ . Experimental results on co-tunneling have been reported by Geerligs *et al.* [58] and Eiles *et al.* [59] for metallic structures and by Pasquier *et al.* [60] for semiconductor quantum dots. In addition to higher order tunneling mediated by the Coulomb interaction, the effects of spin interaction between the confined electrons and the reservoir electrons have been studied theoretically [61-67]. When coupled to reservoirs, a quantum dot with a net spin, for instance, a dot with an odd number of electrons, resembles a magnetic impurity coupled to the conduction electrons in a metal. "Screening" of the localized magnetic moment by the conduction electrons leads to the well-known *Kondo effect* [61-67]. This is particularly interesting since parameters like the exchange coupling and the Kondo temperature should be tunable with a gate voltage. However, given the size of present day quantum dots, the Kondo temperature is hard to reach, and no

experimental results have been reported to date. Experimental progress has been made recently in somewhat different systems [68,69].

The second simplification is that we have modeled the Coulomb interactions with a constant capacitance parameter, and we have treated the single-particle states as independent of these interactions. More advanced descriptions calculate the energy spectrum in a self-consistent way. In particular, for small electron number ( $N < 10$ ) the capacitance is found to depend on  $N$  and on the particular confinement potential [45-47, 70]. In this regime, screening within the dot is poor and the capacitance is no longer a geometric property. It is shown in section 7 that the constant capacitance model also fails dramatically when a high magnetic field is applied. Calculations beyond the self-consistent Hartree approximation have also been performed. Several authors have followed Hartree-Fock [71-73] and exact [74,75] schemes in order to include spin and exchange effects in few-electron dots [76]. One prediction is the occurrence of spin singlet-triplet oscillations by Wagner *et al.* [77]. Evidence for this effect has been given recently [50,78], which we discuss in section 7.

There are other simplifications as well. Real quantum dot devices do not have perfect parabolic or hard wall potentials. They usually contain many potential fluctuations due to impurities in the substrate away from the 2DEG. Their ‘thickness’ in the  $z$ -direction is not zero but typically 10 nm. And as a function of  $V_g$ , the potential bottom not only rises, but also the shape of the potential landscape changes. Theories virtually always assume effective mass approximation, zero thickness of the 2D gas, and no coupling of spin to the lattice nuclei. In discussions of delicate effects, these assumptions may be too crude for a fair comparison with real devices. In spite of these problems, however, we point out that the constant capacitance model and the more advanced theories yield the same, important, qualitative picture of having an excitation and an addition energy. The experiments in the next section will clearly confirm this common aspect of the different theories.

### 3. Experiments on single lateral quantum dots.

This section presents experiments which can be understood with the theory of the previous section. We focus in this section on lateral quantum dots which are defined by metallic gates in the 2DEG of a GaAs/AlGaAs heterostructure. These dots typically contain 50 to a few hundred electrons. (Smaller dots containing just a few electrons  $N < 10$ ) will be discussed in section 5.) First, we discuss linear response measurements (3.1) while section 3.2 addresses experiments with a finite source-drain voltage.

### 3.1. LINEAR RESPONSE COULOMB OSCILLATIONS.

Fig. 3.1 shows a measurement of the conductance through a quantum dot of the type shown in Fig. 1.1 as a function of a voltage applied to the center gates [79]. As in a normal field-effect transistor, the conductance decreases when the gate voltage reduces the electron density. However, superimposed on this decreasing conductance are periodic oscillations. As discussed in section 2, the oscillations arise because, for a weakly coupled quantum dot, the number of electrons can only change by an integer. Each period seen in Fig. 3.1 corresponds to changing the number of electrons in the dot by one. The period of the oscillations is roughly independent of magnetic field. The peak height is close to  $e^2/h$ . Note that the peak heights at  $B = 0$  show a gradual dependence on gate voltage. This indicates that the peaks at  $B = 0$  are classical (i.e. the single electron current flows through many OD-levels). The slow height modulation is simply due to the gradual dependence of the barrier conductances on gate voltage. A close look at the trace at  $B = 3.75$  T reveals a quasi-periodic modulation of the peak amplitudes. This results from the formation of Landau levels within the dot and will be discussed in detail in section 7. It does not necessarily mean that tunneling occurs through a single quantum level.

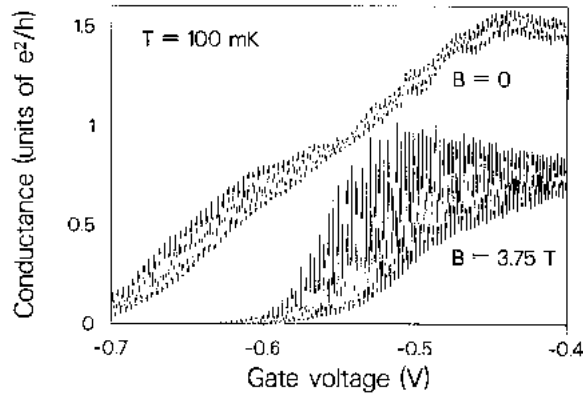


Figure 3.1. Coulomb oscillations in the conductance as a function of center gate voltage measured in a device similar to the one shown in Fig. 1.3, at zero magnetic field and in the quantum Hall regime. (From Williamson *et al.* [79].)

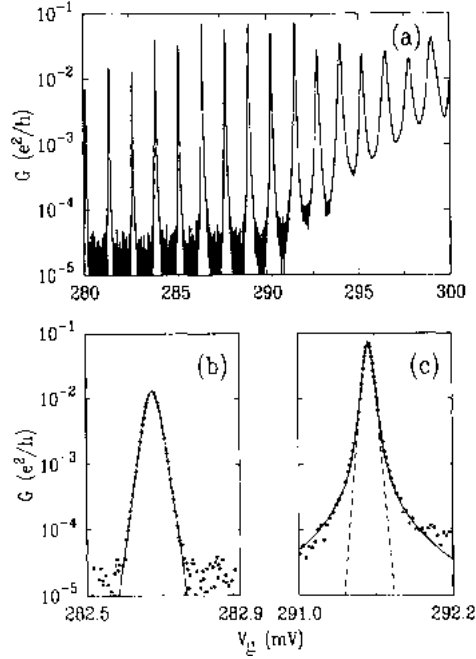


Figure 3.2. Coulomb oscillations measured at  $B = 2.53$  T. The conductance is plotted on a logarithmic scale. The peaks in the left region of (a) have a thermally broadened lineshape as shown by the expansion in (b). The peaks in the right region of (a) have a Lorentzian lineshape as shown by the expansion in (c). (From Foxman *et al.* [80].)

The effect of increasing barrier conductances due to changes in gate voltage can be utilized to study the effect of an increased coupling between dot and macroscopic leads. This increased coupling to the reservoirs (i.e. from left to right in Fig. 3.1) results in broadened, overlapping peaks with minima which do not go to zero. Note that this occurs despite the constant temperature during the measurement. In Fig. 3.2 the coupling is studied in more detail in a different, smaller dot where tunneling is through individual quantum levels [80,81]. The peaks in the left part are so weakly coupled to the reservoirs that the intrinsic width is negligible:  $h\Gamma \ll k_B T$ . The expanded peak in (b) confirms that the lineshape in this region is determined by the Fermi distribution of the electrons in the reservoirs.

On a logarithmic scale, the finite temperature Fermi distribution leads to linearly decaying tails. The solid line in (b) is a fit to Eq. (2.5) with a temperature of 65 mK and fit parameter  $e^2/C = 0.61$  meV. The peaks in the

right part of (a) are so broadened that the tails of adjacent peaks overlap. The peak in (c) is expanded from this strong coupling region and clearly shows that the tails have a slower decay than expected for a thermally broadened peak. In fact, a good fit is obtained with the Lorentzian lineshape of Eq. (2.6) with the inclusion of a temperature of 65 mK (so  $k_B T = 5.6 \mu\text{eV}$ ). In this case, the fit parameters give  $h\Gamma = 5 \mu\text{eV}$  and  $e^2/C = 0.35 \text{ meV}$ . The Lorentzian tails are still clearly visible despite the fact that  $k_B T \approx h\Gamma$ . An important conclusion from this experiment is that for strong Coulomb interaction the lineshape for tunneling through a discrete level is approximately Lorentzian, similar to the non-interacting Breit-Wigner formula (2.6).

Fig. 3.3(a) shows the temperature dependence of a set of selected conductance peaks [52]. These peaks are measured for barrier conductances much smaller than  $e^2/h$  where  $h\Gamma \ll k_B T$ . Above approximately 1K, the peak heights increase monotonically, but at low temperature, a striking fluctuation in peak heights is observed. Moreover, some peaks decrease and others increase on increasing temperature. Random peak behavior is not seen in metallic Coulomb islands. It is due to the discrete density of states in quantum dots. The randomness from peak to peak is usually ascribed to the variations in the nature of the energy levels in the dot. The observed behavior is reproduced in the calculations of Fig. 3.3(b), where variations are included in the form of a random coupling of the quantum states to the leads [52]. The origin of this random coupling is the random speckle-like spatial pattern of the electron wave function in the dot resulting from a disordered or ‘chaotic’ confining potential. We return to chaos in dots in section 6.

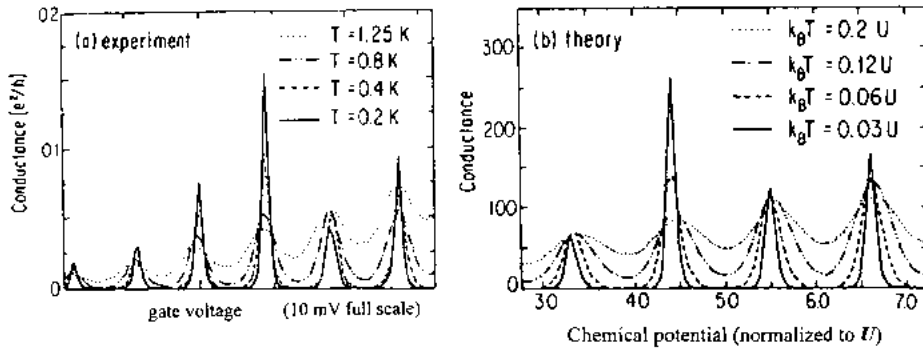


Figure 3.3. Comparison between (a) measured and (b) calculated Coulomb oscillations in the quantum regime for different temperatures at  $B = 0$ . For the calculation, the level spacing was taken to be uniform:  $\Delta E = 0.1U = 0.1e^2/C$ , but the coupling of successive energy levels was varied to simulate both an overall gradual increase and random variations from level to level (From Meir, Wingreen and Lee [52].)

The temperature dependence of a single quantum peak at  $B = 0$  is shown in Fig. 3.4 [81]. The upper part shows that the peak height decreases as inverse temperature up to about 0.4 K. Beyond 0.4 K the peak height is independent of temperature up to about 1 K. We can compare this temperature behavior with the theoretical temperature dependence of classical peaks in Fig. 2.4(a) and the quantum peaks in Fig. 2.4(b). The height of a quantum peak first decreases until  $k_B T$  exceeds the level spacing  $\Delta E$ , where around 0.4 K it crosses over to the classical Coulomb blockade regime. This transition is also visible in the width of the peak. The lower part of Fig. 3.4 shows the full-width-at-half-maximum (FWHM) which is a measure of the lineshape. The two solid lines differ in slope by a factor 1.25 which corresponds to the difference in "effective temperature" between the classical lineshape of Eq. (2.4) and quantum lineshape of Eq. (2.5). At about 0.4 K a transition is seen from a quantum to a classical temperature dependence, which is in good agreement with the theory of section 2.2.

The conclusions of this section are that quantum tunneling through discrete levels leads to conductance peaks with the following properties: The maxima increase with decreasing temperature and can reach  $e^2/h$  in height; the lineshape gradually changes from thermally broadened for weak coupling to Lorentzian for strong coupling to the reservoirs; and the peak amplitudes show random variations at low magnetic fields.

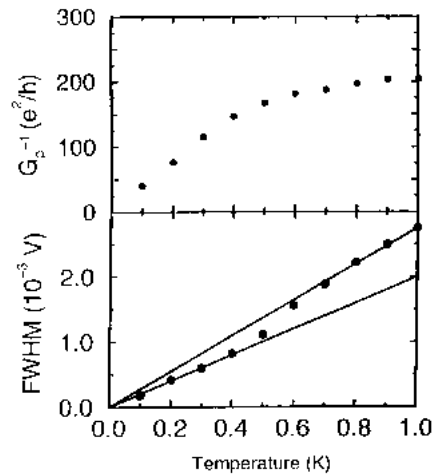


Figure 3.4. Inverse peak height and full-width-half-maximum (FWHM) versus temperature at  $B = 0$ . The inverse peak height shows a transition from linear  $T$  dependence to a constant value. The FWHM has a linear temperature dependence and shows a transition to a steeper slope. These measured transitions agree well with the calculated transition from the classical to the quantum regime. (From Foxman *et al.* [81].)

## 3.2. NON-LINEAR TRANSPORT REGIME.

In the non-linear transport regime one measures the current  $I$  (or differential conductance  $dI/dV_{sd}$ ) while varying the source-drain voltage  $V_{sd}$  or the gate voltage  $V_g$ . The rule that the current depends on the number of states in the energy window  $eV_{sd} = (\mu_{left} - \mu_{right})$  suggests that one can probe the energy level distribution by measuring the dependence of the current on the size of this window.

The example shown in Fig. 3.5 demonstrates the presence of two energies: the *addition energy* and the *excitation energy* [82]. The lowest trace is measured for small  $V_{sd}$  ( $V_{sd} \ll \Delta E$ ). The two oscillations are regular Coulomb oscillations where the change in gate voltage  $\Delta V_g$  corresponds to the energy necessary for adding one electron to the dot. In the constant capacitance model this addition energy is expressed in terms of energy in Eq. (2.2) and in terms of gate voltage in Eq. (2.3).

The excitation energy is discerned when the curves are measured with a larger  $V_{sd}$ . A larger source-drain voltage leads not only to broadened oscillations, but also to additional structure. Single peaks clearly develop into double peaks, and then triple peaks. Below we explain in detail that a single peak corresponds to tunneling through a single level (when  $eV_{sd} < \Delta E$ ), a double peak involves tunneling via two levels (when  $\Delta E < eV_{sd} < 2\Delta E$ ), and a triple peak involves three levels (when  $2\Delta E < eV_{sd} < 3\Delta E$ ). The spacing between mini-peaks is therefore a measure of the excitation energy with a constant number of electrons on the dot. These measurements yield to an excitation energy  $\Delta E \approx 0.3$  meV which is about ten times smaller than the Coulomb

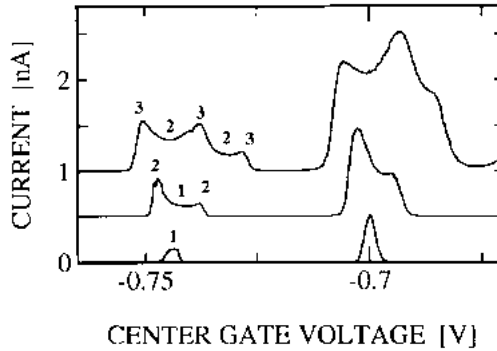


Figure 3.5. Coulomb peaks at  $B = 4$  T measured for different source-drain voltages  $V_{sd}$ . From the bottom curve up  $V_{sd} = 0.1, 0.4,$  and  $0.7$  meV. The peak to peak distance corresponds to the addition energy  $e^2/C + \Delta E$ . The distance between mini-peaks corresponds to the excitation energy  $\Delta E$  for constant number of electrons on the dot. (From Johnson *et al.* [82].)

charging energy in this structure.

To explain these results in more detail, we use the energy diagrams [83] in Fig. 3.6 for five different gate voltages. The thick vertical lines represent the tunnel barriers. The source-drain voltage  $V_{sd}$  is somewhat larger than the energy separation  $\Delta E = E_{N+1} - E_N$ , but smaller than  $2\Delta E$ . In (a) the number of electrons in the dot is  $N$  and transport is blocked. When the potential of the dot is increased via the gate voltage, the 0D-states move up with respect to the reservoirs. At some point the  $N$ th electron can tunnel to the right reservoir, which increases the current from zero in (a) to non-zero in (b). In (b), and also in (c) and (d), the electron number alternates between  $N$  and  $N-1$ . We only show the energy states for  $N$  electrons on the dot. For  $N-1$  electrons the single particle states are lowered by  $e^2/C$ . (b) illustrates that the non-zero source-drain voltage gives two possibilities for tunneling from the left reservoir onto the dot. A new electron, which brings the number from  $N-1$  back to  $N$ , can tunnel to the ground state  $E_N$  or to the first excited state  $E_{N+1}$ . This is denoted by the crosses in the levels  $E_N$  and  $E_{N+1}$ . Again, note that these levels are drawn for  $N$  electrons on the dot. So, in (b) there are two available states for tunneling onto the dot of which only one can get occupied. If the extra electron occupies the excited state  $E_{N+1}$ , it can either tunnel out of the dot from  $E_{N+1}$ , or first relax to  $E_N$  and then tunnel out. In either case, only this one electron can tunnel out of the dot. We have put the number of tunnel possibilities below the barriers.

If the potential of the dot is increased further to the case in (c), the electrons from the left reservoir can only tunnel to  $E_N$ . This is due to our choice for the source-drain voltage:  $\Delta E < eV_{sd} < 2\Delta E$ . Now, only the ground state level can be used for tunneling on and for tunneling off the dot. So, compared to (b) the number of tunnel possibilities has been reduced and thus we expect a somewhat smaller current in (c).

Continuing to move up the potential of the dot results in the situation depicted in (d). It is still possible to tunnel to level  $E_N$ , but in this case one electron, either in  $E_N$  or in  $E_{N-1}$ , can tunnel off the dot. So, here we have one possibility for tunneling onto the dot and two for tunneling off. Compared to (c) we thus expect a rise in the current. It can be shown that for equal barriers the currents in (b) and (d) are equal [83].

Increasing the potential further, brings the dot back to the Coulomb blockade and the current drops back to zero. Note that in (e) the levels are shown for  $N-1$  electrons on the dot.

Going through the cycle from (a) to (e) we see that the number of available states for tunneling changes like 0-2-1-2-0. This is also observed in the experiment of Fig. 3.5. The second curve shows two maxima which correspond to cases 3.6(b) and 3.6(d). The minimum corresponds to case 3.6(c). For a source-drain voltage such that  $2\Delta E < eV_{sd} < 3\Delta E$  the sequence of

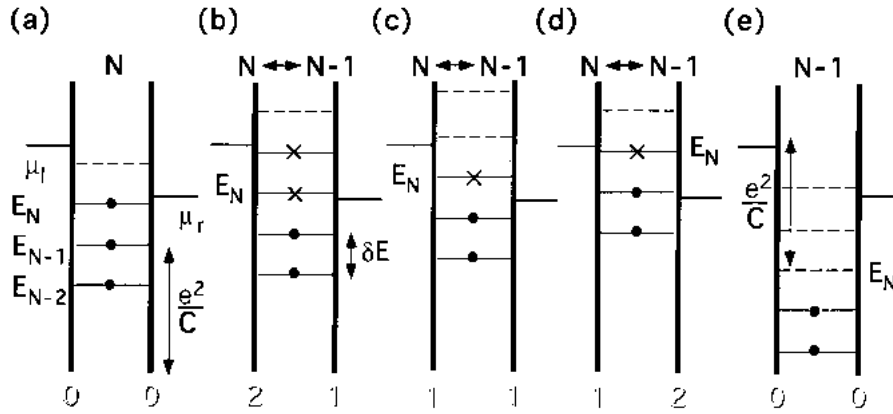


Figure 3.6. Energy diagrams for five increasingly negative gate voltages. The thick lines represent the tunnel barriers. The number of available tunnel possibilities is given below the barriers. Horizontal lines with a bold dot denote occupied OD-states. Dashed horizontal lines denote empty states. Horizontal lines with crosses may be occupied. In (a) transport is blocked with  $N$  electrons on the dot. In (b) there are two states available for tunneling on the dot and one state for tunneling off. The crosses in level  $E_N$  and  $E_{N+1}$  denote that only one of these states can get occupied. In (c) there is just one state that can contribute to transport. In (d) there is one state to tunnel to and there are two states for tunneling off the dot. In (e) transport is again blocked, but now with  $N-1$  electrons on the dot. Note that in (a)-(d) the levels are shown for  $N$  electrons on the dot while for (e) the levels are shown for  $N-1$  electrons (From van der Vaart *et al* [83].)

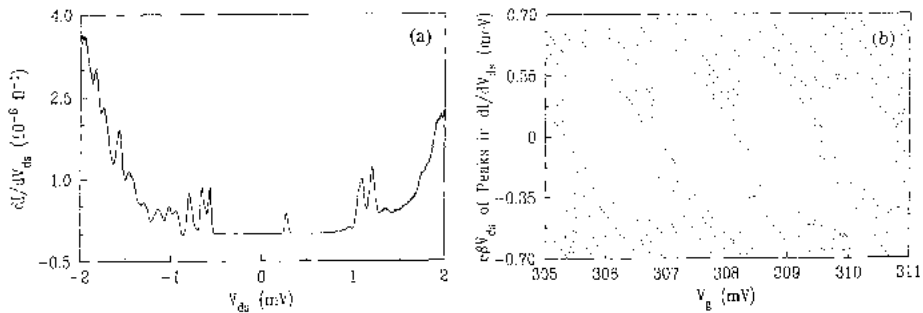


Figure 3.7. (a)  $dI/dV_{sd}$  versus  $V_{sd}$  at  $B = 3.35$  T. The positions in  $V_{sd}$  of peaks from traces as in (a) taken at many different gate voltages are plotted in (b) as a function of gate voltage. A factor  $e\beta$  has been used to convert peak positions to electron energies. The diamond-shaped addition energy and the discrete excitation spectrum are clearly seen. (From Foxman *et al.* [80].)

contributing states is 0-3-2-3-2-3-0 as the center gate voltage is varied. Here, the structured Coulomb oscillation should show three maxima and two local minima. This is observed in the third curve in Fig. 3.5.

Fig. 3.7 shows data related to that in Fig. 3.5, but now in the form of  $dI/dV_{sd}$  versus  $V_{sd}$  [80]. The quantized excitation spectrum of a quantum dot leads to a set of discrete peaks in the differential conductance; a peak in  $dI/dV_{sd}$  occurs every time a level in the dot aligns with the electrochemical potential of one of the reservoirs. Many such traces like Fig. 3.7(a), for different values of  $V_g$ , have been collected in (b). Each dot represents the position of a peak from (a) in  $V_g$ - $V_{sd}$  space. The vertical axis is multiplied by a parameter that converts  $V_{sd}$  into energy [80]. Fig. 3.7(b) clearly demonstrates the Coulomb gap at the Fermi energy (i.e. around  $V_{sd} = 0$ ) and the discrete excitation spectrum of the single particle levels. The level separation  $\Delta E \approx 0.1$  meV in this particular device is much smaller than the charging energy  $e^2/C \approx 0.5$  meV.

The transport measurements described in this section clearly reveal the addition and excitation energies of a quantum dot. These two distinct energies arise from both quantum confinement and from Coulomb interactions. Overall, agreement between the simple theoretical model of section 2 and the data is quite satisfactory. However, we should emphasize here that our labeling of 0D-states has been too simple. In our model the first excited single-particle state  $E_{N+1}$  for the  $N$  electron system is the highest occupied single-particle state for the ground state of the  $N+1$  electron dot. (We neglect spin-degeneracy here.) Since in lateral dots the interaction energy is an order of magnitude larger than the separation between single-particle states, it is reasonable to expect that adding an electron will completely generate a new single-particle spectrum. In fact, to date there is no evidence that there is any correlation between the single-particle spectrum of the  $N$  electron system and the  $N+1$  electron system. This correlation is still an open issue. We note that there are also other issues that can regulate tunneling through dots. For example, it was recently argued [84] that the electron spin can result in a spin-blockade. The observation of a negative-differential conductance by Johnson *et al.* [82] and by Weis *et al.* [85] provides evidence for this spin-blockade theory [84].

#### 4. Multiple Quantum Dot Systems.

This section describes recent progress in multiple coupled quantum dot systems. If one quantum dot is an *artificial atom* [2], then multiple coupled quantum dots can be considered to be *artificial molecules* [86]. Combining insights from chemistry with the flexibility possible using lithographically defined structures, new investigations are possible. These range from studies

of the "chemical bond" between two coupled dots, to 0D-state spectroscopy, to possible new applications as quantum devices, including use in proposed quantum computers [87,88].

The type of coupling between quantum dots determines the character of the electronic states and the nature of transport through the artificial molecule. Purely electrostatic coupling is used in orthodox Coulomb blockade theory, for which tunnel rates are assumed to be negligibly small. The energetics are then dominated by electrostatics and described by the relevant capacitances, including an inter-dot capacitance  $C_{in}$ . However, in coupled dot systems the inter-dot tunnel conductance  $G_{int}$  can be large, i.e. comparable to or even greater than the conductance quantum  $G_Q = 2e^2/h$ . In this strong tunneling regime the charge on each dot is no longer well defined, and the Coulomb blockade is suppressed. So, both the capacitance and the tunnel conductance may influence transport.

All experiments described in this section are performed on lateral coupled quantum dots. Experiments on *electrostatically-coupled* quantum dots are described in 4.1, followed by experiments and theory of *tunnel-coupled* dots in 4.2. A new spectroscopic technique using two quantum dots is described in 4.3, and the issue of quantum coherence is discussed in 4.4.

#### 4.1. ELECTROSTATICALLY-COUPLED QUANTUM DOTS.

Electrostatically-coupled quantum dots with negligible inter-dot tunnel conductance fall within the realm of single electronics and are covered by the orthodox theory of the Coulomb blockade [4]. In this regime, the role of tunneling is solely to permit the incoherent transfer of electrons through an electrostatically-coupled circuit. Single electronics, so called because one electron can represent one bit of information, has been extensively studied for possible future applications in electronics and computation. Many interesting applications have been developed, including the electron turnstile [89,90], the electron pump [91,92], and the single electron trap [93]. Electron pumps fabricated from metal tunnel junctions are closely related to coupled quantum dot systems. An analysis of the electron pump using the orthodox theory of the Coulomb blockade was originally done by Pothier *et al.* [91], who found good agreement with experiment. We confine the discussion here to electrostatically-coupled semiconductor dots.

Parallel coupled dot configurations permit measurements using one dot to sense the charge on a second neighboring dot. If the first dot is operated as an electrometer the charge on a neighboring dot can modulate the current through this electrometer. Dot-electrometers are extremely sensitive to the charge on a neighboring dot. Even small changes of order  $10^{-4}e$  can be detected. A change

of a full electron charge can completely switch off the current through the electrometer. Narrow channels have also been employed as electrometers [94].

A parallel quantum dot configuration which demonstrates switching [95] is shown by the atomic force micrograph in Fig. 4.1. The dot on the right (dot 1) is operated as an electrometer controlled by gate  $C1$ , while the dot on the left (dot 2) is a box without leads whose charge is controlled by a second gate  $C2$ . The voltages on gates  $F1$ ,  $F2$ ,  $Q1$ , and  $Q2$  were used to define the double dot structure and to adjust the coupling between the dots. The coupling here is primarily capacitive, since the tunnel probability between dots 1 and 2 is made very small. Plots of the peak positions in the linear response conductance were used to map out the charge configurations  $(N_1, N_2)$  vs. gate voltages  $V_{g1}$  and  $V_{g2}$ , with  $N_i$  the number of electrons on dot  $i$ .

Fig. 4.2(a) is a plot of the measured conductance vs. gate voltages  $V_{g1}$  and  $V_{g2}$  (labeled  $V_{C1}$  and  $V_{C2}$ ). The peak locations jump periodically as the gate voltage on dot 2 is swept. This is clear evidence of the influence of the charge of dot 2, and it provides a demonstration of the switching function of capacitively-coupled dots. Fig. 4.2(b) is a comparison of the measured peak positions with a capacitive coupling model based on Coulomb blockade theory, described below. As shown, the agreement between theory and experiment is excellent.

The honeycomb pattern in Fig. 4.2 is characteristic of electrostatically-coupled double dot systems. Using Coulomb blockade theory, one can calculate the total electrostatic energy  $U_{N_1, N_2}(V_{g1}, V_{g2})$  of the coupled dot system for a given charge configuration  $(N_1, N_2)$  in the limit of negligible inter-dot tunneling [91, 95-97]. The energy surface  $U_{N_1, N_2}(V_{g1}, V_{g2})$  is a paraboloid with a minimum at the point  $(V_{g1}, V_{g2})$  for which the actual charge configuration  $(N_1, N_2)$  equals the charge induced by the gates. As  $N_1$  or  $N_2$  is incremented, the charging energy surface  $U$  repeats with a corresponding offset in gate voltage. The set of lowest charging energy surfaces forms an "egg-carton" potential defining an array of cells in gate voltage. Within each cell,  $N_1$  and  $N_2$  are both fixed. The borders between cells are defined by the intersections of charging energy surfaces for neighboring cells.

Along the border between cells the dot charge can change and transport can occur. For parallel coupled dot systems, current can flow through dot 1 only when the number of electrons on dot 1 can change. Referring to Fig. 4.2, this occurs along the lines joining cells  $(N_1, N_2)$  and  $(N_1 \pm 1, N_2)$ . Changes in the charge of dot 2 are possible along the boundaries between cells  $(N_1, N_2)$  and  $(N_1, N_2 \pm 1)$ . However, these changes do not produce current through dot 1. Also, no current flows as charge is swapped from one dot to the other along the boundaries between cells  $(N_1, N_2)$  and  $(N_1 + 1, N_2 - 1)$  or  $(N_1 - 1, N_2 + 1)$  because the

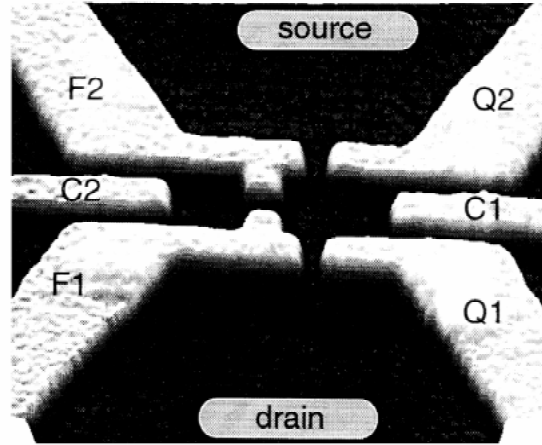


Figure 4.1. An atomic force image of the parallel-coupled dot device. The outer electrodes define both the quantum point contacts coupling the main dot to the reservoirs as well as the inner quantum point contact which controls the inter-dot coupling. The geometries of the two dots can be independently tuned with the two center gates. The right dot is about 400 x 400 nm (From Hoffman *et al.* [95].)

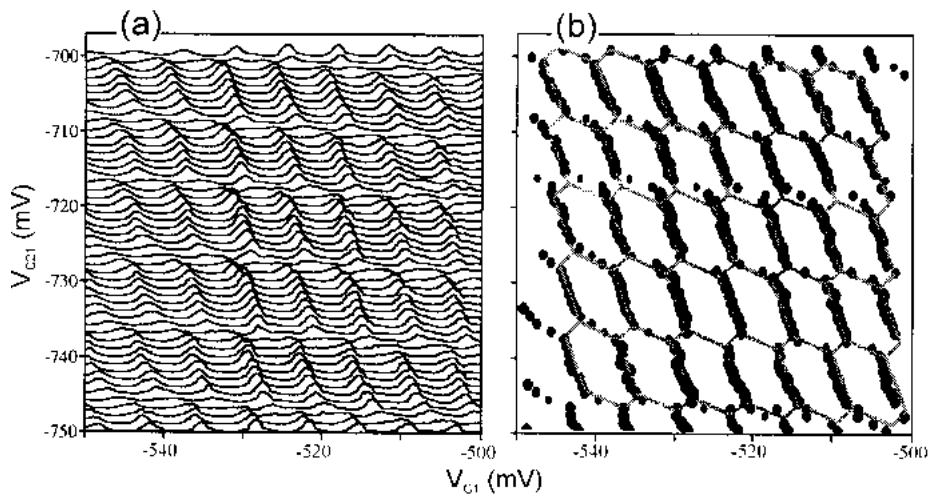


Figure 4.2. (a) Typical conductance measurements for the parallel dot structure shown in Fig. 4.1. Each trace corresponds to a fixed value of second center-gate voltage  $V_{C2}$ ; the curves are offset vertically. The conductance scale is arbitrary but constant over the whole range of measurements. (b) The conductance maxima of (a) are plotted as dots as a function of the two center-gate voltages. The phase diagram calculated from an electrostatic model is plotted as solid lines. (From Hoffman *et al.* [95].)

total number  $N = N_1 + N_2$  stays constant. These two borders are not predicted to lead to observable current peaks, and the corresponding sections of the honeycomb pattern in Fig. 4.2(b) do indeed not contain experimental data points. Note that for series coupled double dot systems, like those discussed below, the constraints on transport are different. Current can flow through both dots only when the charges on both dots can change. This occurs at the set of points where the line boundaries between cells  $(N_1, N_2)$  and  $(N_1 \pm 1, N_2)$  and between cells  $(N_1, N_2)$  and  $(N_1, N_2 \pm 1)$  intersect. The resulting conductance peak pattern is just a hexagonal array of *points*, as demonstrated in section 4.2.

Two dimensional scans of double dot conductance peak data are necessary in order to see the simplicity of the pattern of hexagonal cells. If only one gate is swept, the one dimensional trace cuts through data such as Fig. 4.2(a) along a single line, which may be inclined relative to both axes due to capacitive coupling of a single gate to both dots. The resulting series of peaks is no longer simply periodic, but shows evidence of both periods. With series coupled double dots, for which transport occurs only at an array of points, one dimensional conductance traces typically miss many points. The resulting suppression of conductance peaks predicted [98,99] and observed [100,101] in series coupled dot systems has been called the stochastic Coulomb blockade.

#### 4.2. TUNNEL-COUPLED QUANTUM DOTS.

When electrons tunnel at appreciable rates between quantum dots in a coupled dot system, the system forms an artificial molecule with "molecular" electronic states which can extend across the entire system. In this regime the charge on each dot is no longer quantized, and the orthodox theory of the Coulomb blockade can no longer be applied. Nonetheless, the total charge of the molecule can still be conserved. The reduction in ground state energy brought about by tunnel-coupling is analogous to the binding energy of a molecular bond. Analogies with chemistry and biochemistry may permit the design of new types of quantum devices and circuits based on tunnel-coupled quantum dots. Perhaps the most adventurous of these would be a quantum computer with electronic states which coherently extend across the entire system [87]. The issue of coherence is addressed in section 4.4.

Early experiments [37] on fifteen tunnel-coupled dots in series demonstrated evidence for coherent states over the entire sample. Below, we focus on more recent experiments on smaller two and three dot arrays, which make use of the ability to calibrate and continuously tune the inter-dot tunnel conductance during the experiment [96,101-107]. These experiments are analogs of textbook "gedanken" experiments in which the molecular binding energy is studied as a function of inter-atomic spacing.

The central issues in the theory of tunnel-coupled dots are the destruction of charge quantization by tunneling and the resulting changes in the ground state energy. These issues were originally addressed theoretically in the context of small metal tunnel junctions with many tunneling channels [108-111], unlike semiconductor dots with few channels. The theory of semiconductor dot arrays initially focused on models with one-to-one tunnel coupling between single particle levels in neighboring dots [112-114] with charging energy  $E_C = e^2/C$  small or comparable to the energy level spacing  $\Delta E$ . This approximation is inappropriate for strongly coupled many electron quantum dots like those discussed below, for which the charging energy is much greater than the level spacing  $E_C \gg \Delta E$ . (For 2D dots with constant  $E_F$  the charging energy varies with  $N$  as  $E_C \sim E_F/\sqrt{N}$ , because  $C$  is proportional to the dot radius, while the level spacing varies as  $\Delta E \sim E_F/N$ . In addition for  $N = 1$  we have  $E_F \sim E_C \sim \Delta E$ , producing the above inequality.) The destruction of charge quantization requires inter-dot tunneling rates comparable to  $E_C/\hbar$ , large enough to couple to a broad range of single-particle levels on each dot. The many-body theory of tunnel-coupled quantum dots in this limit has recently been developed [115-118] and is summarized below.

We begin this section with a description of an experiment on a double quantum dot with tunable inter-dot tunneling by Waugh *et al.* [101,102]. The experimental geometry is shown in Fig. 4.3(a), which is an SEM photograph of fourteen gates used to define a series array of nominally identical coupled quantum dots inside the 2DEG of a GaAs/AlGaAs heterostructure. By energizing only some of the gates, systems with one, two, or three dots can be created, and the conductance of each of the four quantum point contacts can be recorded and calibrated individually. For the data discussed below, two dots in series were formed, isolated by tunnel barriers from the leads, and traces of the linear response conductance peaks at low temperature were recorded vs. gate voltage. In this experiment two side gates with equal gate capacitance  $C_g$  were tied together so that the induced charges on each dot were nominally identical. This unpolarized gate arrangement corresponds to a trace taken along the diagonal  $V_{C1} = V_{C2}$  in Fig. 4.2(b).

Fig. 4.4 presents the central experimental result. As the inter-dot tunnel conductance increases from  $G_{int} = 0.03e^2/h$  in (a) to  $G_{int} = 1.94e^2/h$  in (d), the conductance peaks split by an increasing amount  $\Delta V_s$ , saturating in (d) at the spacing  $\Delta V_{sat}$ . The peak spacing in (a) is the same as for a single dot, whereas the spacing in (d) is half as large, indicating that the two dots have combined into a single large dot with twice the gate capacitance. Data similar to Fig. 4.4 were obtained independently by van der Vaart *et al.* [103].

We can understand the origin of peak splitting by examining theoretical plots of the electrostatic energy associated with the ground state of the array for

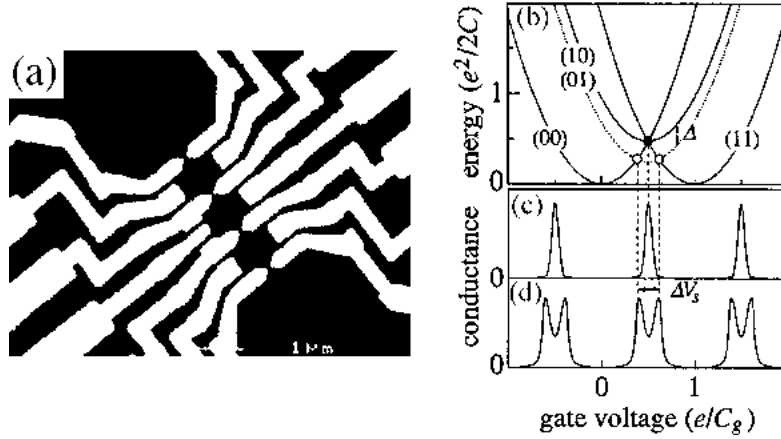


Figure 4.3. (a) SEM micrograph of three coupled quantum dots with tunable barriers. The dots are  $0.5 \times 0.8 \mu\text{m}^2$ . (b) Double dot charging energy vs. gate voltage for  $(N_1, N_2)$  electrons on each dot for identical dots. Without inter-dot coupling, parabolas with  $N_1 \neq N_2$  are degenerate (solid curves). Inter-dot coupling removes the degeneracy, shifting the lowest parabola down by  $\Delta = E_{int}$  (dotted curves). Schematic double dot conductance vs. gate voltage without coupling (c), and with coupling (d). Peaks occur at open markers in (b). (From Waugh *et al.* [102].)

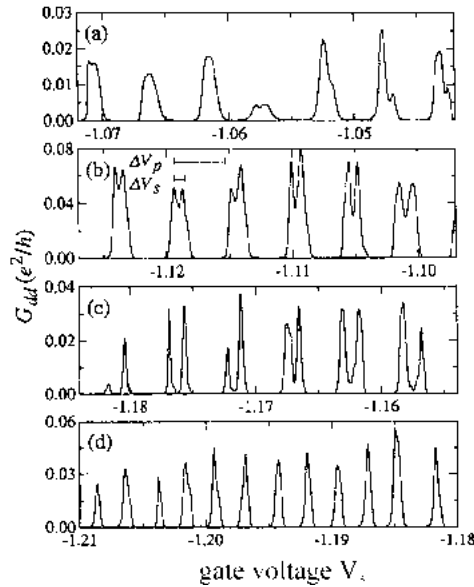


Figure 4.4. Double dot conductance  $G_{dd}$  vs. gate voltage  $V_s$  for increasing inter-dot coupling. Coupling splits conductance peaks, with split peak separation  $\Delta V_s$  proportional to the interaction energy  $E_{int}$ . Inter-dot conductance in units of  $e^2/h$  is in (a) 0.03, in (b) 0.88, in (c) 1.37, and in (d) 1.94. (From Waugh *et al.* [102].)

different charge configurations  $(N_1, N_2)$ . Plots of the electrostatic energy for zero inter-dot coupling are shown as the solid lines in Fig. 4.3(b). Because equal charges are induced by the gates in the experiment, unpolarized configurations with equal numbers of electrons, (0,0) and (1,1), have lowest energy. If only one electron is added to the array, and we assume the absence of inter-dot tunneling, it must necessarily reside on one dot or the other. This results in the polarized configurations, (1,0) and (0,1), with excess electrostatic energy. A conductance trace for this case shows the periodicity associated with a single dot, as illustrated in (c). Inter-dot coupling, either tunnel coupling or electrostatic, acts to reduce the energy of the polarized configurations, as indicated by the dashed curve in (b), causing conductance peaks to split, as indicated in (d). When the polarization energy is completely destroyed, the dashed curve in (b) touches the horizontal axis, and the peak spacing saturates at half the original value.

By calibrating the inter-dot tunnel conductance vs. gate voltage Waugh *et al.* [102] demonstrated that the peak splitting was strongly correlated with the inter-dot tunnel conductance  $G_{int}$ , increasing from a small value for  $G_{int} \cong 0$  to saturation for  $G_{int} \cong 2e^2/h$ . Thus the quantization of charge on individual dots is completely destroyed by one quantum of inter-dot conductance. Intuitively, one might expect that the inter-dot capacitance  $C_{int}$  diverges as the constriction joining the dots is opened, and this approach has been used to analyze coupled dot data with orthodox charging theory. However, for lateral dots the inter-dot capacitance increases more slowly than logarithmically with inter-dot spacing. Thus the inter-dot capacitance remains essentially constant even when the inter-dot tunneling changes exponentially fast. Numerical simulations [119] of the actual experimental geometry confirm these arguments. (Note that the capacitance per unit length  $L$  between two thin co-planar rectangular metal strips of width  $w$  and separation  $d$  in a medium with dielectric constant  $\epsilon$  is  $C/L = (2\epsilon/\pi)\ln(2w/d)$  for  $L \gg d$ .)

In the experiments discussed in this section we can ignore effects from the single-particle states. The central issue here is the destruction of charge quantization by tunneling. For single dots, the destruction of charge quantization by increasing the tunnel conductances was addressed early on by Kouwenhoven *et al.* [18], and Foxman *et al.* [80]. As the tunnel conductance  $G$  to the leads increases, the linewidth of the peaks becomes lifetime broadened (e.g. see Fig. 3.2) and the Coulomb blockade is destroyed when  $G \cong 2e^2/h$  [18]. To analyze data such as these Matveev [115] extended earlier theoretical work on charge fluctuations in metal junctions [56,108-111] to the few channel case appropriate for dots. Matveev considered a single dot with many electrons connected to the surrounding reservoir by a single 1D lead. Using a Luttinger liquid approach he calculated the interaction energy vs. tunneling rate for the

strong tunneling limit and confirmed that the quantization of charge on the dot and the associated energy were completely destroyed when the lead conductance reached exactly  $2e^2/h$ .

Matveev *et al.* [117] and Golden and Halperin [116,118] extended the single dot results to address the case of two quantum dots connected by a 1D lead but isolated from the surrounding reservoir. The initial work by both groups [116,117] achieved similar results, and both found good agreement with the experiment [102]. Later the calculations were extended to include higher order terms [118]. To compare theory with data like Fig. 4.4, Golden and Halperin [116,118] express their results for the interaction energy  $E_{int}$ , the analog of the molecular binding energy, in terms of a normalized energy shift:

$$f(\rho) = \frac{4E_{int}(\rho)}{E_{C2}\rho^2} \quad (4.1)$$

where  $0 < \rho \leq 1$  is the difference in induced charge between the two dots in units of  $e$ , and  $E_{C2} = e^2/(C+2C_{int})$  is the charging energy of one of the two dots including the effect of the inter-dot capacitance  $C_{int}$ . For unpolarized dots  $\rho = 1$ , as discussed in Ref. 116, and  $f(\rho)$  is equal to the fractional peak splitting  $f = \Delta V_s/\Delta V_{sat}$ . In the weak tunneling limit the fractional peak splitting is [118]:

$$f \cong \frac{2\ln 2}{\pi^2} N_{ch}g + 0.1491N_{ch}g^2 - 0.00980N_{ch}^2g^2 \quad (4.2)$$

where  $N_{ch}$  is the number of channels,  $N_{ch} = 2$  for one spin degenerate mode, and  $g = G_{int}/(N_{ch}e^2/h)$  is the dimensionless inter-dot conductance per channel. In the strong tunneling limit  $0 < 1-g \ll 1$ , the peak splitting for  $N_{ch} = 2$  becomes [118]:

$$f \cong 1 + 0.919(1-g)\lg(1-g) - 0.425(1-g) \quad (4.3)$$

Below we compare these functions to measurements.

Tunnel-coupled double dots are controlled by three parameters, the two gate voltages  $V_{g1}$  and  $V_{g2}$  and the inter-dot tunnel conductance  $G_{int}$ . Data on tunnel-coupled double dots in series [102,103,106,107] initially consisted of 2D slices through this 3D parameter space. In order to map out the full 3D pattern Livermore *et al.* [104] conducted new experiments on a coupled dot structure with two nominally identical dots, otherwise similar to Fig. 4.3(a). The two gate voltages  $V_{g1}$  and  $V_{g2}$  were swept in a raster pattern while the series conductance  $G_{dot}$  through the double dot was measured to create an image of

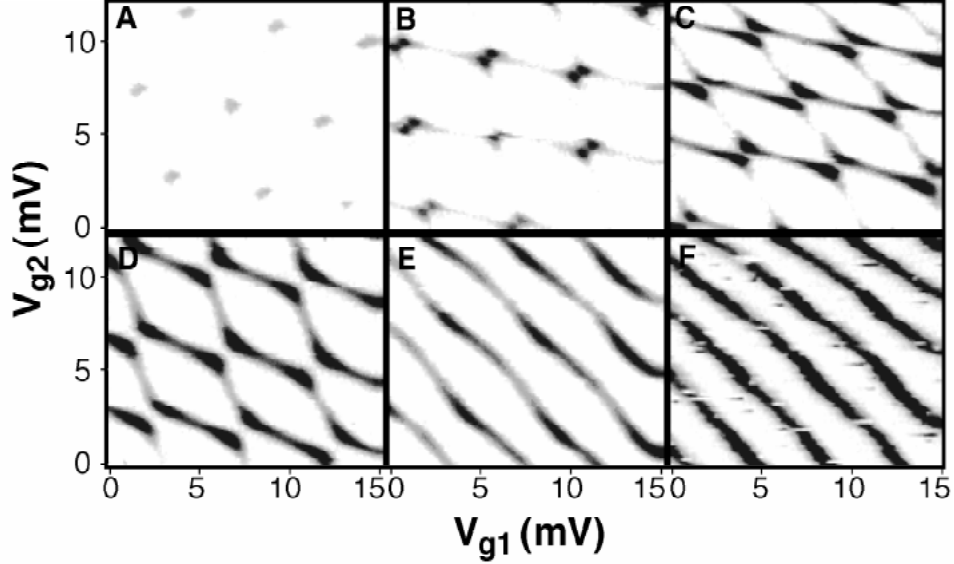


Figure 4.5. Logarithm of double dot conductance as a function of gate voltages  $V_{g1}$  and  $V_{g2}$ , which are offset to zero. Dark indicates high conductance; white regions represent low conductance. Panels are arranged in order of increasing inter-dot conductance  $G_{int}$ , which in units of  $2e^2/h$  is in (a) 0.22, in (b) 0.40, in (c) 0.65, in (d) 0.78, in (e) 0.96, and in (f) 0.98. (From Livermore *et al.* [104].)

the conductance pattern for fixed  $G_{int}$ . This procedure was repeated for a series of values for  $G_{int}$ .

Figures 4.5(a) to (f) present conductance images for inter-dot tunnel conductances increasing from a small value  $G_{int} = 0.22G_Q$  in (a) to  $G_{int} = 0.98G_Q$  in (f). This series of images presents a complete picture of how the pattern of  $G_{dot}$  evolves with inter-dot tunneling. In (a) the effects of inter-dot conductance are small, and the pattern is a hexagonal array of points, as expected for two capacitively coupled dots in series. Close examination reveals a small splitting of each point due to the inter-dot capacitance  $C_{int}$ . Within each hexagon,  $N_1$  and  $N_2$  are well defined. Compared with data from capacitively-coupled parallel dots in Fig. 4.2, the pattern for series dots differs in that conductance only occurs at the points where two sides of each hexagon intersect. As discussed above, this follows from the requirement that the number of charges on both dots must be able to change simultaneously in order for transport to occur.

As the inter-dot tunnel conductance increases, the dot conductance pattern in Fig. 4.5 changes dramatically. At  $G_{int} \cong G_Q$  in (f) the conductance pattern

becomes an array of lines corresponding to the Coulomb blockade for a single large dot. It is convenient to change gate voltage variables from  $V_{g1}$  and  $V_{g2}$  to the average gate voltage  $V_{av} = (V_{g1} + V_{g2})/2$ , and the difference  $V_{diff} = V_{g1} - V_{g2}$ . The average  $V_{av}$  induces charge equally on both dots and increases the total charge, whereas the difference  $V_{diff}$  induces polarization in the double dot system and leaves the total charge unchanged. The pattern in (f) shows an array of lines perpendicular to the  $V_{av}$  direction which separate regions defined by integer values of the total double dot charge  $N_{tot} = N_1 + N_2$ . The pattern in (f) is insensitive to  $V_{diff}$  because the dots have effectively joined into one large dot. The evolution of the conductance patterns between the weak and strong tunneling limits shows how inter-dot tunneling changes transport. As the inter-dot tunnel conductance increases, the condition that both  $N_1$  and  $N_2$  are quantized relaxes into a single condition that the total charge  $N_{tot} = N_1 + N_2$  is quantized. Between these two extremes the conductance grows steadily out from the array of points in (a) along the boundaries between configurations with different total charge  $N_{tot}$ , and the shape of these boundaries changes from the zigzag pattern for weak tunneling to straight lines in (f).

The splitting between the lines of conductance in Fig. 4.5 measures the dot interaction energy predicted by theory [116-118] and thus determines an analog of the molecular binding energy. The fractional splitting  $f = 2\Delta V_s / V_p$  is the ratio of the minimum separation  $\Delta V_s$  between lines of conductance along the  $V_{av}$  direction to the saturated splitting  $V_p/2$  where  $V_p$  is the period in (a) along the  $V_{av}$  direction. The inter-dot tunnel conductance  $G_{int}$  was independently

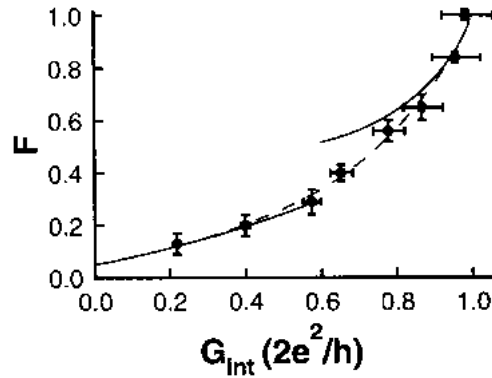


Figure 4.6. Measured fractional splitting  $F$  (circles), theoretical fractional splitting (solid lines), and theoretical interpolation (dotted line) plotted as a function of inter-dot tunnel conductance  $G_{int}$ . Theoretical splitting includes both splitting due to inter-dot tunneling and the small splitting due to interdot capacitance. (From Livermore *et al.* [104].)

determined by separate measurements of the center point contact with the two outer point contacts open. Fig. 4.6 plots measurements of the fractional splitting  $f$  vs.  $G_{int}$ , together with theory [118] in the weak and strong tunneling limits (solid curves) and an interpolation between these limits (dashed curve). As shown, the agreement between experiment and theory is excellent, providing strong support for the charge quantization theory. Similar agreement was also found for measurements by Adourian *et al.* [105] for two tunnel-coupled quantum dots in parallel. A somewhat different approach was used by Molenkamp *et al.* [120] to analyze their experiments on a parallel dot system.

So far we have discussed only linear response transport, measured for very small source-drain voltages. Crouch *et al.* [121] have measured the Coulomb blockade for series double dots via non-linear  $I$ - $V_{sd}$  curves. The devices used were essentially a double dot version of the device in Fig. 4.3(a). The two side gates were tied together to induce equal charges on both dots, and the differential conductance  $G_{dif} = dI/dV_{sd}$  was measured as both the source-drain voltage  $V_{sd}$  and gate voltage were swept. Figs. 4.7(a) to (d) present gray scale plots of  $G_{dif}$  vs.  $V_{sd}$  and vs. gate voltage as the inter-dot tunnel conductance is increased from  $G_{int} \cong 0$  in (a) to  $G_{int} \cong 2e^2/h$  in (d). The diamond pattern in (a)

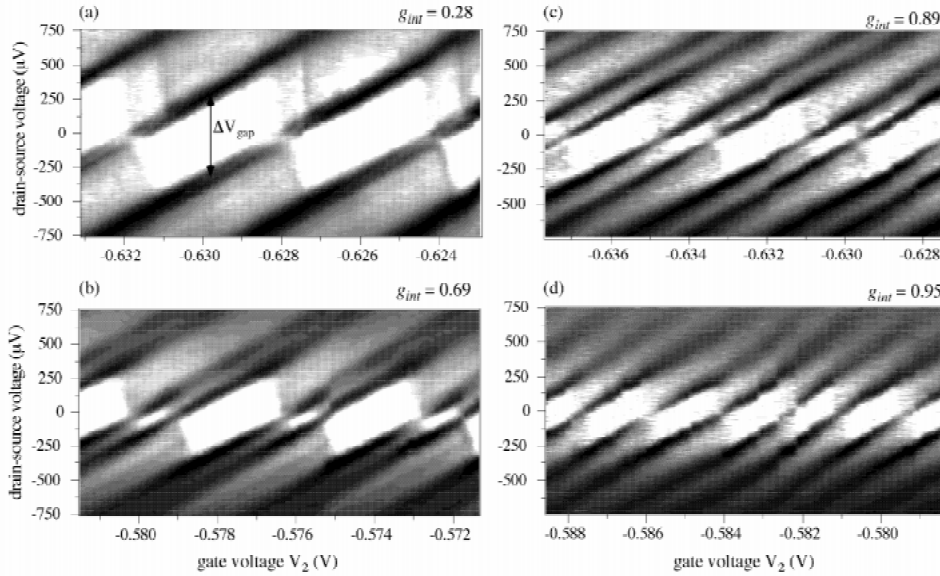


Figure 4.7. Differential conductance  $G_{dif}$  on a logarithmic scale as function of source-drain voltage and side gate voltages  $V_{g1} = V_{g2}$  for inter-dot conductances  $g_{int}$  (units of  $2e^2/h$ ) in (a) 0.28, in (b) 0.69, in (c) 0.89, and in (d) 0.95. (From Crouch *et al.* [121].)

is essentially that measured for a single dot (see section 3.2), showing a single well developed region of Coulomb blockade. The period in gate voltage corresponds to adding one electron to each dot. As the inter-dot tunnel conductance increases, a second smaller region of Coulomb blockade develops. This second region grows with  $G_{int}$  until the evolution saturates in (d) at a pattern for a single large dot with half the gate voltage periodicity. This evolution is qualitatively in accord with what one would expect from linear-response data above and from charge quantization theory. A quantitative comparison of theory and experiment [121] requires an additional self-consistent calculation [96] to include the effects of inter-dot polarization induced by  $V_{sd}$ , when this is done very good agreement is found.

In summary, the quantization of electronic charge produces frustration in electrostatically-coupled dots which is relaxed by inter-dot tunneling, resulting in a reduction in the ground state energy analogous to a molecular binding energy. Frustration arises because the optimal charges induced by gates on coupled dots are not generally integral multiples of the electronic charge. Forcing integral occupation increases the electrostatic energy. Inter-dot tunneling destroys charge quantization on individual dots and allows the charge distribution to reach its optimal configuration. This picture is quantitatively confirmed by comparison of theory with linear-response measurements on series and parallel coupled quantum dots and nonlinear current-voltage measurements on series coupled dots.

#### 4.3. SPECTROSCOPY WITH COUPLED DOTS.

Single quantum dots display well defined discrete energy states as described in sections 2 and 3. For semiconductor dots with Fermi energy  $E_F \sim 10$  meV and  $N \sim 100$  electrons the separation between the 0D-states is  $\Delta E \sim 100$   $\mu$ eV which exceeds  $k_B T$  for  $T < 1$  K. The values of energy states are of interest for specific quantum dot structures and their statistics are of interest for comparison with quantum chaos theory (see section 6). The resolution of tunnel measurements of the 0D-states in single dots is limited by thermal broadening of the Fermi energy in the leads.

Van der Vaart *et al.* [103] have demonstrated an improved spectroscopic technique using 0D-states in the second dot of a coupled dot structure to remove the effects of thermal broadening in the leads. Fig. 4.8(a) shows the coupled dot device, which is also defined in the 2DEG of a GaAs/AlGaAs heterostructure. The dots are a few times smaller than the ones discussed in section 4.2 such that here the 0D-states are well resolved. In contrast to the experiments in section 4.2, the tunneling rate between dots is made very weak,

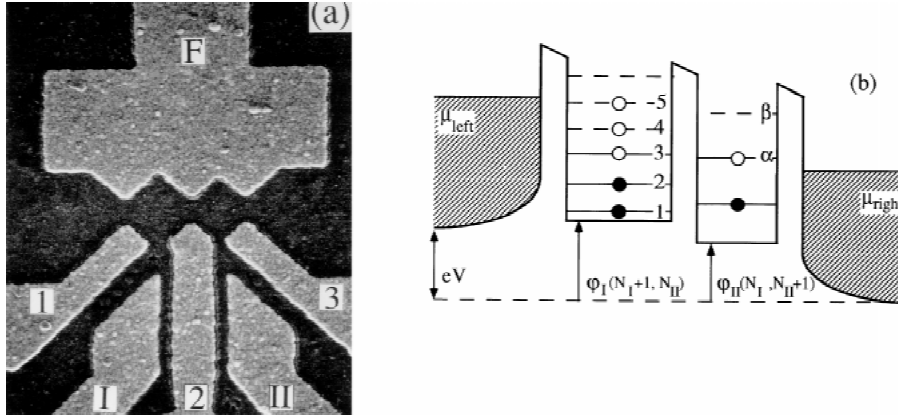


Figure 4.8. (a) SEM micrograph of the double dot with lithographic dimensions of  $320 \times 320 \text{ nm}^2$  (left dot) and  $280 \times 280 \text{ nm}^2$  (right dot). (b) Schematic potential landscape of the double quantum dot, where  $\mu_{left}$  and  $\mu_{right}$  denote the electrochemical potentials of the left and right reservoirs and  $V$  the bias voltage across the double dot. The 0D-states in dot I are denoted by levels 1 to 5 and in dot II by levels  $\alpha$  and  $\beta$ . (From van der Vaart *et al.* [103].)

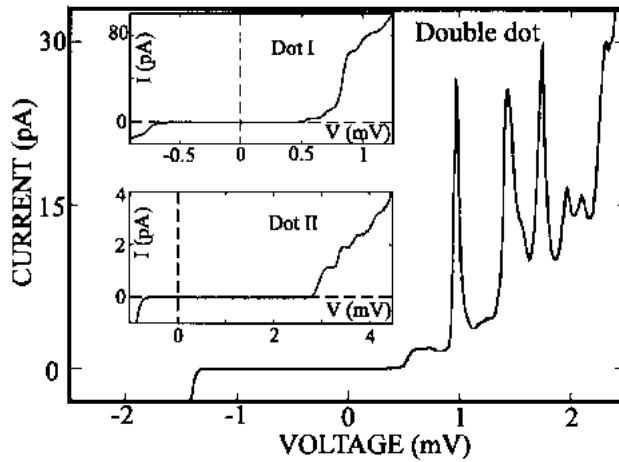


Figure 4.9.  $I$ - $V$  curve of the double dot, showing sharp resonances in the current when two 0D-states line up. Upper inset:  $I$ - $V$  curve of dot I. Lower inset:  $I$ - $V$  curve of dot II. Both insets show a suppression of the current at low voltages due to Coulomb blockade and a stepwise increase of the current due to the discrete energy spectrum of a single dot. (From van der Vaart *et al.* [103].)

as well as tunneling to the leads. The lifetime in each dot is therefore long and the 0D-states have a broadening much smaller than their separations. Although, the Coulomb blockade also exists for both dots, we here describe only the additional influence of the 0D-states. As indicated in Fig. 4.8(b) transport through the series double dot begins as an electron tunnels in from the left lead to the 0D-state 3 in the left dot. If one of the unoccupied states of the right dot, state  $\alpha$  in (b), lines up with state 3, then the electron can tunnel elastically to the right dot and eventually leave through the right barrier. So, even if the conditions for Coulomb blockade are fulfilled, if none of the 0D-states in the right dot line up with a 0D-state in the left dot the tunneling rate is strongly suppressed. Thus transport through the dot should show sharp features limited only by the lifetime of the single-particle states, not the temperature.

The  $I-V_{sd}$  curve in Fig. 4.9 demonstrates how narrowing occurs. The two insets show  $I-V_{sd}$  traces for dots I and II individually; both show steps which occur when the Fermi level in the lead passes through a 0D-state. The average spacing between levels is found to be  $\Delta E = 125 \mu\text{eV}$  for dot I and  $\Delta E = 225 \mu\text{eV}$  for dot II. When the gates forming both dots are energized, the series double dot shows a very different  $I-V_{sd}$  characteristic. Instead of steps we now see sharp peaks which occur at source-drain voltages for which a 0D-state in the right dot and one in the left dot line up; the current is suppressed at other source-drain voltages. Analogous structure is seen in traces of conductance vs. gate voltage at finite  $V_{sd}$ , for which each conductance peak breaks up into a series of peaks, each associated with a specific pair of 0D-states in the left and right dots. Fitting of one of these resonances shows that the lineshape is Lorentzian with an additional broadening corresponding to a temperature of 35 mK [103]. The fact that this temperature is several times smaller than the electron temperature in the leads demonstrates that the discrete states in one dot act to remove thermal broadening due to the leads [86,122].

#### 4.4. COHERENT TUNNELING THROUGH QUANTUM DOTS

The coherence of electronic states becomes an important issue whenever wave-like aspects of electrons are important. In the early 1980's researchers were surprised to find that electron waves traveling through disordered metallic conductors exhibited wave interference phenomena at low temperatures, in the form of weak localization and universal conductance fluctuations, over length scales much greater than the elastic scattering length [123-125]. This interference demonstrated that coherent transport can occur in a Fermi liquid even though the particles interact strongly via Coulomb forces. A considerable body of experimental and theoretical work led to a detailed quantitative understanding of coherence in disordered conductors. Quantum dots also show

conductance fluctuations and analogs of weak localization, which are associated with coherent interference inside the dots (see section 6), but our understanding of the coherence times is not yet as well developed as for open structures.

The issue of coherence is critical for applications of quantum dots to possibly construct quantum computers [87,88]. The theoretical speed of quantum computers follows from the fact that they coherently process superpositions of wavefunctions, and the original approaches required that processing remain coherent across the computer during the entire calculation. The resulting experimental constraints are truly daunting for useful calculations and threaten to place the implementation of quantum computers as hardware far into the future. Recent advances in quantum error correction relax these requirements and create hope for somewhat nearer-term implementations.

Tunneling in experiments, especially in the weak tunneling regime, is generally considered to be an incoherent process. Theoretically this need not be true, but the electrons in quantum dots interact with many other particles: charged impurity atoms, electrons in surrounding gates, phonons in the substrate, and photons from the environment, for example. If the dynamics of these particles are not included in the description of the many-body system which comprises the quantum dot (or the quantum computer), then the interaction between the electrons on the dot with these “external particles” effectively destroys the coherent behavior of the electrons on the dot. Currently, the issue of coherence of electron states inside quantum dots and the coherence of tunneling processes is actively discussed but relatively few data are available [36,82].

Recent experiments [126,127] have made an important step in our understanding of coherence for tunneling experiments on quantum dots by demonstrating that part of the tunnel current is coherent. Figs. 4.10(a) shows an SEM photograph of the device of Yacoby *et al.* [126], which consists of a GaAs/AlGaAs quantum dot with two adjustable quantum point contacts placed inside a ring which forms two arms of an electron interferometer. The quantum dot was placed in the tunneling regime with an electron temperature  $\sim 80$  mK. At this temperature for this size dot, tunneling normally takes place through a single quantum level of the dot. The coherence length of electrons in the ring was larger than its circumference, and interference between electron waves tunneling through the dot and passing along the open arm of the interferometer was detected via Aharonov-Bohm (AB) oscillations in the ring current as a perpendicular magnetic field  $B$  was swept.

Coherence in the tunneling current is demonstrated by the data of Fig. 4.10(b), which is a trace of the ring current vs. plunger gate voltage  $V_P$  for

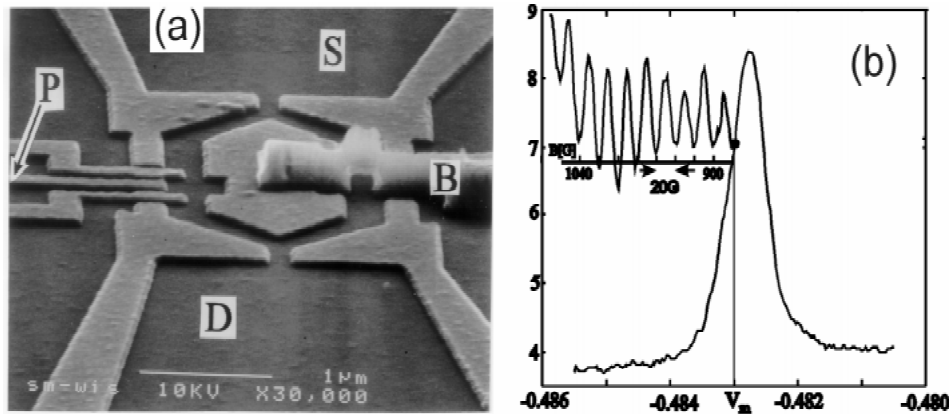


Figure 4.10. (a) An SEM micrograph of an Aharonov-Bohm ring with a quantum dot placed in the left arm. The light regions are the metal gates. The central metallic island is biased via an air bridge (B) extending to the right. (b) One of the ring's current peaks as a function of the gate voltage applied to P in (a). At the top left the current is plotted as a function of magnetic field (the magnetic field increases to the left) at the fixed gate voltage  $V_m$  showing Aharonov-Bohm oscillations. The large current of the right arm is subtracted. (From Yacoby *et al.* [126].)

small source-drain voltage. The Coulomb blockade for the dot creates sharp conductance peaks in the ring current for fixed magnetic field. When the gate voltage is fixed on the side of a conductance peak and the magnetic field is swept instead, periodic AB-oscillations are observed, with a period corresponding to the ring area, demonstrating the existence of a coherent component of the current tunneling through the dot. The phase of the AB-oscillations was the same for different Coulomb blockade conductance peaks, but changed abruptly at the top of each peak as expected for a resonant phenomenon like tunneling through a single level.

The observation of coherence in tunneling through a single dot is an important step, but many issues remain open in the study of coherence in single and coupled quantum dots and quantum dot circuits. These include a quantitative understanding of the coherence time of electron states inside single dots and an understanding of coherence of molecular electronic states inside tunnel-coupled quantum dots and quantum dots circuits. This knowledge will permit reasonable assessments of the feasibility of quantum computation using coupled dot circuits in the future.

## 5. Vertical quantum dots.

This section deals with the transport properties of a single vertical semiconductor quantum dot which is weakly coupled to the reservoirs via heterostructure tunnel junctions. We focus on Coulomb interactions and quantum mechanical effects, both of which become enhanced in a small dot containing just a few electrons ( $N \leq 20$ ). First, in section 5.1, we describe the vertical dot tunnel structures and the technique of single electron spectroscopy, while section 5.2 addresses atom-like properties observed in a quantum dot with a two-dimensional harmonic potential.

### 5.1. SINGLE ELECTRON SPECTROSCOPY OF A FEW-ELECTRON DOT.

Coulomb oscillations are usually periodic. However, in a small dot containing just a few electrons, both the electron-electron interactions and quantum confinement effects become sufficiently strong that the spacings between the Coulomb oscillation peaks become irregular [50,128-131]. Lateral dot structures, discussed in sections 3 and 4, are not suitable for defining a system of only a few electrons because the tunnel barriers are formed by a depletion potential. This potential is significantly affected by the center or plunger gate potential close to ‘pinch-off’. In practice, when  $N < \sim 25$  the tunnel barriers become too large for observing a current, even at resonance. In vertical dot structures, this problem is overcome by the use of heterostructure barriers. These tunnel barriers are abrupt and thin, and are only weakly affected by a gate potential. Furthermore, the lateral geometry in a vertical dot is sufficiently well defined to allow for the formation of systematically degenerate sets of 0D-states in the dot [31,132]. However, there are inherent technical difficulties in squeezing the vertical dot, i.e. varying the number of electrons. To date there only have been a few reports of how these difficulties have been solved. These include transport through two-terminal dots [133-137], transport through three-terminal gated dots [130,131,138-142], and capacitance measurements on two-terminal gated dots [15,50].

Fig. 5.1 shows a schematic diagram of a two-terminal quantum dot structure and the Coulomb staircase observed by Schmidt *et al.* [136]. The GaAs dot is located between the two AlGaAs barriers. The two barriers have different widths, which promotes the accumulation of electrons in the dot for negative  $V_{sd}$  and the escape from the dot for positive  $V_{sd}$  [51,143]. For negative  $V_{sd}$  a current step occurs whenever an extra electron is trapped in the dot, while for positive  $V_{sd}$  a sharp current peak appears due to resonant tunneling through a single-particle 0D-state [133-137,144,145]. Since the dot is depleted ( $N = 0$ ) at  $V_{sd} = 0$  the first step occurs when  $V_{sd}$  is increased sufficiently such that the

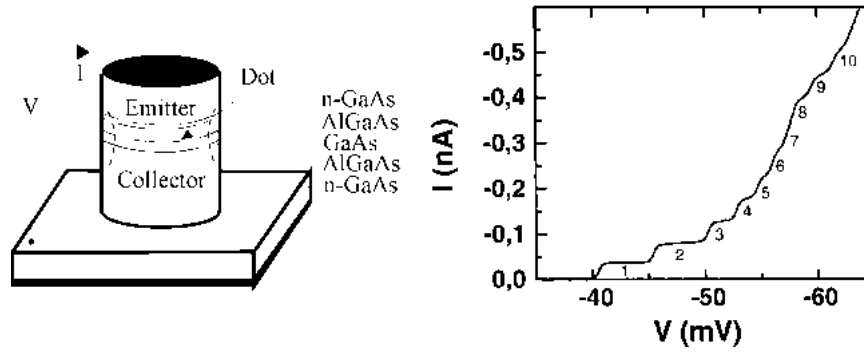


Figure 5.1. (a) Schematic diagram of a two-terminal quantum dot device and (b) the Coulomb staircase in the current vs. source-drain voltage at  $B = 0$  T. The fabricated dot diameter is  $0.35 \mu\text{m}$ , but due to depletion effects the electrons experience a dot which is several times smaller. (From Schmidt *et al.* [136].)

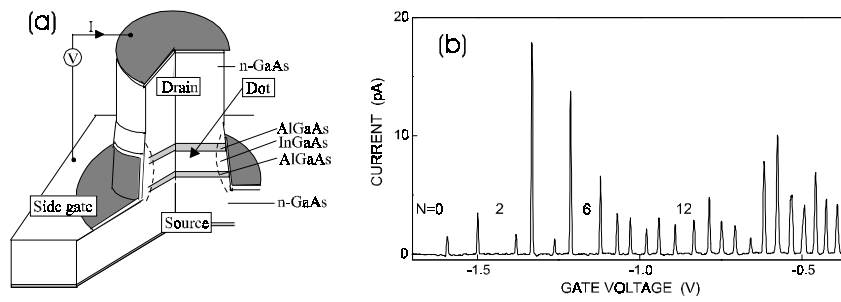


Figure 5.2. (a) Schematic diagram of the gated quantum dot device and (b) the Coulomb oscillations in the current vs. gate voltage at  $B = 0$  T observed for a  $0.5 \mu\text{m}$  diameter dot. (From Tarucha *et al.* [131].)

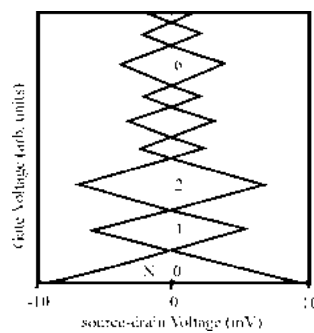


Figure 5.3. Measured size of the Coulomb gap versus gate voltage. The diamonds represent the source-drain voltage value at which current starts to flow. The sizes of the diamonds directly correspond to the peak spacings in Fig. 5.2(b). (From Kouwenhoven *et al.* [146].)

electrochemical potential of one of the reservoirs aligns with the  $N = 1$  energy state. At  $V_{sd} = -40$  mV in Fig. 5.1(b) the first electron enters the dot. The subsequent steps each represent the addition of one more electron. This charging process is in the nonlinear transport regime (see section 3.3). From the voltage interval  $\Delta V_{sd}$  between the  $N$ th and  $(N+1)$ th steps, an addition energy needed to put an extra electron in the  $N$ -electron dot,  $\Delta\mu$ , can be deduced since  $\Delta\mu = \beta e \Delta V_{sd}$ , where  $\beta < 1$  is a factor to convert source-drain voltage to energy. The large values of  $\Delta V_{sd}$ , compared to lateral dots, arise from the strong Coulomb interactions and quantum mechanical effects in the few-electron system.

Fig. 5.2 shows a schematic diagram of a vertical dot and the Coulomb oscillations observed at  $B = 0$  T [131]. This dot has a circular Schottky gate placed on the side of the mesa close to the dot region, and is used to squeeze the dot. The dot is made from InGaAs, which has a narrower band gap than the GaAs in the contacts. The inclusion of In reduces the conduction band bottom in the dot below the Fermi level in the contacts. This means that electrons are accumulated in the dot even when no voltages are applied. This allows to study linear transport properties. (Note that for the device in Fig. 5.1 both the dot and contacts are made from GaAs.) The current  $I$  vs. gate voltage  $V_g$  measured at small  $V_{sd}$  shows clear Coulomb oscillations.

In Fig. 5.3 the measured size of the Coulomb gap (i.e. the source-drain voltage at which current starts to flow) is plotted as a function of gate voltage [146]. The vertical  $V_{sd} = 0$  axis corresponds directly to the data in Fig. 5.2(b). Note that, for instance, the size of the peak spacings along the  $V_{sd} = 0$  axis are the same as the peak spacings for the corresponding  $N$  in Fig. 5.2(b). These irregular peak spacings at  $V_{sd} = 0$  lead to correspondingly irregular sizes for the diamond shaped Coulomb gaps. This is in contrast to the regularly shaped diamonds in Figs. 3.7(b) and 4.7, which were measured on lateral dots. As we discuss in the next section these irregularities can be described to the small number of electrons in vertical dots. Note that the Coulomb diamond in the  $N = 0$  region never closes when we continue to make the gate voltage more negative, implying that the dot is indeed empty. From this observation the absolute values of  $N$  can be identified and used to label the spaces between the current peaks.

Single electron effects are observed also in ac capacitance measurements [15,50]. Fig. 5.4 shows a schematic diagram of the vertical dot structure and the capacitance signal observed by Ashoori *et al.* [15]. The dot is located in the GaAs quantum well and its size is controlled by the top gate voltage. Electron exchange occurs only through the barrier to the bottom electrode. The ac capacitance measurement shows a sequence of peaks as a function of top plate voltage. Note that although this is a two terminal device, the capacitance

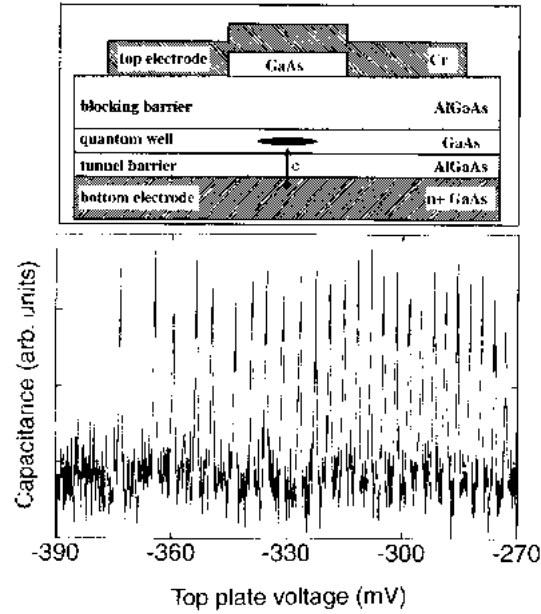


Figure 5.4. Schematic diagram of the dot structure prepared for capacitance spectroscopy, and the capacitance data vs. gate bias (top plate voltage) characteristic at  $B = 0$  T. The dot is the black disk between the two AlGaAs barriers. (From Ashoori *et al.* [15].)

measurements are in the linear response regime. The first capacitance peak on the left represents the first electron entering the dot. Thus, the  $N$ th peak position in top plate voltage is directly related to  $\mu(N)$ . The capacitance peaks are more widely spaced as the dot approaches the “pinch-off” point. This also reflects the increase in both the Coulomb interactions and the quantum mechanical effects when  $N$  approaches zero. We discuss the  $B$ -field dependence of the capacitance signal in section 7.

## 5.2. SHELL STRUCTURE AND HUND’S RULE.

If a dot has the shape of a circular disk and the confining potential is harmonic, then we have a system with a high degree of symmetry. This symmetry leads to sets of degenerate single-particle states which form a *shell structure*. Such a shell structure for circular 2D potentials was predicted by self-consistent calculations [147]. Here, we discuss the formation and electron filling of a shell structure by comparing a non-interacting model with models that include Coulomb interactions and exchange interactions.

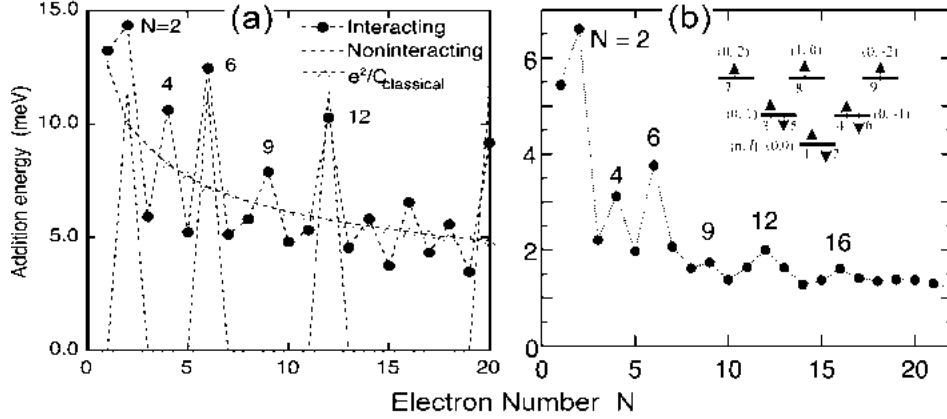


Figure 5.5. Addition energy vs. electron number. (a) Hartree-Fock calculation for a circular dot with harmonic lateral potential (filled circles). The open circles show the single-particle excitation energy, and the open triangles give the charging energy from a classical self-capacitance model. (From Tamura *et al.* [148].) (b) The filled circles are the measured addition energies derived from the Coulomb oscillations in Fig. 5.2. The inset depicts the filling of the shells for  $N = 9$  in line with Hund's rule.

Fig. 5.5(a) shows a comparison between energies of non-interacting single-particle states, classical charging energies derived from a self-capacitance model, and those derived from a Hartree-Fock (HF) calculation. The results are shown in the form of addition energies with respect to  $N$  [148]; see Eq. (2.2) for the addition energy in the constant interaction model. For a circularly symmetric 2D confinement potential the quantum numbers for the single-particle states are conveniently described by a radial quantum number  $n = 0, 1, 2, \dots$  and an angular momentum quantum number  $\ell = 0, \pm 1, \pm 2, \dots$ . We consider a harmonic confinement potential  $V(r) = \frac{1}{2}m^* \omega_0 r^2$  for which the non-interacting Schrödinger equation has the following analytic solutions for the eigenenergies  $E_{n\ell}$ :

$$E_{n\ell} = (2n + |\ell| + 1)\hbar\omega_0 \quad (5.1)$$

The calculation in Fig. 5.5(a) is performed by taking  $\hbar\omega_0 = 2Ry^*$  ( $= 11.5$  meV for the InGaAs dot in Fig. 5.2), where  $Ry^*$  is the effective Rydberg constant which is a measure for the interaction energy. It follows from Eq. (5.1) that  $E_{n\ell}$  has degenerate sets of states, which are separated by  $\hbar\omega_0$  from each other and which are completely filled for  $N = 2, 6, 12, 20$ , etc. For these special values of  $N$  the addition energy is maximal. These maxima persist when interactions are included in a HF approximation. However, in addition, the HF calculation also

reveals maxima in the addition energy at  $N = 4, 9$  and  $16$ . For these  $N$  values, respectively, the second, third and fourth shells are half filled with parallel spins in accordance with *Hund's rule*. Half filled shells correspond to a maximum spin state, which, due to exchange interaction, has relatively low energy. These atom-like features persist as long as  $\hbar\omega_o$  is comparable to, or larger than, the interaction energy.

Fig. 5.5(b) shows the addition energy as a function of  $N$  obtained from the data shown in Fig. 5.2. The spacing between the  $N$ th and  $(N+1)$ th current peaks reflects the energy to add one more electron to a dot containing  $N$  electrons. For example, the energy to add the third electron to an  $N = 2$  dot can be derived from the spacing between the second and third peak. For each value of  $N$  a factor to convert gate voltage to addition energy (i.e. the factor  $eC_g/C$  in Eq. 2.1) can be determined from the Coulomb diamonds in Fig. 5.3. The addition energy generally becomes larger as  $N$  decreases and has large maxima for  $N = 2, 6$  and  $12$ , and also relatively large maxima for  $N = 4, 9$  and  $16$ . This  $N$ -dependence of the addition energy is consistent with the HF calculation in Fig. 5.5(a) and reflects the complete filling of the first, second and third shells as well as the half filling of the second, third and fourth shells with parallel spins. The inset in (b) shows schematically the occupation of the lowest three shells for  $N = 9$ . The actual value of the addition energy is smaller than that in the HF calculation, because  $\hbar\omega_o$  derived from the experiment (see below) is smaller than that used in the calculation

The electronic states are expected to be significantly modified by a magnetic field,  $B$ , applied parallel to the tunneling current. Fig. 5.6 shows the  $B$ -field dependence of the position of the current peaks. The positions of the first three peaks depend monotonously on  $B$ , whereas the other peaks oscillate back and forth a number of times. The number of “wiggles” increases with  $N$ . Close inspection of the figure reveals that the current peaks generally shift in pairs with  $B$ . The spacing between the peaks when  $N$  is odd is nearly constant, whereas the peak spacing varies strongly with  $B$  when  $N$  is even. This even-odd effect is particularly clear around 3.5 T, where all the peaks are evolving smoothly with  $B$ . Here the peak spacing alternates between “large” for even  $N$  and “small” for odd  $N$ . Most of these features can be explained within a single-particle framework.

If we assume a parabolic confinement, the non-interacting Schrödinger equation can be solved in the presence of a magnetic field. This calculation was first performed in 1928 and the eigenenergies are known as Darwin-Fock states [149,150]:

$$E_{n\ell} = (2n + |\ell| + 1)\hbar\left(\frac{1}{4}\omega_c^2 + \omega_o^2\right)^{1/2} - \frac{1}{2}\ell\hbar\omega_c, \quad (5.2)$$

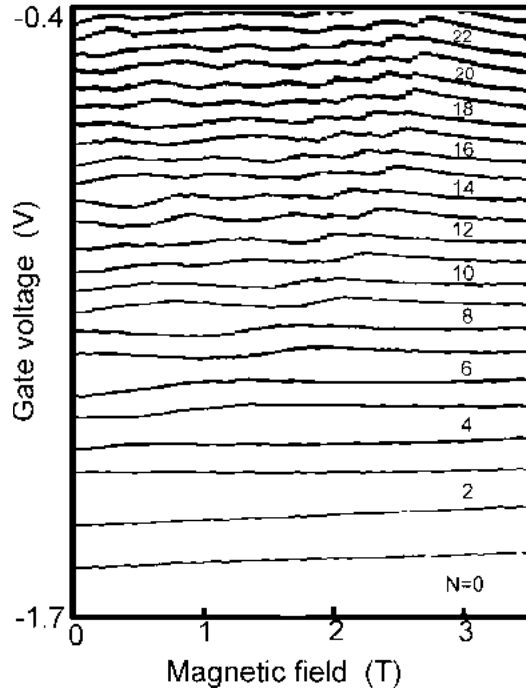


Figure 5.6. Plot of the gate voltage positions of the current peaks in Fig. 5.2 vs. magnetic field. (From Tarucha *et al.* [131].)

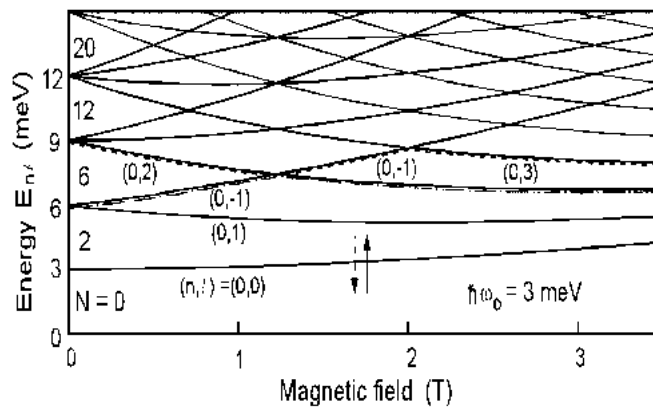


Figure 5.7. Calculated single-particle energy vs. magnetic field for a parabolic potential with  $\hbar\omega_0 = 3$  meV. Each state is two fold spin degenerate. The dashed and dot-dashed lines are discussed in the text. (From Tarucha *et al.* [131].)

where  $\hbar\omega_c = \hbar eB/m^*$  is the cyclotron energy. Fig. 5.8 shows  $E_{nl}$  vs.  $B$  calculated for  $\hbar\omega_o = 3$  meV. Spin is neglected so each state is twofold degenerate. The degeneracies at  $B = 0$  T are lifted in the presence of a  $B$ -field such that a single-particle state with a positive or negative  $\ell$  shifts to lower or higher energy, respectively. The  $B$ -field dependence of these states gives rise to an addition energy for even  $N$  that is strongly dependent on  $B$ . On the other hand, the addition energy for odd  $N$  is determined only by the effect of Coulomb repulsion. This leads to a pairing of the conductance peaks, which is evident in Fig. 5.6. In Fig. 5.7 the energy curve for the fifth and sixth electrons (dot-dashed line) predicts that these electrons undergo a transition in their quantum numbers:  $(n, \ell)$  changes from  $(0, -1)$  to  $(0, 2)$  at 1.3 T. The energy curve for the seventh and eighth electrons (dotted line) predicts that these electrons undergo transitions in  $(n, \ell)$  from  $(0, 2)$  to  $(0, -1)$  at 1.3 T and then to  $(0, 3)$  at 2T. These transitions are also seen in Fig. 5.6. However, one should keep in mind that the charging energy separates the non-interacting states of Fig. 5.7 by a value which is roughly constant in magnetic field. In a similar fashion, the quantum numbers can be identified for the other electron states. Above the  $B$ -field where the last “wiggles” occurs, the single-particle states merge into the lowest spin-degenerate Landau level (i.e. for  $n = 0, \ell \geq 0$ ). The single-particle excitation energy calculated, for example, at  $B = 3.5$  T, is still large (between 1 and 1.5 meV in Fig. 5.7) and significantly contributes to the addition energy for even  $N$ . This leads to the alternating peak spacings observed around 3.5 T in Fig. 5.6 (i.e. the spacings where the even numbers have been placed are larger than the neighboring spacings).

Fig. 5.8(a) shows the  $B$ -field dependence of the third, fourth, fifth and sixth current peaks, i.e. peaks belonging to the second shell. The pairing of the third and fourth peaks, and the fifth and sixth peaks above 0.4 T is clearly seen. However, this pairing is rearranged for  $B < 0.4$  T. In this region the third and fifth peaks, and the fourth and sixth peaks are paired. The evolution, as a pair, of the third and fifth peak for  $B < 0.4$  T is continued by the third and fourth peak for  $B > 0.4$  T. Similarly, the evolution, as a pair, of the fourth and sixth peak for  $B < 0.4$  T is continued by the fifth and sixth peak for  $B > 0.4$  T. For  $B > 0.4$  T, following the arguments related to Fig. 5.7, the third and fourth peaks are identified by the quantum numbers  $(n, \ell) = (0, 1)$  with anti-parallel spins. The fifth and sixth peaks are identified by  $(n, \ell) = (0, -1)$  with anti-parallel spins. The rearrangement of the pairing for  $B < 0.4$  T can be understood in terms of *Hund's rule*, which is well known in atomic physics [151]. Hund's rule says that degenerate states in a shell are filled first with parallel spins up to the point where the shell is half filled. This is modeled in the calculation of  $\mu(N)$  vs.  $B$  shown in Fig. 5.8(b). In this figure the quantum numbers  $(n, \ell)$  help to identify the angular momentum transitions, and the diagrams illustrate the spin

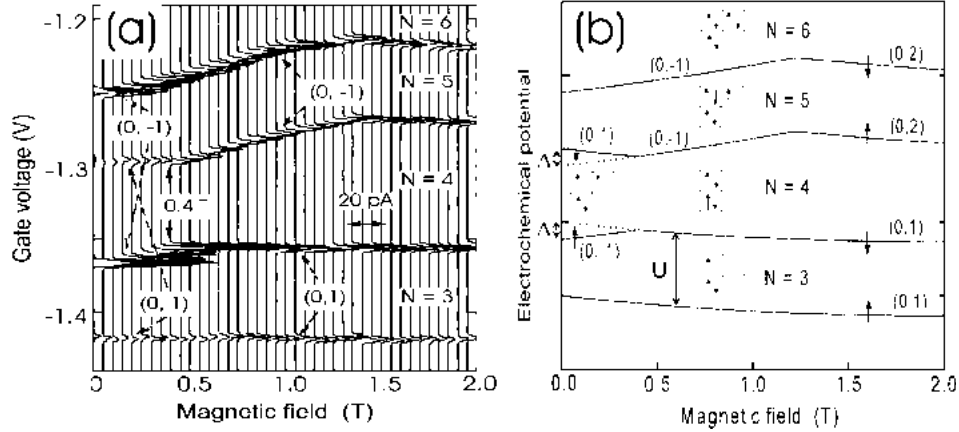


Figure 5.8. (a) Evolution of the third, fourth, fifth and sixth current peaks with magnetic field from 0 to 2 T. The original data consists of current vs. gate voltage traces for different magnetic fields, which are offset and rotated by 90 degrees. (b) Calculated electrochemical potential vs. magnetic field for the model described in the text and parameters  $U = 3$  meV,  $\Delta = 0.7$  meV, and  $\hbar\omega_0 = 3$  meV. The quantum numbers  $(n, \ell)$  are shown of the  $N$ th electron and the diagrams show the spin configurations. (From Tarucha *et al.* [131].)

configurations. In the constant interaction model, [see Eqs. (2.1) and (2.2)]  $\mu(N)$  can be written as a constant interaction energy  $U$  added to  $E_{nl}$  [152,153]. To include Hund's rule in the calculation we introduce an energy  $\Delta$ , which represents the energy reduction due to the exchange interaction between electrons with parallel spins. Specifically, for  $N = 4$ , the ground state energy is reduced if the outer two electrons have parallel spins with different angular momenta rather than anti-parallel spins with the same angular momentum.  $\mu(4)$  is thus reduced by an amount  $\Delta$  and there is a corresponding increase in  $\mu(5)$  by  $\Delta$ . This exchange effect is canceled in the presence of a  $B$ -field when the  $(0, \pm 1)$  states, which are degenerate at  $B = 0$  T, are split by an energy exceeding  $\Delta$ . This is a simple way to include exchange effects in a constant interaction model. However, for small  $N$  we find a remarkable agreement between what is seen in Fig. 5.8(a) and that predicted in (b) with  $U = 3$  meV and  $\Delta = 0.7$  meV. In this model, the addition energy for  $N = 4$  at  $B = 0$  T is expected to be larger by  $2\Delta$  than that for  $N = 3$  and 5, and this is indeed observed in Fig. 5.5(b). This simple Hund's rule model is a first correction to the constant interaction model. A more rigorous Hartree-Fock approach, or exact diagonalization of the  $N$ -electron Hamiltonian, as outlined in Refs. 73-75, 154-159, are required for a more quantitative comparison. Very recently Eto [160] has actually been able to calculate a  $B$ -field dependence of the addition

spectra that very closely duplicates the data in Fig. 5.9. These calculations thus confirm the simple model of Fig. 5.8(b).

In this section we have described that the linear transport characteristics through a 2D artificial atom reflect a shell structure, and the filling of electrons is in line with Hund's rule. The atom-like energy spectrum of the dot states is systematically modified by a magnetic field, which allows the identification of the quantum numbers of the single-particle states. Note that the observation of orbital degeneracy implies that the system is non-chaotic, which is very unusual for solid state systems. In fact, on the level of single-particle states the vertical dots are the first non-chaotic solid state devices. In the next section we return to lateral dots and discuss chaos in dots without symmetry.

## 6. Mesoscopic Fluctuations of Coulomb Blockade.

This section concerns the rather specific subject of mesoscopic fluctuations of conductance in the Coulomb blockade regime. After briefly reviewing universal conductance fluctuations in open quantum dots (6.1), we turn to discuss the newer and experimentally more challenging problem of mesoscopic fluctuations of Coulomb blockade peak heights (6.2 and 6.3), peak positions and spacings (6.4 and 6.5), and elastic co-tunneling in the valleys between Coulomb blockade peaks (6.6). At the end, some open questions and conclusions are given (6.7). Whereas transport in open quantum dots with highly conductive leads can be described in terms of quantum interference of a non-interacting electron traversing the dot via multiple diffusive or chaotic paths, in nearly isolated, Coulomb blocked quantum dots, interactions have a dominant role in transport, coexisting with large non-periodic fluctuations due to quantum interference. Nonetheless, many experimental aspects of mesoscopic fluctuations in blocked dots can be understood quantitatively within the constant interaction model where fluctuations arise from the spatial structure of single-particle 0D states.

### 6.1. CONDUCTANCE FLUCTUATIONS IN OPEN QUANTUM DOTS.

Mesoscopic conductance fluctuations typically refer to quasi-random fluctuations of the conductance of small open conductors with large conductance  $G > e^2/h$  [161-163]. These fluctuations are ubiquitous at low temperatures when the size of the system  $L$  becomes comparable to the phase coherence length  $\ell_\phi(T)$ , which can grow to several microns at temperatures below  $\sim 1$  K. Mesoscopic fluctuations are distinct from noise in that they do not depend on time, but rather depend on experimentally controllable

parameters such as magnetic field or gate voltage. Because these parameters can be swept back and forth, it is readily seen that although the fluctuations are unpredictable, like noise, they are perfectly repeatable within a single cool-down of the device – a striking instance of deterministic randomness in a quantum system. An example of mesoscopic fluctuations in an open quantum dot is shown in Fig. 6.1.

Conductance fluctuations in open conductors can be understood as interference of phase-coherent electrons traversing the sample via a number of interfering paths. The influence of an external magnetic field is to alter the relative phase of the various interfering paths, scrambling the interference “speckle” pattern and thus causing the conductance to fluctuate in a complicated, essentially random way. Less obvious from this trajectory-with-phase picture is the fact that these fluctuations exhibit universal statistical properties. For instance, measured in conductance their magnitude is always of order  $e^2/h$ , independent of material and the average conductance, giving them their name: “universal conductance fluctuations” (UCF) [164-167]. A vast theoretical effort over the past decade has shown that the universal aspects of mesoscopic phenomena are associated with universal spectral properties of random matrices [168-172] as well as the universal properties of the quantum manifestations of classical chaos [173-175].

UCF in disordered metals and semiconductors has been widely investigated over the last fifteen years (for reviews of the experimental literature, see [163,35]). More recently, experiments in high-mobility GaAs quantum dots have shown that gate-confined *ballistic* structures (i.e. devices in which the bulk elastic mean free path  $\ell$  exceeds the size of the dot) also exhibit UCF. This ballistic UCF is similar to UCF in disordered systems [163,176-178] with the same universal statistics [170,172] as long as several conducting channels per lead are open, so that  $G_{dot} > e^2/h$ . The applicability of UCF concepts to ballistic quantum dots draws particular attention to the fact that *disorder is not a requirement for UCF*, but is only one means of generating the universal features of quantum transport. The universality of UCF applies whenever, but only when, the quantum dot has an irregular shape that gives rise to chaotic scattering from the walls of the device. Fortunately, this chaotic-shape condition is easily met in practice; with sufficiently large number of electrons ( $N > \sim 50$ ) nearly any irregular shape will yield chaos at sufficiently low magnetic field. The non-chaotic character of the vertical dots discussed in section 5.2 is possible since they contain a small number of electrons. (Here, we sidestep the fact that in classical dynamics the generic situation is a mixed phase space, with some trajectories executing regular motion and others chaotic motion. A mixed phase space can lead to fractal conductance fluctuations [180]).

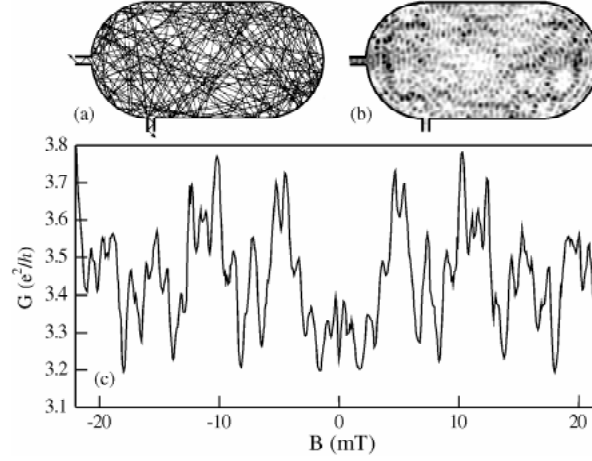


Figure 6.1. (a) Chaotic classical trajectory entering, then bouncing within, and finally exiting an open stadium billiard. The semiclassical model of transport accounts for all such classical trajectories and includes phase interference between trajectories. Signatures of *classical* chaos therefore appear in the quantum transport. (b) A quantum wave function for the open stadium billiard (the size compared to  $\lambda_F$  corresponding to the stadium device in Ref. [176], suggests an alternative approach more applicable to nearly-isolated devices, in which transport is described by the coupling of the dot wave function to the electron states in the leads. (From Akis and Ferry [181].) (c) An example of experimental conductance fluctuations in an open ( $N \sim 3$ ) quantum dot from the device used in Ref. 179.

Much of the recent progress in understanding UCF and other mesoscopic effects such as weak localization in quantum dots has been gained through the application of random matrix theory (RMT) [182]. (A powerful alternative approach based on supersymmetry has also provided many breakthrough results [183].) To treat the case of an open quantum dot with two leads, each transmitting  $M$  channels per lead, one introduces a scattering matrix of the form:

$$S = \begin{pmatrix} r & t' \\ t & r' \end{pmatrix} \quad (6.1)$$

where  $r, t$  and  $r', t'$  are  $M \times M$  complex reflection and transmission matrices for particles approaching the dot from the right or left, respectively. In order to apply RMT, the matrix  $S$  is assumed to be as random as possible given the physical constraints of the system, which are that  $S$  be unitary,  $SS^\dagger = I$ , in order to conserve current (all particles must be either transmitted or reflected), and  $S$  is symmetric ( $S = S^T$ ) for the case of time-reversal symmetry ( $B \sim 0$ ), or

Hermitian ( $S = S^\dagger$ ) for broken time-reversal symmetry ( $|B| > \sim \Phi_0/L^2$ ). We will not discuss the case of strong spin-orbit scattering, which introduces additional structure to  $S$  [182]. The conductance  $G$  of the dot can be related to  $S$  through the Landauer formula:

$$G = (2e^2/h) \text{Tr} \{ t t^\dagger \} \quad (6.2)$$

Through Eq. (6.2), the statistics of conductance fluctuations may be related to the spectral statistics of the random scattering matrix if we assume that changes to the impurity configuration or external parameters applied to the dot are equivalent to choosing another member of the random matrix ensemble. From this point of view, generic statistical properties of random matrices [184], in particular, level repulsion and spectral rigidity, can be seen to be intimately connected to the universal statistics observed in transport through disordered or chaotic dots [167,169,171,185]. (For a collection of articles on this subject, see Ref. [162]). The harder question, of course, is why the random matrix assumption should work at all in describing even single-particle transport, let alone transport in a strongly interacting electron liquid? Without attempting an answer, we simply note that while the rough connections between UCF and RMT, and between RMT and quantum chaos have been appreciated since the early days of mesoscopic physics, a rigorous theoretical web tying these subjects together has emerged only in the past year or so. The reader is referred to Refs. [183,186,187] for discussions of this fascinating subject. From an experimental viewpoint, it seems miraculous that such an abstract approach succeeds in quantitatively describing quantum transport in real materials.

## 6.2. FLUCTUATIONS OF COULOMB BLOCKADE PEAK HEIGHTS.

The random scattering matrix approach described above applies to conductance fluctuations in open quantum dots. When the leads form tunnel barriers with low conductance,  $G_{left}, G_{right} < e^2/h$ , Coulomb blockade appears at moderately low temperatures,  $k_B T < \sim E_c$ . For lower temperatures,  $k_B T < \Delta E$ , discrete 0D-states are resolved and conduction is mediated in this case by resonant tunneling through the quasi-bound state of the dot, which is lifetime-broadened by  $\hbar\Gamma$ . In this regime, conductance fluctuations as large as the average conductance itself will result as the electron states in the leads couple better or worse to the quasi-bound state of the dot, as shown in the numerical results of Fig. 6.2. For disordered or chaotic-shaped quantum dots, conductance fluctuations in the resonant tunneling regime appear random, as seen in Fig. 6.2

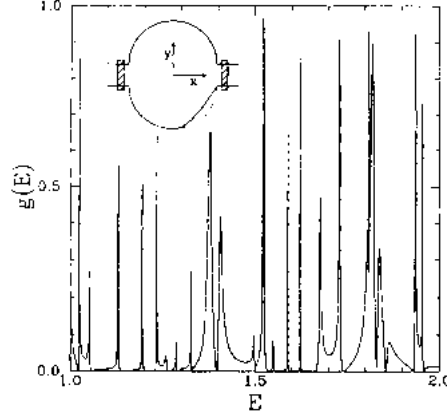


Figure 6.2. Numerical calculation of resonance conductance  $g(E)$  for a disordered and desymmetrized stadium billiard with single-mode tunneling leads, as a function of Fermi energy,  $E = E_F$ . Resonances are fits to Lorentzian lineshapes, and have large amplitude fluctuations due to the coupling of the wave function to the leads. (From Jalabert, Stone, and Alhassid [188].)

but with different statistical properties than UCF in open dots. In this case, the origin of the random fluctuations can be understood as resulting from the spatial structure of the quasi-bound wave function. In particular, the amplitude of the wave function in the vicinity of the leads determines the fluctuations, rather than the spectral properties of the scattering matrix. These differing views of the origin of mesoscopic fluctuations can be reconciled by the so-called R-matrix formalism, originally developed to address similar problems in compound nuclear scattering. R-matrix theory relates the Hamiltonian of the isolated system to the scattering matrix of the corresponding open system.

The effects of finite temperature and charging energy can be readily accounted for in the quantum Coulomb blockade regime,  $\hbar\Gamma < k_B T < \Delta E \ll e^2/C$ . Recalling the discussion in section 2, Coulomb blockade conductance peaks in this regime are approximately uniformly spaced in gate voltage  $V_g$ , and have a thermally broadened line shape,

$$G / G_{max} = \cosh^{-2}(\delta / 2k_B T) \quad (6.3)$$

where  $\delta = e(C_g/C) \cdot |V_{g,res} - V_g|$ . The peak height  $G_{max}$  is related to the tunneling rates through the left and right leads,  $\Gamma_{left}$  and  $\Gamma_{right}$ , by:

$$G_{max} = \frac{e^2}{4k_B T} \left( \frac{\Gamma_{left} \Gamma_{right}}{\Gamma_{left} + \Gamma_{right}} \right) \equiv \frac{e^2 \bar{\Gamma}}{4k_B T} \alpha \quad (6.4)$$

where

$$\alpha \equiv \frac{\Gamma_{left} \Gamma_{right}}{\bar{\Gamma}(\Gamma_{left} + \Gamma_{right})} \quad (6.5)$$

is a dimensionless peak height and  $h\Gamma = h\Gamma_{left} + h\Gamma_{right}$  is the total lifetime broadening of the 0D-state.

An RMT approach to fluctuations in peak height was developed by Jalabert, Stone and Alhassid [188] based on the assumption that the 0D-states of the dot can be described as typical large-quantum-number eigenstates ( $\psi_n$  with  $n \gg 1$ ) of a quantum chaotic system, and thus can be characterized by an RMT which is appropriate to the symmetry of the system. In this case, it is the Hamiltonian of the isolated dot rather than the scattering matrix that is modeled as a random matrix. The required symmetry of the random matrix ensemble is again confined to two classes (in the absence of strong spin-orbit scattering): symmetric matrices for  $B = 0$ , when the system obeys time-reversal symmetry (the ensemble of such random matrices is known as the Gaussian orthogonal ensemble, or GOE, because of the invariance of the spectrum under orthogonal transformation) or Hermitian matrices for  $B \neq 0$  (Gaussian unitary ensemble, or GUE).

The resulting model of transport in the quantum Coulomb blockade regime closely resembles the statistical theory of compound nuclear scattering, with peak height distributions analogous to Porter-Thomas distributions of resonance widths. The assumption that the overlap integrals of the wave functions in the dot with the wave functions in the lead are Gaussian distributed implies that the tunneling rates into and out of the dot  $\Gamma_{left}$  and  $\Gamma_{right}$  (which are proportional to the square of the overlap) obey Porter-Thomas statistics, that is  $\chi_\nu^2$  distributed with  $\nu = 1$  degree of freedom for GOE and  $\nu = 2$  for GUE. If one further assumes that the leads are statistically independent (valid when their separation greatly exceeds  $\lambda_F$ ) and have the same average tunneling rates,  $\bar{\Gamma}_{left} = \bar{\Gamma}_{right} = \bar{\Gamma} / 2$ , the distribution of dimensionless peak heights  $P(\alpha)$  have the following forms, depending only on the presence or absence of time-reversal symmetry:

$$P_{(B=0)}(\alpha) = \sqrt{2/\pi\alpha} e^{-2\alpha} \quad (6.6a)$$

$$P_{(B \neq 0)}(\alpha) = 4\alpha [K_0(2\alpha) + K_1(2\alpha)] e^{-2\alpha} \quad (6.6b)$$

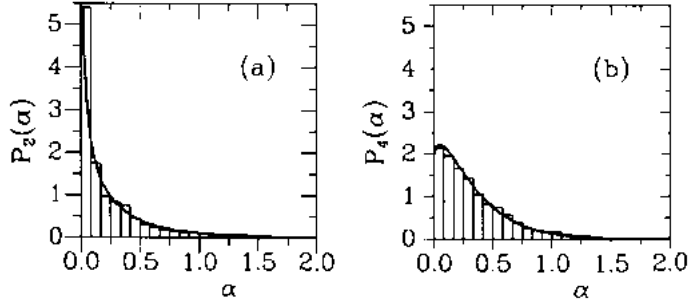


Figure 6.3. Numerical distributions of the dimensionless conductance  $\alpha$  defined in Eq. (6.5), based on resonance data similar to that in Fig. 6.2, though for a different billiard shape (the Robnik billiard), along with RMT results. (a) For the case of time-reversal symmetry, with zero magnetic flux; solid curve is the GOE result, Eq. (6.6a). (b) For the case of broken time-reversal symmetry, with an applied magnetic flux; solid curve is GUE result Eq. (6.6b). (From Bruus and Stone [192].)

where  $K_o$  and  $K_l$  are modified Bessel functions [188,189]. Note that the average peak height in zero and nonzero field are different,  $\int \alpha P_{(B=0)}(\alpha) d\alpha = 1/4$  and  $\int \alpha P_{(B \neq 0)}(\alpha) d\alpha = 1/3$ . This effect is related to weak localization in open mesoscopic systems. The above results have been extended using both RMT and nonlinear sigma-model approaches to include nonequivalent, multi-mode, and correlated leads [189-191], dot shapes undergoing distortion across the transition from integrable to chaotic classical dynamics [192], and partially broken time-reversal symmetry [193,194]. In each case the results were found to agree well with direct numerical simulations of tunneling through chaotic dots. These numerical studies of peak height fluctuations are based on a non-interacting picture of electronic wave functions in confined hard-wall 2D chaotic cavities with tunnel-barrier leads. An example comparing numerics to RMT, Eq. (6.6), is shown in Fig. 6.3 [192].

We now discuss the experiments. Earlier measurements of transport through blockaded, gate-confined quantum dots demonstrated significant height fluctuations among Coulomb blockade peaks at low temperatures and low magnetic fields [80,82,195], as seen for instance in Fig. 3.3. These fluctuations were not the main focus of these works and were not studied in detail. Recently, two groups have directly checked the RMT predictions, Eq. (6.6), using gate-defined GaAs quantum dots [196,197]. Representative series of peaks showing large height fluctuations as a function of gate voltage are shown for the data of Chang *et al.* [196] in Fig. 6.4(a) and Folk *et al.* [197] in Fig. 6.4(b). Both experiments found excellent agreement with the RMT predictions, as shown in Fig. 6.5. The consistency with theory in the two

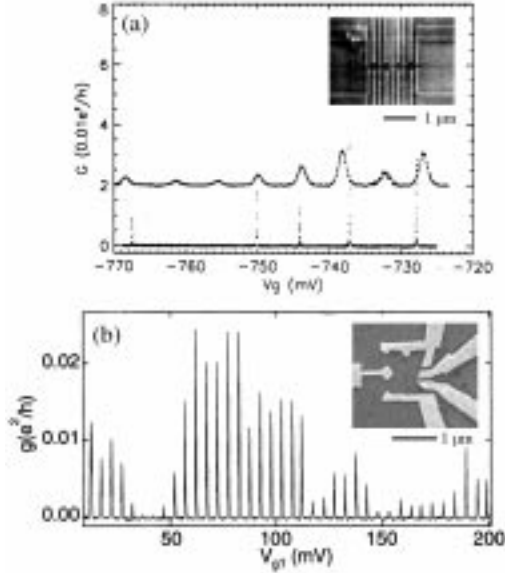


Figure 6.4. Coulomb blockade peaks as function of gate voltage, showing fluctuations in peak height, including some peaks of zero height. (a) From the experiment of Chang *et al.* [196] for very small quantum dots,  $N \sim 50-100$ . Both low temperature ( $T_{dot} \sim 75$  mK) and higher-temperature ( $T_{dot} \sim 600$  mK) data are shown. Inset shows micrograph of multiple devices used to gather ensemble statistics. (b) From the experiments of Folk *et al.* [197] for larger dots,  $N \sim 1000$  which use two shape distorting gates to create an effective ensemble of dots (inset). Data for base temperature  $T_{dot} \sim 90$  mK is shown. Both data sets (a) and (b) are for  $B = 0$ .

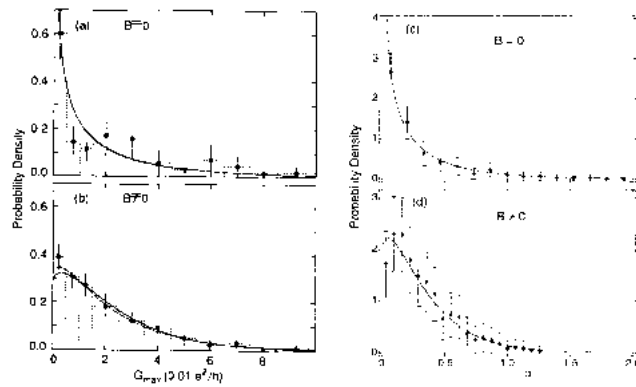


Figure 6.5. Experimental distributions of Coulomb blockade peak heights. (a,b) From Chang *et al.* [196] and (c,d) from Folk *et al.* [197]. Distributions for  $B = 0$  (a,c) and  $B \neq 0$  (b,c) in units of  $G_{max}$  for (a,b) and dimensionless conductance  $\alpha$  for (c,d), with units related by Eq. (6.4). Both experiments find reasonably good agreement with RMT, Eq. (6.6), shown as solid lines (An alternative fitting procedure, allowing variation in lead conductance, is shown as a dashed line in (a,b)).

experiments is noteworthy considering the differences in device design. The dots in Ref. 196 were relatively small, containing only  $\sim 50$ -100 electrons, and easily satisfied the requirement of the theory that  $k_B T \ll \Delta E$ , with  $\Delta E \sim 620$  mK compared to an estimated electron temperature of  $\sim 75$  mK. The dots used in Ref. 197 were considerably larger, containing of order 1000 electrons. This allowed a greater number of peaks to be observed in a single dot, but had the disadvantage that the inequality  $k_B T < \Delta E$  was only satisfied by a factor of 2, with  $\Delta E \sim 200$  mK, and an electron temperature of  $\sim 90$  mK.

An interesting feature of the data in Fig. 6.4(b) is the correlation in height between neighboring peaks, with a correlation length of  $\sim 4$  peaks for these dots. Within a single-particle picture, one would expect the spatial pattern of adjacent wave functions (associated with the  $N^{\text{th}}$  and  $(N+1)^{\text{st}}$  states of the dot) to be essentially uncorrelated [198]. The nature of this correlation, and whether it can be wholly attributed to finite temperature effects or whether it is an intrinsic feature remains unanswered and is a subject of current investigation.

### 6.3. PARAMETRIC CORRELATION OF COULOMB PEAK HEIGHT.

Besides investigating the height distribution of a set of Coulomb peaks by sweeping  $V_g$ , one may also investigate mesoscopic peak height fluctuations as a continuous function of an external parameter such as magnetic field [196,197,199]. This procedure gives a peak height function  $G_{\text{max}}(B)$  which in many respects resembles traditional UCF measurements of conductance  $G(B)$  in open systems but with different statistics. Peak height fluctuations are also closely related to universal correlations of the level velocities, i.e. the rates of change of energy of a single-particle level [200,201] with respect to a parametric change in boundary conditions. Experimentally, the measurement of  $G_{\text{max}}(B)$  is complicated by the fact that the peak position also depends on magnetic field, as seen for instance in Fig. 5.3 and Fig. 7.3. In practice, one needs a two-dimensional raster over both  $V_g$  and  $B$ , with peak height information extracted by following a peak in the  $V_g$ - $B$  plane. An example of random fluctuations in  $G_{\text{max}}(B)$  measured using this raster method is shown in Fig. 6.6(a) for the dot in Fig. 6.4(b).

Sensitivity of the Coulomb peak height to changes in magnetic field can be characterized by an autocorrelation function

$$C_g(\Delta B) = \left\langle \tilde{G}_{\text{max}}(B) \tilde{G}_{\text{max}}(B + \Delta B) \right\rangle_B / \text{var}(\tilde{G}_{\text{max}})_B \quad (6.7)$$

where  $\tilde{G}_{\text{max}} = (G_{\text{max}} - \langle G_{\text{max}} \rangle)$  is the deviation of peak height from its average. For disordered or chaotic dots,  $C_g(\Delta B)$  has been calculated within RMT by

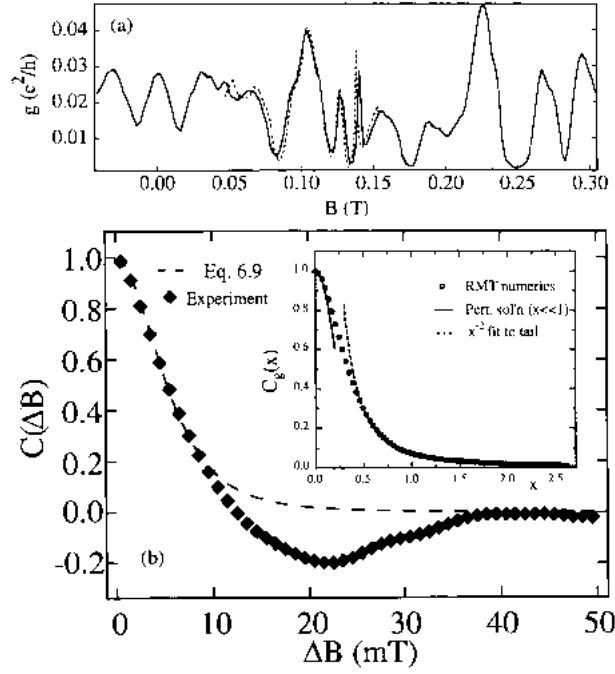


Figure 6.6. (a) Parametric fluctuations in peak height,  $G_{max}$  as a continuous function of magnetic field  $B$  measured from a 2D raster over gate voltage and  $B$ , as described in text. Dashed curve is peak height at  $-B$  showing symmetry and repeatability. (b) Experimental auto-correlation of peak height fluctuations, defined in Eq. (6.7) (diamonds). Approximate theoretical form for peak-height auto-correlation, Eq. (6.9) suggested in Ref. [46] (dashed line) gives  $B_c \sim 16$  mT. Inset: Full theoretical (RMT) distribution (open circles) along with perturbative solution  $C_g(x) \sim 1 - \pi^2 x^{-2}$  (solid curve) and large- $x$  asymptotic form,  $C_g(x) \sim 0.735(\pi x)^{-2}$  (dashed curve), where  $x = \Delta B/B_c$ . (From Folk *et al.* [41].)

Alhassid and Attias [202] and Bruus, *et al.* [203] and found to be universal when plotted as a function of the scaled variable  $x \equiv \Delta B/B_c$ . The characteristic magnetic field  $B_c$  is smaller than the field corresponding to one flux quantum through the dot:

$$B_c \sim \frac{\Phi_0}{A_{dot}} (\Delta E/\kappa E_T)^{1/2} \sim \frac{\Phi_0}{A_{dot}} (2\pi\kappa^2 N)^{-1/4} \quad (6.8)$$

where  $E_T$  is the Thouless energy, defined for ballistic dots as the inverse time of flight across the dot,  $E_T = \hbar v_F/\sqrt{A_{dot}}$ ,  $N$  is the number of electrons on the dot,

and  $\kappa$  is a geometrical factor ( $\kappa \sim 1$ ) [168,192,203,204]. Measurements of  $B_c$  based on fits of the experimental  $C_g(\Delta B)$  to the scaled theoretical curve for gate-confined dots have found values considerably larger than this prediction [197,199], close to, or even exceeding  $\phi_0/A_{dot}$ . Without a direct measurement of  $\kappa$  these results cannot be said to be inconsistent with theory. Parametric correlations of density-of-states fluctuations have been measured in vertical transport by Sivan *et al.* [205]. In their system the characteristic magnetic field was quite close to the value expected from theory. Their system differed from the present one in several ways: transport was vertical rather than lateral (and therefore only sensitive to fluctuations in density of states, not the coupling to the leads), the dot was 3D rather than 2D, and disordered rather than ballistic. The importance of these experimental differences remains to be sorted out.

The theoretical auto-correlation function of peak height fluctuations in the quantum Coulomb blockade regime,  $h\Gamma < k_B T < \Delta E \ll e^2/C$ , is shown as open circles in the inset of Fig. 6.6(b) for the case of broken time-reversal symmetry and statistically equivalent single-channel leads. This curve is found numerically using R-matrix theory assuming a Hamiltonian for the dot of the form  $H(x) = H_1 \cos(x) + H_2 \sin(x)$  with  $H_1$  and  $H_2$  independent random matrices of the appropriate symmetry, i.e. GOE or GUE [202,203,206]. Near  $x = 0$ , perturbation theory gives  $C_g(x) \sim 1 - \pi^2 x^2$ , while the  $x \gg 1$  tail is found numerically to be  $C_g(x) \sim 0.735(\pi x)^{-2}$ . To facilitate comparison to experiment, Alhassid and Attias [202] find numerically that the whole auto-correlation function is reasonably well estimated by a Lorentzian squared,

$$C_g(x) \sim \left[1 + (x/0.54)^2\right]^{-2} \quad (6.9)$$

for statistically equivalent leads and broken time reversal symmetry.

Experimental results for the auto-correlation of peak height fluctuations from Ref. 197 are shown in Fig. 6.6(b) along with a fit to the form of Eq. (6.9). The theory misses the dip below the  $C_g(\Delta B) = 0$  axis usually seen in the experimental data. This dip presumably result from some short-trajectory effect and so would not be expected to show up in RMT, though perhaps would appear in new approaches that go beyond RMT by considering the specific phase-space dynamics for a particular ballistic billiard [187]. An outstanding problem is the role of finite temperature on both the distribution functions and the correlation functions. In open quantum dots, finite temperature effects on mesoscopic fluctuations were analyzed by Efetov [207]. No similar analysis for Coulomb blockade peak height fluctuations has been given to date.

#### 6.4. MESOSCOPIC FLUCTUATIONS IN PEAK POSITION AND SPACING

While peak heights in the quantum Coulomb blockade regime show large fluctuation as a function of peak number or magnetic field (i.e. fluctuations on the order of the height itself), the spacing between peaks  $\Delta V_g$  generally appears quite uniform once the dot contains many electrons,  $N \gg 1$ , as seen in Fig. 3.3 and 6.4(b). In very small dots,  $N < 20$ , nonuniform spacing reveals shell structure as the first few quantum states are filled, as discussed in section 5. At high  $B$ , in the quantum Hall regime, regular peak position oscillations as a function of magnetic field have been observed by McEuen and coworkers [43,152,208], as discussed in section 7. An important conclusion of McEuen's high-field experiments is that in order to adequately explain the data, a self-consistent model of the confined electrons in a field is needed. Whether this continues to hold in the low field regime, where 0D quantization rather than Landau level quantization modifies the classical electrostatics problem, is not known. To start off, however, we will discuss the simplest model of random fluctuations in peak spacing as a function of the number of electrons on the dot (as set by a gate voltage). This model assumes a constant classical charging energy  $e^2/C$  which can be separated out from the level spacing  $\Delta E$  between non-interacting 0D states. In this picture, fluctuations in peak spacing are purely associated with fluctuations in spacing between the 0D-states (see also Eq. (2.3) and below):

$$\Delta V_g^N = e/C_g \quad (N \text{ odd}) \quad (6.10a)$$

$$\Delta V_g^N = \frac{C}{e C_g} (e^2/C + \Delta E) \quad (N \text{ even}) \quad (6.10b)$$

As discussed by Sivan *et al.* [209], if one further assumes  $\Delta E$  to be distributed according to RMT statistics (assuming the dot is disordered or chaotic) the resulting fluctuations in spacing  $\Delta \mathcal{E} = \Delta E / \langle \Delta E \rangle$  should then be distributed according to the famous "Wigner surmise" [210] for the distribution of eigenvalue spacings in random matrices,

$$P(\Delta \mathcal{E}) = \frac{\pi}{2} (\Delta \mathcal{E}) \exp\left(-\frac{\pi}{4} (\Delta \mathcal{E})^2\right) \quad (B = 0; \text{GOE}) \quad (6.11a)$$

$$P(\Delta \mathcal{E}) = \frac{32}{\pi^2} (\Delta \mathcal{E})^2 \exp\left(-\frac{4}{\pi} (\Delta \mathcal{E})^2\right) \quad (B \neq 0; \text{GUE}) \quad (6.11b)$$

This “constant interaction plus random matrix theory” (CI+RMT) model yields an alternating average peak spacing given by the averages of Eq. (6.10) with rms fluctuations in the spacing of peaks that bracket an even- $N$  state given by:

$$\delta(\Delta V_g) = \frac{C \Delta E}{e C_g} (4/\pi - 1)^{1/2} \cong 0.52 \frac{C \Delta E}{e C_g} \quad (B = 0; \text{GOE}) \quad (6.12 \text{ a})$$

$$\delta(\Delta V_g) = \frac{C \Delta E}{e C_g} (3\pi/8 - 1)^{1/2} \cong 0.42 \frac{C \Delta E}{e C_g} \quad (B \neq 0; \text{GOE}) \quad (6.12 \text{ b})$$

independent of  $N$ , as long as  $k_B T < \Delta E$ . Since the level spacing is typically much smaller than the charging energy, Eq. (6.12) implies relatively small fluctuations in peak spacing, consistent with experiment. A more detailed comparison, however, reveals both quantitative and qualitative disagreement between CI+RMT and experiment. At zero or small magnetic field, no even/odd behavior has been reported in dots with  $N \gg 1$  (although well-understood spin effects are seen in tunneling and capacitance spectroscopy for small  $N$  as discussed in section 5). In fact, Sivan *et al.* [209] find that fluctuation statistics in peak spacing in small gate-defined GaAs quantum dots at low temperature ( $\sim 100$  mK) disagree significantly from the CI+RMT prediction. They find peak spacing fluctuations larger by a factor of up to five from the predictions of the CI+RMT model, with an insensitivity to factor-of-two changes in  $\Delta E$  as  $N$  ranges from  $\sim 60$  to  $\sim 120$  as seen in Fig. 6.7. Moreover, the observed distribution of fluctuations does not appear similar in form to Eq. (6.11), but is symmetric about its average. These observations have lead Sivan *et al.* to suggest a picture of peak spacing fluctuations that is essentially classical in origin, closely related to the problem of packing charges onto a finite volume, with spacing fluctuations resulting from random “magic numbers” in which better and worse packings of charge depend on  $N$ . Their picture is supported by a numerical calculation of the ground state energy of a lattice model of the dot which shows that as interactions are turned on, fluctuations in ground state energy transform from the Wigner statistics of Eq. (6.11) to roughly gaussian fluctuations with an rms amplitude of  $\sim 0.10 - 0.15 e^2/C$ , independent of  $\Delta E$ .

A recent self-consistent calculation of ground state energy fluctuations in 2D and 3D quantum dots beyond the CI+RMT picture predicts fluctuations in peak spacing due to capacitance fluctuations (i.e. in addition to single-particle effects) that *does* depend on  $\Delta E$ :

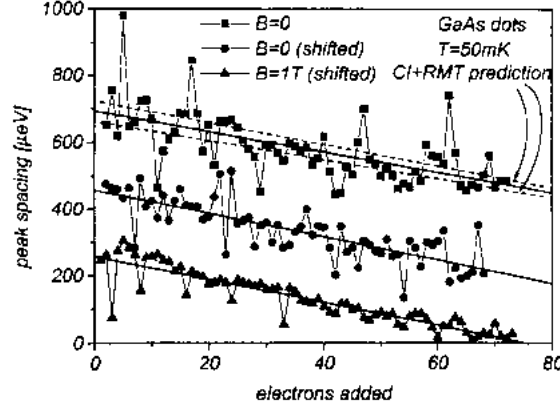


Figure 6.7. Spacing between neighboring Coulomb blockade peaks (solid squares, in energy units, including capacitance lever arm) versus number of electrons added to a GaAs quantum dot. Bottom two traces have been shifted by 200  $\mu\text{V}$  and 400  $\mu\text{V}$ , respectively. Overall slope results from gradual increase in capacitance as  $N$  increases, solid line is a linear fit. CI+RMT prediction (dashed lines) is based on Eq. (6.12). (From Sivan *et al.* [209].)

$$\delta(\Delta V_g) \sim \begin{cases} \frac{C \Delta E}{e C_g} \alpha_2 (2\pi N)^{-1/4} & (2D) \\ \frac{\sqrt{4/3} C \Delta E}{e C_g} \alpha_3 (2\pi N)^{-1/4} & (3D) \end{cases} \quad (6.13)$$

for weakly disordered dots [211]. (Eq. (6.13) applies in the case of quasi-ballistic motion of electrons; if the dot is strongly diffusive,  $\ell \ll L$ , the term  $(2\pi N)^{-1/4}$  should be replaced with  $g^{-1/2}$ , where  $g$  is the dimensionless conductance of the material.) The parameter  $\alpha_{2(3)} \approx 1$  for weak interactions, for which the screening length is much less than the Fermi wavelength, and is of order the gas parameter,  $\alpha_{2(3)} \sim e^2/\epsilon v_F$ , for strong interactions. For GaAs quantum dots, one expects  $\alpha_{2(3)} \approx 1$ . The analysis in Ref. [211] suggests that additional contributions to the fluctuations unaccounted for in the CI+RMT come from unscreened charge at the edge of the dot (roughly analogous to the packing picture). On the other hand, Eq. (6.13) suggests fluctuations in peak spacing should be of order  $\Delta E$  for weak interactions. If the value of  $\alpha_{2(3)}$  were to become  $\gg 1$ , the fluctuations would indeed be large according to Eq. (6.13), but why this should occur in GaAs gate-defined dots is not apparent. Clearly more experiments are needed to sort out this interesting problem.

A related issue concerns the parametric motion of a single Coulomb blockade peak in a magnetic field. Such motion is discussed in section 5 for few-electron dots, and in section 7 for dots in the quantum Hall regime. Parametric fluctuations of peak position at low field in larger gate confined dots [197,199] have an rms amplitude  $\delta [\Delta V_g(B)] \approx (e/C_g)[\Delta E/(e^2/C)]$ , corresponding to energy fluctuations of order  $\Delta E$ . Since peak spacing distributions over an ensemble of peaks are similar to, but certainly not the same as parametric fluctuations of a single peak, it may not be appropriate to compare this result directly to the experimental and theoretical work on peak spacing statistics gathered over many peaks.

### 6.5. PARAMETRIC PEAK MOTION AND ORBITAL MAGNETISM.

The fluctuations of Coulomb blockade peak *position*, as distinct from peak height, as a function of  $B$  is closely related to the universal parametric motion of quantum levels [186,200,201] as well as to the magnetic properties of mesoscopic samples. Connections between the statistics of peak position and peak height fluctuations have been addressed within RMT by Alhassid and Attias [202]. Peak position fluctuations are particularly important because they can be related to mesoscopic fluctuations of orbital magnetism in small electronic systems, a subject of great interest in the last few years as the result of a provocative handful of technically difficult direct measurements of the magnetic response of mesoscopic structures. By definition magnetization  $M = -\partial U(N,B)/\partial H$  and magnetic susceptibility  $\chi = \partial M/\partial H$  are the first and second derivatives of the ground state energy of a system with respect to  $B$ . So, at zero temperature,  $M$  and  $\chi$  are respectively the sums of parametric level velocities and level curvatures of all states below the Fermi surface [212]. (Remember the definition  $\mu_{dot}(N) \equiv U(N) - U(N-1)$ .) Experiments measuring the magnetic moment (or, alternatively, the persistent current, expressing derivatives in terms of flux rather than field,  $I = -\partial U(N,\varphi)/\partial \varphi$  in metallic rings have found dramatically enhanced magnetic response, one to two orders of magnitude larger than expected for non-interacting electrons, both for large ensembles [213] and individual rings [214]. In contrast, the persistent currents measured in a single ballistic GaAs ring [215] was also found to be large, but in this case was consistent with theory (for reviews see [212,216]). The susceptibility of  $10^5$  ballistic 2D GaAs squares showed a dramatically enhanced paramagnetic response around zero field, roughly 100 times the Landau diamagnetic susceptibility  $\chi_o = -e^2/12\pi m^*c^2$  [217]. This effect has been interpreted as the result of threading Aharonov-Bohm flux through *nonchaotic* families of trajectories in the square billiard, emphasizing the importance of the underlying classical dynamics on mesoscopic magnetic properties [204,216,218-220].

More generally, one expects typical mesoscopic fluctuations in  $\chi$  for an isolated ballistic 2D dot to exceed the Landau susceptibility by powers of  $k_F L$  depending on whether the shape of the dot is chaotic or integrable [204,219,220]:

$$\langle \chi^2 \rangle^{1/2} \sim \begin{cases} k_F L |\chi_o| & \text{(chaotic dynamics)} \\ (k_F L)^{3/2} |\chi_o| & \text{(integrable dynamics)} \end{cases} \quad (6.14)$$

Many of the unanswered questions concerning mesoscopic magnetism can be recast in terms of the  $B$  dependence of Coulomb blockade peak position  $V_g^*$ . In particular, the derivative of the peak position with respect to magnetic field is proportional to the *difference* between the magnetizations for subsequent values of  $N$ :

$$\partial V_g^* / \partial B \sim (C/eC_g) [M_N - M_{N+1}] \quad (6.15)$$

assuming the ratio of capacitances in the prefactor is not field dependent. Theoretically, fluctuation statistics of  $\partial V_g^* / \partial B$  can be calculated by the same methods used to obtain Eq. (6.14). An important difference between Coulomb peak position and magnetization, however, concerns fluctuating particle number. Whether or not the number of particles on the dot is a fixed quantity affects orbital magnetization and susceptibility. For instance, the zero field susceptibility of a chaotic-ballistic 2D dot has zero average (over an ensemble of dots or over shape distortions of a single dot) when particle number is not fixed (grand canonical ensemble),  $\langle \chi \rangle_{GCE} = 0$ , but is paramagnetic for fixed particle number (canonical ensemble),  $\langle \chi \rangle_{CE} \sim -k_F L \chi_o$ . Transport through a Coulomb blockade peak, on the other hand, represents a hybrid ensemble in which particle number may fluctuate by  $\pm 1$  but no more on the conductance peak, and can undergo quantum fluctuations (co-tunneling) between peaks. The rules of magnetic response in this case have not been established.

## 6.6. FLUCTUATIONS IN ELASTIC CO-TUNNELING

At moderately low temperature and small voltage bias ( $k_B T, eV_{sd} < (\Delta E, e^2/C)^{1/2}$ ), the residual conductance *between* Coulomb blockade peaks is dominated by elastic co-tunneling in which an electron (or hole) virtually tunnels through an energetically forbidden charge state of the dot lying at an energy  $\delta$  above

(below) the Fermi energy in the leads, where  $\delta$  equals  $e^2/2C$  at the center of the valley between peaks and decreases to zero on the peak. As discussed by Averin and Nazarov [221], elastic co-tunneling is a coherent virtual process that occurs on a short time scale,  $\tau_{cot} \sim h/\delta$ , consistent with the time/energy uncertainty relation. Average transport properties for elastic as well as inelastic co-tunneling were given in Ref. 221 and experimental aspects in Ref. 222. Aleiner and Glazman recently extended this work to include mesoscopic fluctuations of elastic co-tunneling [223]. Unlike on-peak conduction which can be described as a one-electron resonant tunneling process, co-tunneling properties are strongly affected by electron-electron interactions in the form of the charging energy.

The co-tunneling current for weakly coupled leads is usually very small and therefore difficult to measure. However, once the tunneling point contacts are sufficiently open, say  $G_{t,r} > \sim 0.5(2e^2/h)$ , fluctuations in the valleys can be measured quite easily, allowing co-tunneling fluctuations  $G_{min}(B)$  at valley minima to be studied along with the resonant tunneling fluctuations  $G_{max}(B)$  at peak tops. Figs. 6.8(a) and (b) show co-tunneling and resonant tunneling fluctuation for an adjacent peak and valley in a  $\sim 0.3 \mu m$  GaAs quantum dot with  $E_c \approx 600 \mu eV$  and  $\Delta E \approx 20 \mu eV$  [224]. Again, because the gate voltage positions of the peaks and valleys depend on  $B$ , a 2D raster over the  $B$ - $V_g$  plane is needed to follow peaks and valleys.

The autocorrelation functions  $C(\Delta B)$  for both  $G_{max(min)}(B)$ , (defined by Eq. 6.7) shown in Fig. 6.8(c) illustrate the primary difference between resonant (peak) and co-tunneling (valley) fluctuations: the characteristic magnetic field  $B_c$  is significantly larger for the valleys than for the peaks [197]. The difference in  $B_c$  can be understood from a semiclassical point of view as follows: On resonance, the characteristic time during which an electron diffusively accumulates Aharonov-Bohm phase is the so-called Heisenberg time, or inverse level spacing,  $\tau_H \sim h/\Delta E$ , the same as for an isolated billiard. Because co-tunneling is a virtual process, the time over which phase may accumulate is much shorter,  $\tau_{cot} \sim h/\delta$ , limited by the uncertainty relation. This suggests a characteristic field in the valleys defined in analogy to Eq. (6.8):

$$B_c^{cot} \sim \frac{\Phi_o}{A_{dot}} (\delta/\kappa E_T)^{1/2} \quad (6.16)$$

giving a ratio of characteristic fields:

$$\frac{B_c^{cot}}{B_c} = \sqrt{\frac{\delta}{\Delta E}} \quad (6.17)$$

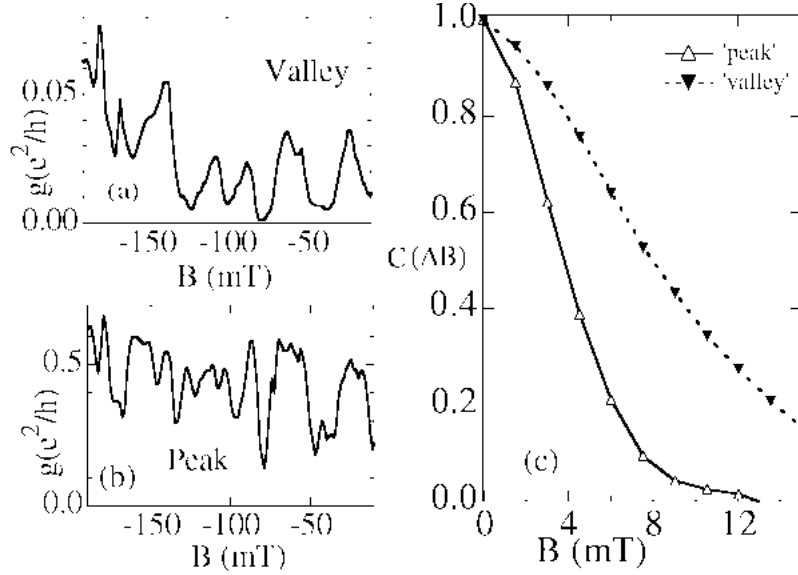


Figure 6.8. (a) Mesoscopic fluctuations of elastic co-tunneling in the valley and (b) resonant conductance on the adjacent peak for a  $\sim 0.4 \mu\text{m}$  GaAs gate-defined quantum dot. (Note the different vertical scales in (a) and (b).) (c) Normalized auto-correlation of peak and valley fluctuations, showing the factor of  $\sim 2$  larger correlation field for the valley. (From Cronenwett *et al.* [224].)

For the gate-defined GaAs dots studied in Fig. 6.8, the expected ratio of characteristic fields is  $((300 \mu\text{eV})/(20 \mu\text{eV}))^{1/2} \approx 4$ . This estimate appears inconsistent with the experimentally observed ratio of  $\sim 2$  in Fig. 6.8(c). A possible explanation for this large discrepancy is that on the peak some time scale shorter than  $\hbar/\Delta E$  is acting as the characteristic time for phase accumulation in resonant tunneling.

A proper theoretical treatment [223] of co-tunneling fluctuations accounting for virtual processes through all excited levels above the Coulomb gap reproduces the semiclassical results Eqs. (6.16) and (6.17), and for the case  $E_T < 2\pi\delta$ , predicts explicit universal forms for the autocorrelation of valley conductance (Fig. 6.9) as well as the full distribution of co-tunneling fluctuations for arbitrary magnetic field [223]. One interesting feature of the analysis is that although the full distribution is sensitive to time-reversal symmetry breaking by a small magnetic field, its first moment, the average co-tunneling conductance  $\langle g \rangle_{cot}$ , is independent of field and therefore (unlike peak conductance) does not show an analog of weak localization.

Finally we point out that the increased field scale of the valleys is a direct reflection of the “tunneling time” of an electron through the dot [225]. Mesoscopic fluctuations of co-tunneling therefore provide a novel tool for measuring full distributions of such times in a much simpler way than can be realized in time-domain tunneling experiments. Experimental work in this direction is in progress.

### 6.7. CONCLUSIONS AND OPEN PROBLEM.

The coexistence of quantum interference, quantum chaos (leading to universal statistics of wave function and scattering statistics), and electron-electron interaction makes the problem of transport through quantum dots at low temperatures both complicated and very rich, experimentally and theoretically. This is true for both open quantum dots and Coulomb blockaded dots, the subject of the present section. As in the nuclear scattering problem, the strongest justification for the use of RMT in mesoscopics has been agreement with experiment. Recent experiments described here [196,197] have highlighted an important new success: a correct description of the peak height fluctuations in the quantum regime,  $h\Gamma < k_B T < \Delta E \ll e^2/C$ . We have also seen how mesoscopic fluctuations in virtual tunneling are observed experimentally and understood qualitatively within relatively simple models. However, many phenomena remain unaddressed theoretically, for instance the effects of finite temperature, scarred wave functions, dephasing and mixed dynamics on the distribution and correlation of peak heights. Other phenomena disagree quantitatively with a “constant interaction plus single-particle quantum chaos” model. Such outstanding disagreements include correlations between the heights of neighboring Coulomb peaks, the magnetic field scale for peak height fluctuations, ratios of peak to valley correlation fields, and peak spacing distributions.

Much of the theoretical story relating mesoscopic fluctuations, quantum chaos, and random matrix theory has been worked out only in the last year or so, and is only now beginning to be tested experimentally. As the focus in mesoscopic physics continues its shift toward the influence of interactions and coupling to the environment, new difficulties and challenges will certainly continue to appear. Two directions of interest that will further expand the palette of mesoscopic phenomena in microstructures in the coming years are the inclusion of superconducting contacts and high-frequency excitation. Present successes motivate a statistical approach to these problems as well, and indeed significant theoretical inroads have been made. Here, too, experiments remain very far behind theory.

## 7. Quantum Dots in High Magnetic Fields.

In this section, we examine the addition spectra of quantum dots when large magnetic fields are applied, and compare the experimental results to theoretical predictions. In 7.1, we address few electron dots, where exact calculations can be performed. Interesting predictions, such as singlet-triplet oscillations in the spin state of the two-electron dot, are compared with experiment. In 7.2 and 7.3, we discuss many-electron dots, where the quantization of the electron orbits into Landau levels is important. 7.2 addresses results that can be understood at a Hartree level, while 7.3 looks at Hartree-Fock and beyond.

### 7.1. FEW-ELECTRON DOTS AT HIGH MAGNETIC FIELDS.

As was discussed in the previous sections, the simplest model of a quantum dot consists of non-interacting electrons residing in a parabolic confining potential. The classical motion is then a periodic oscillation with a characteristic frequency  $\omega_o$ . The addition of a magnetic field alters the motion, leading to orbits of the type shown in Fig. 7.1. An electron at the center of the dot rotates in a cyclotron-like orbit, which becomes the cyclotron frequency  $\omega_c = eB/m^*$  at high magnetic fields. Electrons away from the center slowly precess around the dot as they perform their cyclotron motion. This is due to the drift velocity  $\mathbf{v}_d = \mathbf{E} \times \mathbf{B}$  of the cyclotron orbit in the electric field of the confinement potential. Quantum mechanically, this model can be easily solved [149,150]; the result is given in Eq. (5.2). If we include spin then at high magnetic fields ( $\omega_c \gg \omega_o$ ), Eq. (5.2) simplifies to:

$$E(n, m, S_z) = (n + 1/2)\hbar\omega_c + (2n + |\ell| + 1)\hbar\omega_o^2 / \omega_c + g\mu_B B S_z \quad (7.1)$$

where  $n = 0, 1, 2, \dots$  is the radial or Landau level (LL) index,  $\ell$  labels the angular momentum of the drifting cyclotron orbit, and  $S_z = \pm 1/2$  is the spin index. Roughly speaking, the LL index  $n$  labels the number of magnetic flux quanta  $h/e$  enclosed by the electron orbit during its cyclotron motion, while  $|\ell|$  labels the number of flux quanta enclosed by the drifting orbit. Since each successive  $\ell$ -state encloses one more flux quantum, each (spin-degenerate) LL within the dot can be occupied by one electron per flux quantum penetrating the area of the dot. Increasing  $B$  causes both types of orbits to shrink in order to encircle the same number of magnetic flux quanta, making more states fit in the same area and increasing the LL degeneracy.

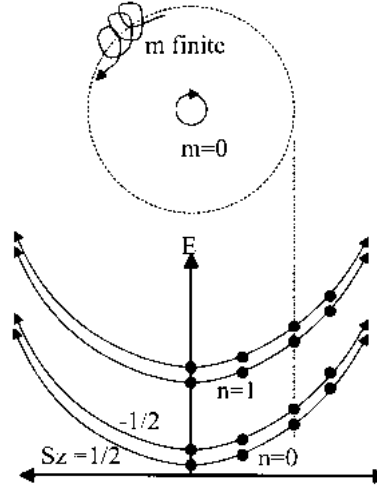


Figure 7.1. Top: Classical electron orbits inside a parabolically confined quantum dot. The orbit in the center exhibits cyclotron motion, while the orbit away from the center also drifts in the electric field of the confining potential. Bottom: Schematic energy level diagram of a quantum dot in a high magnetic field. The  $n = 0$  and  $n = 1$  orbital LLs are shown, each of which is spin-split. The dots represent quantized states within a LL that encircle  $m$  flux quanta in their drifting cyclotron motion, where  $m$  is linearly related to  $l$ , the angular momentum of the state.

Eqs. (5.2) and (7.1) ignore electron-electron interactions. Nevertheless, they should be valid for the first electron occupying a dot, since there are no other electrons with which to interact. The solution from Eq. (5.2) with  $n = \ell = 0$  should thus describe the ground-state addition energy of the first electron. At  $B = 0$  this is the zero-point energy of the harmonic oscillator,  $\hbar\omega_o/2$ . At high  $B$  it is the energy of the lowest LL  $\hbar\omega_c/2$ , and the electric to magnetic crossover occurs when  $\omega_c \approx \omega_o$ .

Measuring a one-electron dot in the lateral gated geometry has proven to be difficult. Vertical dots with as few as one electron have been studied by both linear transport measurements and nonlinear  $I$ - $V$  characteristics and by capacitance spectroscopy, as we discussed in section 5. Results from the latter technique are shown in Fig. 7.2, taken from Ashoori *et al.* [50]. The change in the capacitance due to a single electron tunneling on and off a dot is plotted in grey scale as a function of energy, which was deduced from an applied gate voltage, along the  $y$ -axis and magnetic field along the  $x$ -axis. The first line at the bottom of Fig. 7.2 represents the addition energy for the first electron as a function of  $B$ . The addition energy is constant for low  $B$  and grows linearly for high  $B$ . Fitting to Eq. (7.1) allows the determination of the bare harmonic oscillator frequency:  $\hbar\omega_o = 5.4$  meV.

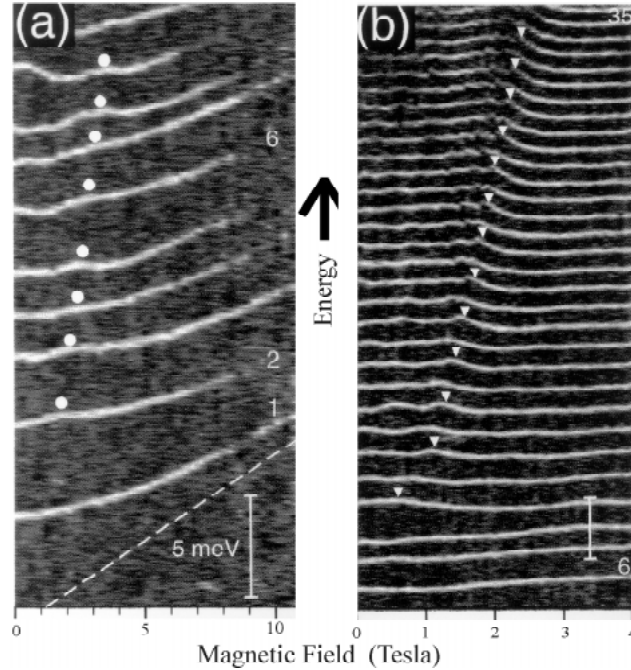


Figure 7.2. Gray scale plot of the addition energies of a quantum dot measured as a function of magnetic field. Each successive light gray line corresponds to the energy for adding an additional electron to the dot. (a) Addition spectrum for the first few electrons. The dot on the curve for the second added electron marks the singlet-triplet transition discussed in the text. (b) Addition spectrum for 6 through 35 electrons. The triangles mark the filling factor  $\nu = 2$  (From Ashoori et al. [90]).

The situation gets more interesting for more than one electron on the dot. To describe the addition energy for larger number of electrons, the simplest approach is to use the non-interacting electron spectrum, Eq. (7.1), combined with the Coulomb-blockade model for the interactions. This model is discussed in section 2. In this approximation, the second electron would also go into the  $n = \ell = 0$  state, but with the opposite spin, creating a spin singlet state. This spin singlet state remains the ground-state configuration until the Zeeman energy is large enough to make it favorable for the second electron to flip its spin and occupy the  $n = 0, \ell = 1$  state. From Eq. (7.1), this occurs when  $\hbar\omega_o/\omega_c = g\mu_B B$ . The two electron ground state is then an  $S_z = 1$  spin-triplet state. For GaAs the spin splitting is quite small ( $g = -0.4$ ), and the Zeeman-driven singlet-triplet transition would occur at a very large  $B$  of around 25 T for the dot in Fig. 5.2. The data, however, shows something quite different. The

addition energy for the second electron has a feature at a much lower field (marked by a dot) that has been attributed to the singlet-triplet transition [50].

A more realistic model of the Coulomb interactions can explain this discrepancy [77]. The size of the lowest state (i.e.  $n = 0$ ,  $\ell = 0$ ) shrinks in size with increasing  $B$ . As a result, the Coulomb interaction between the two spin-degenerate electrons grows. At some point, it becomes favorable for the second electron to occupy the  $\ell = 1$  single-particle state, avoiding the first electron and reducing the Coulomb interaction energy. Now the electrons are in different single particle states, the Pauli exclusion principle no longer requires that their spins point in opposite directions. Both the exchange interaction and the external magnetic field favor an alignment of their spins, and the two-electron system thus switches to a triplet state. This transition is driven predominantly by Coulomb interactions, since the spin splitting is still quite small.

Many other features are also observed in the addition energies of the first few electrons as a function of  $B$ , as seen in Fig. 7.2(a). These features can also be interpreted by comparison with microscopic calculations [227]. The agreement between experiment and theory is not always perfect, which indicates the need for further study.

## 7.2. MANY-ELECTRON DOTS IN THE QUANTUM HALL REGIME.

At larger number of electrons on the dot ( $N > 20$ ), the capacitance spectroscopy measurements begin to show very organized behavior, as is seen in Fig. 7.2(b). This large  $N$  regime has been extensively explored by transport spectroscopy in lateral structures [152,195,208]. An example is shown in Fig. 7.3, where the addition energy for the  $N$ th electron ( $N \sim 50$ ) is measured as a function of  $B$  [152]. This plot is made by measuring a Coulomb oscillation and plotting the position in gate voltage (a) and height (b) of the peak as a function of  $B$ . The behavior is very regular in the regime between 2 T and 4 T. The peak positions drop slowly, and then rise quickly, with a spacing between rises of approximately 60 mT. At the same time that the peak position is rising, the peak amplitude drops suddenly. Regularities can also be seen in the peak amplitudes measured at a fixed  $B$ , but with changing  $V_g$ , i.e. for adding successive electrons. For example, the data presented in Figs. 4.1 and 4.2 are plots of a series of peaks in the ordered regime above 2 Tesla [152]. A close examination reveals that the peak heights show a definite modulation with a period of every-other peak.

To understand these results, a theoretical model of the many-electron dot is needed. Unfortunately, for dots containing more than  $\sim 10$  electrons, exact calculations cannot easily be performed and approximation schemes must be

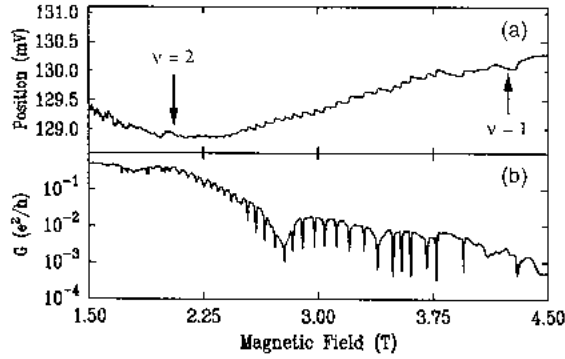


Figure 7.3. (a) Position in gate voltage and (b) peak height of a conductance peak measured as a function of magnetic field. The filling factors  $\nu$  in the dot are as marked. The quasi-periodic structure reflects single-electron charge rearrangements between the two lowest LLs. (From McEuen *et al.* [152].)

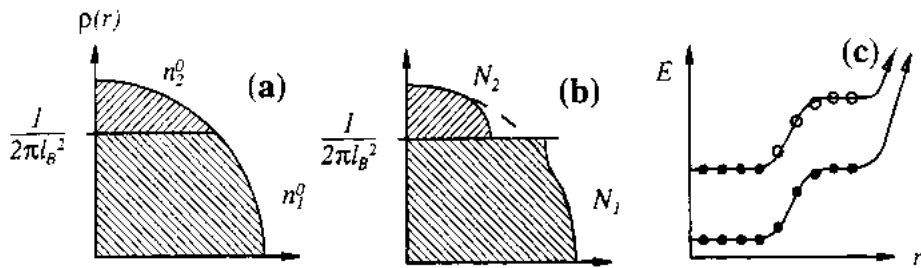


Figure 7.4. (a) Self-consistent model of a dot with two Landau levels occupied. (a) Filling of the LLs that would yield the classical electrostatic charge distribution. (b) Electrons redistribute from the higher to the lower LL to minimize their LL energy. (c) Resulting self-consistent level diagram for the dot. Solid circles: fully occupied LL, i.e. an “insulating” region. Open circles: partially occupied LL, i.e. a “metallic” region. (From McEuen *et al.* [152].)

used. Again, the simplest approach is to assume the electrons fill up the non-interacting electron states, given by Eq. (7.1), and to use the Coulomb blockade model to describe the Coulomb interactions [7,208]. This model was used to interpret early experiments [208], but later work showed it to be seriously inadequate [152], for essentially the same reasons that we discussed above for the two-electron dot. In a high magnetic field, Coulomb interactions cause rearrangements among the states that cannot be understood from the behavior of non-interacting levels.

An improved description of the addition spectrum treats the Coulomb interactions in a self-consistent manner [152,228,229]. This proto-Hartree approach is essentially the Thomas-Fermi model, but with the LL energy spectrum replacing the continuous density of states that is present at  $B = 0$ . In this model, one views the quantum dot as a small electron gas with a nonuniform electron density. Classically, this density profile would be determined by the competition between the Coulomb interactions and the confinement potential. For example, for a parabolic confinement potential, the result is an electron density that is maximal at the center and decreases continuously on moving away from the center, as shown in Fig.7.4(a).

We now include the effects of Landau level quantization in this picture. In a first approximation, the electrons fill up the requisite number of Landau levels to yield the classical electrostatic distribution. For simplicity, we concentrate exclusively on the case where only two LLs are occupied ( $n = 0$ ;  $S_z = \pm 1/2$ , i.e. the spin-resolved lowest orbital LL). This is shown in Fig. 7.4(a). Note, however, that the states in the second (upper) LL have a higher spin energy than those in the first (lower) LL. As a result, some of these electrons will move to the lower LL. This continues until the excess electrostatic energy associated with this charge redistribution cancels the gain from lowering the LL energy. The resulting (self-consistently determined) charge distribution for the island is shown in Fig. 7.4(b), and the electrochemical potentials for electrons added to the two LLs are shown in Fig. 7.4(c). Note that partial occupation of a LL implies that there are states at the Fermi energy available to screen the bare potential. If we assume perfect screening then the resulting self-consistent potential is flat. This is analogous to the fact that in the interior of a metal no electric fields are present. For example, in the center of the island, where the second LL is partially occupied the self-consistent electrostatic potential is flat. Similarly, near the edge, where the first LL is partially occupied, the potential is also flat. In between, there is an insulating region where exactly one LL is occupied.

The result is that we have two metallic regions, one for each LL, separated by an insulating strip. Electrons added to the dot are added to one of these two metallic regions. If the insulating strip is wide enough, tunneling between the two metallic regions is minimal; they will effectively act as two independent electron gases. The charge is separately quantized on each LL. Not only is the total number  $N$  of electrons in the dot an integer, but also the numbers of electrons  $N_1$  in  $LL_1$  and  $N_2$  in  $LL_2$  are integers. In effect, we have a two-dot, or “dot-in-dot” model of the system, very much similar to the parallel dot configuration in Fig. 4.1.

This schematic picture of a quantum dot in high magnetic fields is supported by a number of simulations [152,228-230]. Fig. 7.5 shows a contour

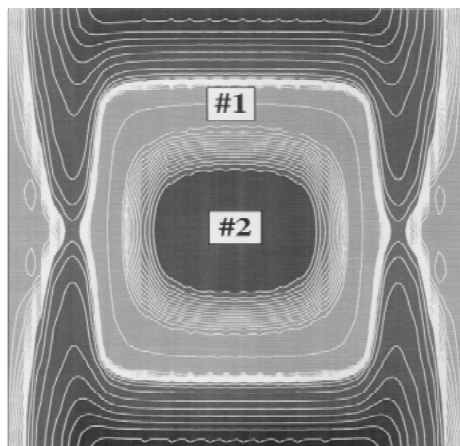


Figure 7.5. Contour plot of the self-consistent electrostatic potential for a ( $1 \mu\text{m} \times 1 \mu\text{m}$ ) quantum dot in a high magnetic field. In the regions labeled #1 and #2, the first and second LLs are partially occupied. The electrons can thus rearrange themselves to screen the external potential, and the resulting self-consistent potential is constant. In between, where one LL is fully occupied and no screening occurs, the potential rises sharply. (From Stopa [230].)

map of the electrostatic potential for a quantum dot with two occupied LLs, as calculated by Stopa [230]. In the center of the dot (region #2) where the second LL is partially occupied, the potential is flat. Similarly, the first LL creates a ring of constant potential where it is partially occupied (region #1). Electrons tunneling onto the dot will go to either one of these metallic regions.

We now discuss the implications of this model for transport measurements. First, as additional electrons are added to the dot, they try to avoid each other. As a result, successively added electrons tend to alternate between the two metallic regions. Note, however, that electrons will most likely tunnel into the outer LL ring, as it couples most effectively to the leads. Peaks corresponding to adding an electron to the inner LL should thus be smaller. If electrons are alternately added to the inner and outer LLs with increasing gate voltage, the peaks should thus alternate in height. The measurements of Fig. 3.2 show this behavior. Measurements [231] for higher numbers of LLs occupied give similar results (i.e. a periodic modulation of the peak amplitudes), with a repeat length determined (approximately) by the number of LLs occupied [83,232].

To understand the peak-position structure in Fig 7.3(a), we again note that, as  $B$  increases, the electrons orbit in tighter circles to enclose the same magnetic flux. In the absence of electron redistribution among the LLs, the charge density therefore rises in the center of the dot and decreases at the

edges. This bunching causes the electrostatic potential of the second LL to rise and that of the first LL to drop. Therefore, the energy for adding an electron to the first LL,  $\mu_1(N_1, N_2)$ , and hence the peak position, decreases with increasing  $B$ . This is illustrated schematically in Fig. 7.6. This continues until it becomes energetically favorable for an electron to move from the second to the first LL. This electron redistribution, which we call internal Coulomb charging, causes the electrostatic potential of the first LL to jump from  $\mu_1(N_1, N_2)$  to  $\mu_1(N_1+1, N_2-1)$  with  $N = N_1 + N_2$ . The energy difference  $[\mu_1(N_1, N_2) - \mu_1(N_1+1, N_2-1)]$  is equal to the interaction energy between LL<sub>1</sub> and LL<sub>2</sub> minus the single electron energy of LL<sub>1</sub>. These jumps are clearly observable in the data of Fig. 7.3, occurring every 60 mT. Note that these electron redistributions are a many-electron version of the two-electron singlet-triplet transition. In both cases, Coulomb interactions push electrons into states at larger radii with increasing  $B$ .

The peak height data shown in Fig. 7.3(b) can be similarly explained. The peak amplitude for adding the  $N$ th electron is strongly suppressed at  $B$  fields where it is energetically favorable to add the electron to the inner LL. This corresponds to the magnetic field where the peak position is rising. A dip in the peak amplitude thus occurs at every peak position where an electron is transferred from the second to the first LL. The period of the oscillation, 60 mT, roughly corresponds to the addition of one flux quantum to the area of the dot. This period implies an area of  $(0.26 \mu\text{m})^2$ , a size which is consistent with the dimensions of the dot.

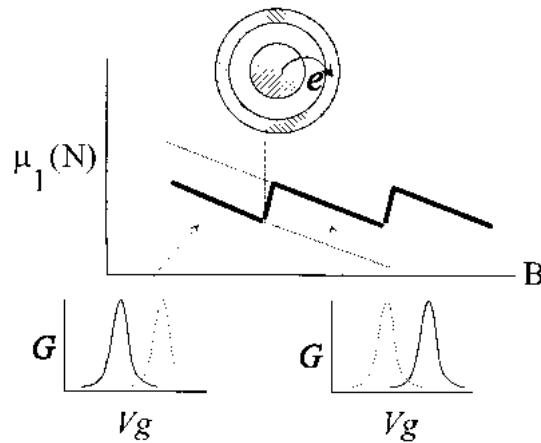


Figure 7.6. Schematic illustration of charge redistribution within a dot with increasing magnetic field. When a single electron moves from the 2nd to the 1st LL, the electrochemical potential for adding an additional electron to the 1st LL increases. As a result, the peak position shifts.

Care must be taken in interpreting the peak height, however. Other experiments show [208,231,233] that the heights of the smaller peaks do not directly reflect the tunneling rate into the inner LL. The tunneling rate into the inner LL is typically too small to produce a significant current. The observed peak is actually due to thermally-activated transport through the outer (first) LL. Since all of the observed current corresponds to tunneling through the first LL, the position of a peak is proportional to the electrochemical potential  $\mu_1(N_1, N_2)$  for adding an electron to the first LL. This potential is a function of both  $N_1$  and  $N_2$ , the number of electrons in the first and second LL, respectively.

The jumps in the peak position with increasing  $B$  thus represent a redistribution of electrons between the LLs. In experiments by van der Vaart *et al.* [233], the peaks were actually observed to jump back and forth *in time*. This is shown in Fig. 7.7. Fig. 7.7(a) shows that with two LLs occupied a peak that corresponds to  $N$  electrons in the dot can appear as a double peak. The double peak has a resonance when either  $\mu_1(N_1, N_2)$  or  $\mu_1(N_1+1, N_2-1)$  aligns with the Fermi energy of the reservoirs. Fig. 7.7(b) shows that the conductance measured as a function of time at a fixed gate voltage switches between two discrete levels. This peak-switching is due to a single electron hopping

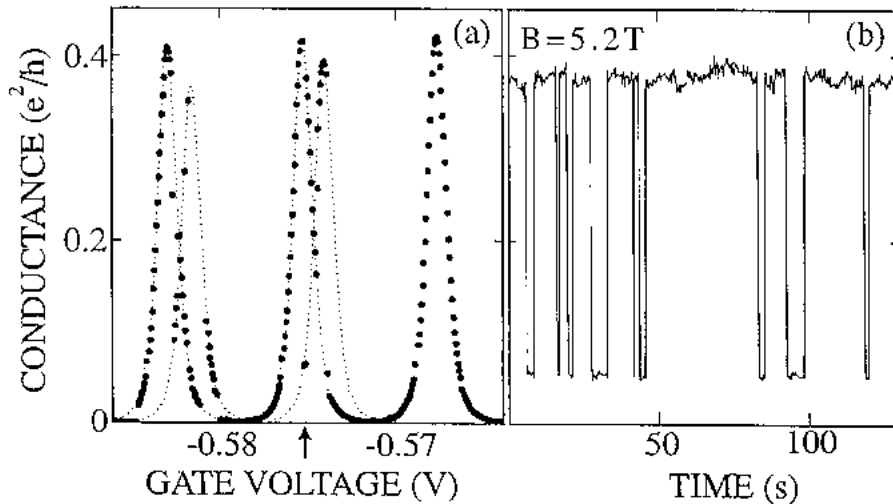


Figure 7.7. (a) Conductance through a quantum dot as a function of gate voltage, measured in a regime where 2 LLs are occupied inside the dot. The Coulomb peaks are observed to switch back and forth between two positions. (The dotted lines are a guide to the eye.) (b) Conductance versus time with the gate voltage fixed at the value denoted by the arrow in (a). The switching behavior results from the hopping of a single electron between the 1st and 2nd LL. (From van der Vaart, *et al.* [233].)

between the inner and the outer LL. At this magnetic field, the time for hopping was on the order of 10 seconds. The tunneling rate between the inner and outer dot is thus incredibly small. This corroborates the point made earlier that the coupling to the inner Landau level is very weak and all of the measurable current is carried by tunneling through the outer LL. Note that this justifies viewing two LLs in a single dot as effectively a double, parallel dot system.

### 7.3. HARTREE-FOCK AND BEYOND.

The model and experiments discussed above indicate that much of the behavior of quantum dots in magnetic fields can be understood based on LL quantization and self-consistent electrostatics. Recently, however, a number of measurements have demonstrated the importance of Coulomb interactions beyond the Thomas-Fermi approximation. For example, the Hund's rule behavior discussed in section 5 is most easily understood within the Hartree-Fock approximation. In the quantum Hall regime, the Hartree-Fock approximation [155,234] yields an effective short-range attractive interactions between electrons of the same spin that leads to larger incompressible regions than in the model above. For example, this significantly alters the rate at which electrons move from the second to the first LL with increasing  $B$  in the regime  $2 < \nu < 1$ . In particular, it is predicted that the transition from a spin-unpolarized dot at  $\nu = 2$  to a spin-polarized dot at  $\nu = 1$  can be described as a second-order phase transition between a magnetic and nonmagnetic state. The magnetization (i.e. the spin polarization of the dot) is predicted to vary as:  $M \sim (B - B_c)^{1/2}$  [235], where  $B_c$  is the magnetic field at  $\nu = 2$ . This implies a rate of change of  $M$  with  $B$ , i.e. a spin susceptibility, of the following form:

$$\chi \equiv dM/dB \sim (B - B_c)^{-1/2} \quad (7.2)$$

The diverging spin susceptibility near  $B = B_c$  indicates that the spins flip very rapidly with increasing  $B$  near the transition. This is driven by the exchange interaction making it desirable to create a region of spin polarized electron gas around the perimeter of the dot.

This prediction is borne out by experiments of Klein *et al.* [235]. Fig. 7.8 shows measurements of the addition spectrum, and Fig. 7.9 the spin susceptibility. The latter is measured by extracting the discrete derivative of  $M$  with respect to  $B$  from the data:  $dM/dB = (1 \text{ spin})/\Delta B$  between successive spin-flips). As Fig. 7.9 shows, the HF theory closely resembles the experimental data, while the self-consistent theory does not produce the diverging susceptibility seen in the experiment.

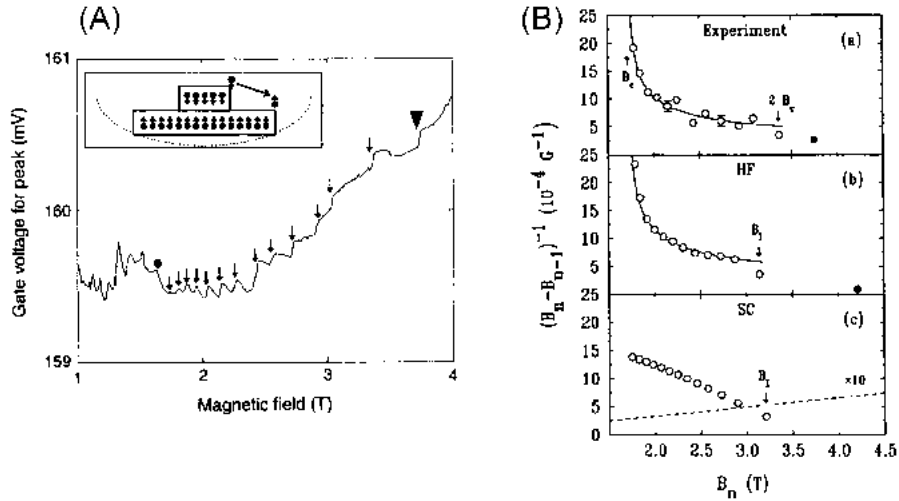


Figure 7.8. (A) Position of the  $M$ th conductance peak as a function of magnetic field. The filled black circle marks the magnetic field at which all electrons are in the lowest orbital LL. The arrows indicate spin flips of individual electrons within the dot. (From Klein *et al.* [235].) Inset: Schematic diagram of the spin-flipping process. (From Ashoori [15].) (B) Plots of the spin susceptibility of the dot versus  $B$ . (a) Experimental data from (A). (b) Predictions of Hartree-Fock model. (c) Predictions of self-consistent model. (From Klein *et al.* [235].)

At higher  $B$ , in the regime  $\nu < 1$ , Hartree-Fock models also make interesting predictions. In the self-consistent model for  $\nu < 1$ , the charge density simply retains its classical electrostatic profile, since the kinetic energy of the electrons are quenched. However, the exchange interaction and correlations beyond the exchange interaction favor different possibilities. If the electron gas is assumed to remain spin-polarized, then theory predicts an edge reconstruction with increasing  $B$  where the charge density no longer monotonically decreases with increasing radius [155,234,236,237].

More recently, people have considered the possibility of non-spin-polarized ground states, motivated by the observation of spin textures, or "skyrmions" in bulk 2DEGs at filling factors near  $\nu = 1$  [238]. In this case, the exchange interaction favors a slow variation of the spin of the 2DEG in space to accommodate an extra, or a missing, electron in a full LL. Recent work indicates that such spin textures will form at the edge of a 2DEG [239], or at the periphery of a quantum dot [240], under the right experimental conditions.

Experimentally, jumps in the addition spectra are observed for  $\nu < 1$  [50,235]; see, for example, the jump marked by a triangle in Fig. 7.8. These jumps have been interpreted as resulting from edge reconstructions [15,235]. It

is very difficult, however, to delineate between the two types of reconstructions discussed above from measurements of the addition spectrum only. Recent experiments on the excitation spectra [241] of dots give evidence that spin flip excitations are important, but the evidence is indirect. A direct measurement of the spin polarization of the dot would be very helpful, but performing such a measurement remains an unsolved experimental challenge.

Also of potential interest are many-body effects on the tunneling rates of single electrons on and off the dot. If tunneling on the dot requires a complex rearrangement of all other electrons, its rate is predicted to be dramatically suppressed [242]. This "orthogonality catastrophe" may be contributing to the extremely slow tunneling rates between the inner and outer LL regions found in the experiment of Fig. 7.7. More experiments are necessary to fully explore these possibilities.

## 8. Time-dependent transport through quantum dots.

This section presents a brief review of some of the experiments and theory on time-dependent transport in quantum dots. In practice, "time-dependent transport" means that an ac signal is applied to a single dot or a multiple dot system and the time-averaged current is measured. In this sense, the process is simply rectification, although the effects can be both non-linear in the driving signal and also non-adiabatic in the driving frequency. Indeed, the application of external frequencies comparable to internal energies of the dot (e.g. level spacings) can be thought of as a form of spectroscopy. The following topics are addressed here: (8.1) adiabatic driving of electrons "the electron turnstile", (8.2) non-adiabatic driving and the Tien-Gordon picture of time-dependent transport, (8.3) spectroscopy of a single dot, and (8.4) time-dependent transport through a double dot.

### 8.1. ADIABATIC REGIME; THE ELECTRON TURNSTILE.

Because of the Coulomb blockade the current through a quantum dot is limited to one electron at a time. This property can be exploited to create an *electron turnstile*, a device which passes one electron in every cycle of an external driving field. Such a device was first realized by Geerligs and coworkers [89] using a series of metal dots. Here, we discuss a simpler realization of the quantum-dot turnstile by Kouwenhoven *et al.* [90,243]. The device is shown schematically in Fig. 8.1. Electrons are moved one at a time through the dot by two sinusoidal signals applied to the two tunneling barriers, 180 degrees out of phase. The rf frequency of the applied signal,  $f = 10$  MHz, is much slower than

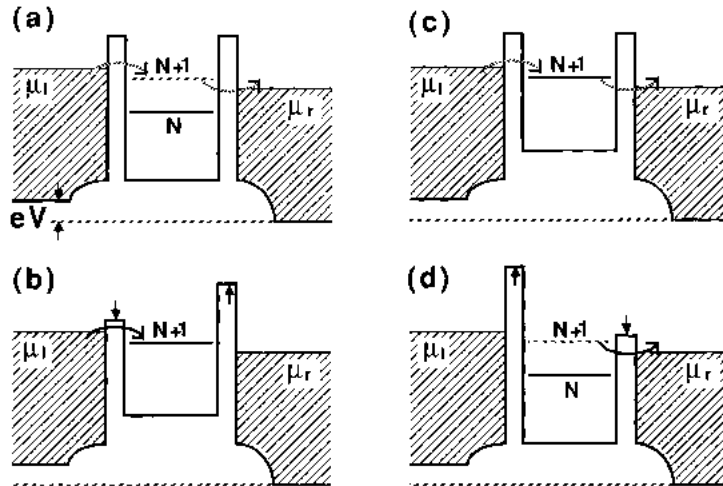


Figure 8.1. Schematic potential landscape for a quantum-dot electron turnstile. (a)-(d) are four stages of an rf cycle. The solid lines indicate the electrochemical potential  $\mu_{dot}$  for the number of electrons that are actually on the dot [i.e.  $N$  in (a) and (d) and  $N+1$  in (b) and (c)]. The dashed lines indicate  $\mu_{dot}$  for one extra electron on the dot. The probability for tunneling is large when the barrier is low (solid arrows), and small when the barrier is high (dashed arrows). During one cycle an integer number of electrons are transported across the quantum dot. (From Kouwenhoven *et al.* [90].)

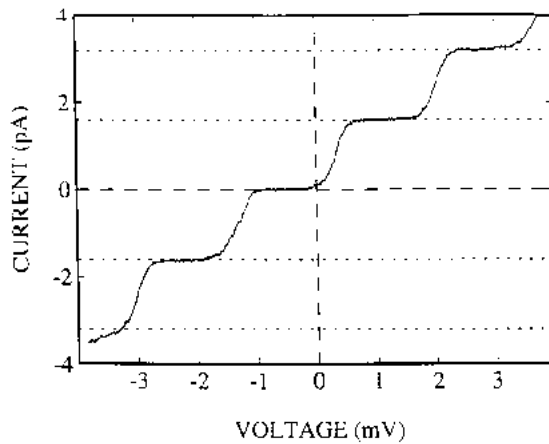


Figure 8.2. Current-voltage characteristics of a quantum-dot electron turnstile. Current plateaus occur at integer multiples of  $ef$  (dotted lines) where the driving frequency  $f = 10$  MHz. (From Nagamune *et al.* [16].)

the tunneling rate of electrons on and off the dot when the barriers are low. The driving signal is therefore in the adiabatic limit in which the state of the dot is fully determined by the electrochemical potential on the side of the low barrier. As depicted in Fig. 8.1, in one cycle exactly one electron is transferred across the quantum dot: The cycle begins with  $N$  electrons on the dot. The barrier to the left lead is then lowered allowing an additional electron to enter the dot. The barrier to the left is then raised, preventing the extra electron from escaping back to the left. The right barrier is then lowered and the electron escapes into the right lead. Raising the barrier to the right lead completes the cycle and returns the dot to its initial configuration with  $N$  electrons. By applying a larger source-drain bias to increase the number of extra electrons allowed on the dot when the left barrier is lowered, two electrons, or three electrons, and so on, can be transferred in each cycle. As a result the time-averaged current passing through the dot is just an integer times the single electron charge times the driving frequency,  $I = nef$ . This current quantization is clearly observed in Fig. 8.2. Each plateau corresponds to an integer number of electrons passing through the quantum dot in each cycle.

Recent work by Keller *et al.* [244] on electron turnstiles has focussed on the possibility of creating a current standard. A high precision experimental connection between current and frequency would complement the standards of voltage and resistance provided by the Josephson and quantum Hall effects. This in turn would provide a new measurement of the fine structure constant. Experiments on a series of four metal dots subjected to precisely phased rf signals have demonstrated a current locked to the rf frequency to an accuracy of 15 parts in  $10^9$  [244].

## 8.2. NON-ADIABATIC REGIME; TIEN-GORDON THEORY.

When the driving signal frequency exceeds the rate at which electrons tunnel on and off the dot, the state of the dot is no longer simply determined by the instantaneous values of the applied voltages [245]. In this non-adiabatic regime it is essential to take into account the phase coherence in time of the electrons on the quantum dot [246-248]. As an instructive example, consider an isolated dot containing a single non-degenerate level whose energy is oscillated up and down in time with respect to the rest of the device. According to Schrödinger's equation, the electron's wavefunction is given by:

$$\psi(x,t) = \psi(x) \exp[-i \int dt' \varepsilon(t')/\hbar] \quad (8.1)$$

where  $\varepsilon(t) = \varepsilon_0 + e\tilde{v} \cos(2\pi ft)$ , and  $\psi(x)$  is the electron's fixed spatial wavefunction. From the point of view of the rest of the device the oscillating

level does not have a definite energy. Instead it has energy components at  $\varepsilon_0$ ,  $\varepsilon_0 \pm hf$ ,  $\varepsilon_0 \pm 2hf$ , etc. This is simply seen by expanding the phase factor into its spectral components:

$$\psi(x,t) = \psi(x) \left[ \sum_{n=-\infty}^{\infty} J_n \left( \frac{e\tilde{V}}{hf} \right) \exp[-i(\varepsilon_0 + nhf) \frac{t}{\hbar}] \right] \quad (8.2)$$

where the weights of the spectral peaks are given by the Bessel functions  $J_n(e\tilde{V}/hf)$ . Note that one cannot obtain a spectrum with discrete sidebands as in Eq. (8.2) by the adiabatic procedure of averaging the instantaneous spectrum over a cycle of the oscillation. Conceptually, the presence of sidebands in the energy spectrum of a level corresponds to the absorption and emission of photons from the ac field. Therefore transport involving the sidebands of the electronic level is commonly referred to as *photon-assisted tunneling* (PAT).

Many of the experiments on photon-assisted tunneling in quantum dots [249,250], and in quantum wells [251-254], can be understood in terms of the theory developed by Tien and Gordon for time-dependent tunneling into a superconductor [245]. Tien and Gordon's theory assumes two things: First, the time-dependence must appear entirely through rigid level shifts as in Eq. (8.1). That is, all oscillating electric fields must be confined to the tunnel barriers. Second, transitions between regions with different time dependences must occur only to lowest order in perturbation theory, i.e., according to Fermi's Golden Rule. In practical application of the theory, the Golden-Rule tunneling rates across a barrier are simply modified to reflect the changed spectral densities due to the relative time dependence. For sinusoidal signals, this corresponds to including the sidebands in Eq. (8.2) into the tunneling rates.

An example in which the Tien-Gordon theory was applied successfully to transport through a quantum dot is shown in Fig. 8.3. The usual peaks in current as a function of gate voltage are modified by the application of a microwave-frequency ac bias across the dot. This modification of the current can be quantitatively understood within the Tien-Gordon picture. The ac bias causes an oscillating energy difference between the dot and the leads. The tunneling rate of electrons on and off the dot are therefore modified according to [249,255]:

$$\tilde{\Gamma}(\varepsilon) = \sum_{n=-\infty}^{\infty} J_n^2 \left( \frac{e\tilde{V}}{hf} \right) \cdot \Gamma(\varepsilon + nhf) \quad (8.3a)$$

where  $\Gamma(\varepsilon)$  is the tunneling rate in the absence of microwaves.

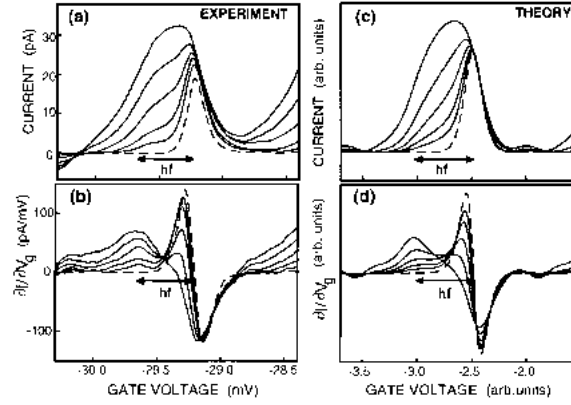


Figure 8.3. Comparison between measurement and Tien-Gordon theory for transport through a quantum dot. The parameters in the calculation are taken from the experiment; only the ac amplitudes are adjusted. The conversion of gate voltage to energy in units of  $hf$  is indicated by the arrows where  $f = 27$  GHz. (From Kouwenhoven *et al.* [249].)

Eq. (8.3a) is a special, discrete case of a general description of the interaction between tunneling electrons and photons in the environment:

$$\tilde{\Gamma}(\varepsilon) = \int_{-\infty}^{\infty} d(hf) P(hf) \Gamma(\varepsilon + hf) \quad (8.3b)$$

Here the weight function  $P(hf)$  is the spectral density function describing the fluctuations in the environment. These fluctuations include the black body radiation of the environment [256], the electrical noise that is coupled into the measurement wires [257], and excitations such as plasmons that can exist in the current and voltage leads due to their finite impedance [258]. These fluctuations are broad-band in frequency. One needs to create a special, resonating environment like an LC-oscillator [259] or apply a microwave signal at a single frequency to get a photocurrent containing sharp, discrete features.

### 8.3. PHOTOCURRENT SPECTROSCOPY OF A QUANTUM DOT.

In the experiment of Fig. 8.3, the density of states in the dot is effectively continuous and one does not see evidence of 0D-states. In contrast, a similar experiment performed on a smaller dot by Oosterkamp and coworkers [44] clearly reveals the 0D-states of the dot. For this case, Fig. 8.4 shows schematically the processes which lead to peaks in the current vs. gate voltage

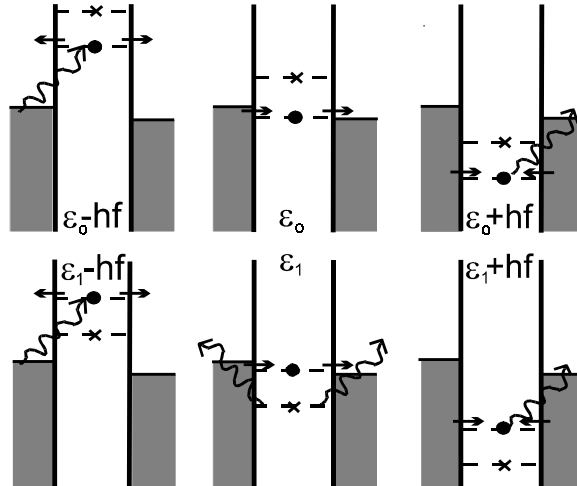


Figure 8.4. Diagrams of six processes which can lead to a current through a quantum dot with discrete OD-states driven by microwaves.  $\epsilon_0$  denotes the groundstate (lower dashed lines) and  $\epsilon_1$  the first excited state (upper dashed lines) of the  $N$ -electron system. Without microwaves only the upper-center diagram can contribute to the current. With microwaves, the indicated inelastic tunnel processes lead to photon-induced current peaks which occur at distinguishable positions in gate voltage. (From Oosterkamp *et al.* [44].)

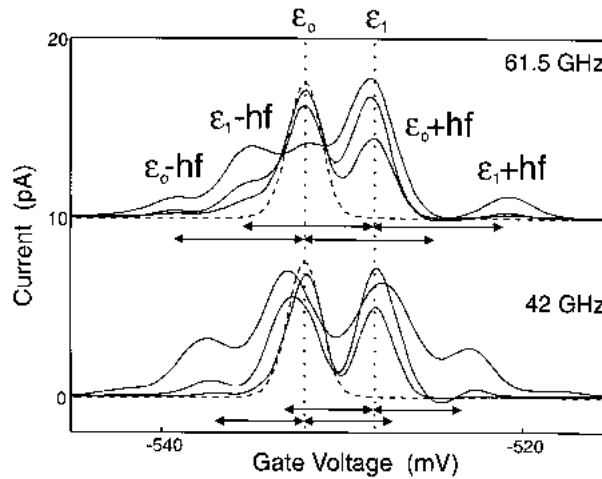


Figure 8.5. Measured, time-averaged current as a function of center-gate voltage for different microwave powers at 61.5 and 42 GHz using the device shown in Fig. 1.3. The dashed curves are without microwaves. The peaks at  $\epsilon_0$  and  $\epsilon_1$  remain fixed while the photon-assisted-tunneling sidebands at  $\epsilon_0 - hf$  and  $\epsilon_1 \pm hf$  shift proportionally to the applied microwave frequency. (From Oosterkamp *et al.* [44].)

for a dot driven by microwaves. The Tien-Gordon picture continues to apply because the ac fields are confined to the barriers and there are no oscillating fields to cause direct transitions within the dot or leads. Fig. 8.5 shows the measured current vs. gate voltage for different microwave frequencies and amplitudes. There are two types of peaks in the current: those associated with transport through the bare levels  $\varepsilon_0$  and  $\varepsilon_l$ , which remain fixed as the microwave frequency is changed, and those associated with transport through the sidebands of the levels (PAT) which shift as expected with microwave frequency. Note that the peak at  $\varepsilon_l$  is only made visible by microwave excitation of electrons out of  $\varepsilon_0$ , as shown in the bottom center diagram of Fig. 8.5. The observation of the excited-state energy level  $\varepsilon_l$  represents a spectroscopy of the quantum dot. This spectroscopy requires both the presence of the microwave field and the measurement of the time-averaged current, so it is best called a "photocurrent spectroscopy" of the dot.

#### 8.4. RABI OSCILLATIONS IN A DOUBLE QUANTUM DOT.

One interesting example of a system which cannot be treated by Tien-Gordon theory is a pair of strongly coupled quantum dots connected in series. A sinusoidal signal of the proper frequency applied to this system will result in a coherent oscillation (Rabi oscillation) of electrons between the two dots. This effect lies beyond a Golden-Rule description of transitions between the dots, and so is not accounted for in the Tien-Gordon model. For the same reason the Shapiro steps in irradiated Josephson junctions do not follow from a Golden-Rule description [97].

In the time-independent case, coherence between the dots is treated theoretically by solving for the eigenstates of the coupled dot system. In the time-dependent case, the equivalent approach is to solve for the *quasi-energy* eigenstates of the system [260]. As a simple example, which is also relevant to experiment, consider two coupled dots each of which has a single non-degenerate energy level [261-263]. The Hamiltonian is simply:

$$H = \sum_{i=1}^2 \varepsilon_i(t) d_i^\dagger d_i + w(d_2^\dagger d_1 + H.c.) \quad (8.4)$$

where the energies of the states are driven by an external sinusoidal signal,  $\varepsilon_1 = 0$ ,  $\varepsilon_2 = e\tilde{v} \cos(\omega t)$ . Since the Hamiltonian is a periodic function of time  $H(t + 2\pi/\omega) = H(t)$ , one can diagonalize the system into eigenstates of the one-period evolution operator  $U(t + 2\pi/\omega, t) = T\{\exp[-(i/\hbar) \int_t^{t+2\pi/\omega} dt' H(t')]\}$ . For the double-dot system, these states have the form [260]:

$$\psi_i^{(j)}(t) = \exp[-iE_j t / \hbar] \varphi_i^{(j)}(t) \quad (8.5)$$

where  $E_j$  is the  $j$ th quasienergy, and  $\varphi_i^{(j)}(t + 2\pi/\omega) = \varphi_i^{(j)}(t)$  is the time periodic Floquet function whose components give the time-dependent amplitudes on the two quantum dots. The quasi-energies are plotted in Fig. 8.6. Qualitatively, each avoided crossing occurs when the levels on the two dots differ by an integer number of photon energies  $\hbar\omega$ . The gap at each crossing is given by  $\approx 2wJ_n(e\tilde{v}/\hbar\omega)$ , which corresponds to the usual symmetric-antisymmetric splitting,  $2w$ , for the time-independent case weighted by the amplitude of the  $n$ th sideband,  $J_n(e\tilde{v}/\hbar\omega)$ . As in the time-independent case, the wavefunctions are delocalized at the avoided crossings. At these resonances, if an electron were placed on one of the dots, it would oscillate back and forth between the dots at a frequency  $\Omega_R = 2wJ_n(e\tilde{v}/\hbar\omega)$ . For the avoided crossings involving a nonzero number of photons, this is just the Rabi oscillation familiar from atomic physics [151].

Time-dependent transport through the double-quantum-dot system coupled to leads can be characterized by the ratio of the Rabi frequency  $\Omega_R$  to the tunneling rate to the leads  $\Gamma$ . If  $\Omega_R$  is large compared to  $\Gamma$  then electrons will perform many coherent oscillations between the dots before each tunneling event to the leads. The rate-limiting step in transport will therefore be tunneling to the leads, and so the current will be proportional to  $\Gamma$ . In the opposite limit, tunneling to the leads will be fast and only rarely will electrons tunnel between the dots (in the latter case the Tien-Gordon picture still applies to tunneling between the dots). These effects are apparent in the left part of

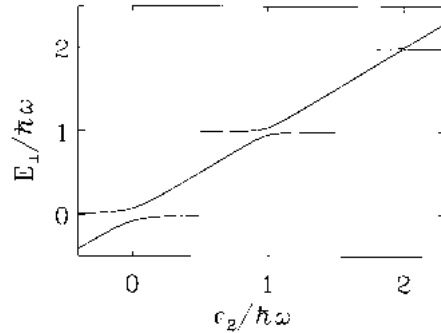


Figure 8.6. Calculated quasi-energies of two coupled quantum dots vs. detuning energy  $\varepsilon_2$ . Here  $\varepsilon_j(t) = e\tilde{v} \cos(\omega t)$ , with  $e\tilde{v} = \hbar\omega = 10w$ , where  $w$  is the hybridization matrix element between the two dots. The quasienergies are defined mod  $(\hbar\omega)$ . The electronic states on the dots hybridize and split by  $2wJ_n(e\tilde{v}/\hbar\omega)$ , becoming delocalized, when  $\varepsilon_2$  crosses the  $n$ th sideband of  $\varepsilon_1$ . (From Stafford and Wingreen [261].)

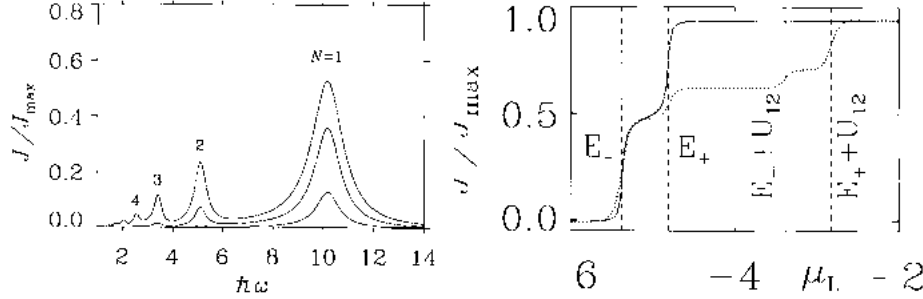


Figure 8.7. Time-averaged current  $\bar{J}$  (in units of  $J_{max} = (e\Gamma/2\hbar)$ ) through a double quantum dot with  $\varepsilon_1 = -5$ ,  $\varepsilon_2 = 5$ ,  $\Gamma = 0.5$ , and ac amplitude  $e\tilde{V} = 2, 4, 6$  (increasing  $\bar{J}$ ). Energies are given in units of  $w$ , the tunneling matrix element between the dots. With  $\mu_L = \mu_R = 0$ , the system functions as an electron pump due to coherent  $n$ -photon-assisted tunneling. Inset: Time-averaged current at the one-photon resonance versus dc bias  $\mu_L$ , with  $e\tilde{V} = 6$ . Solid curve:  $U_{12} = 0$ ; dotted curve:  $U_{12} = 2$ . The jumps allow one to resolve the Rabi splitting  $|E_+ + E_-|$  and the inter-dot interaction  $U_{12}$ . (From Stafford and Wingreen [261].)

Fig. 8.7 where the time-averaged current through a double-quantum-dot system is plotted vs  $\hbar\omega$  for different ac driving amplitudes  $\tilde{V}$ . Since in Fig. 8.7 the dc bias is large compared to the coupling to the leads  $\Gamma$ , the current at the photon-assisted-tunneling peaks is given by [261,264].

$$\bar{J}_{res} = \frac{e\Gamma}{2} \left( \frac{\Omega_R^2}{\Omega_R^2 + \Gamma^2} \right) \quad (8.6)$$

As shown on the right in Fig. 8.7, the Rabi splitting can be observed directly via transport measurements, although care must be taken to distinguish it from the Coulomb interaction  $U_{12}$  between electrons on the two dots [262].

Experimentally, time-dependent transport through a double quantum dot has been studied by Blick *et al.* [265] and by Fujisawa and Tarucha [266]. These results are best understood by first considering the charging diagram of a double quantum dot as shown in Fig. 8.8(a) (see also Fig. 4.2). The vertices, e.g.,  $V$  and  $V'$ , correspond to conditions where a pair of electron levels, one on each dot, become degenerate in energy (Fig. 8.8(b) central panel). Resonant transport can therefore occur through the two dots in series and one expects a peak in the current [103]. Such a peak is shown in the bottom panels of Fig. 8.9(a) and (b). If one applies microwaves of energy  $hf$  to the double dot, one also expects enhanced current due to the photon-assisted tunneling processes shown in the side panels of Fig. 8.8(b). This enhancement is clearly observed in the top panels of Fig. 8.9. It is natural to expect that the Rabi splitting, and

possibly time-resolved Rabi oscillations, will be observed in such a double-quantum-dot structure in the future.

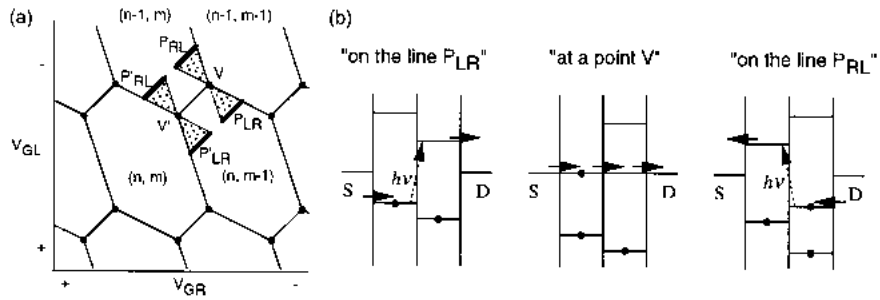


Figure 8.8. (a) Schematic charging diagram of the coupled dot system.  $(n, m)$  gives the number of electrons on the left and right dots, respectively. The 0D-0D resonant-tunneling peaks occur at the vertices, e.g.  $V$  and  $V'$ . The thick lines,  $P_{LR}$ ,  $P_{RL}$ , and so on, indicate the conditions for resonant photon-assisted tunneling. (b) Energy diagram for photon-assisted tunneling on the line  $P_{LR}$ , for ordinary resonant tunneling at the point  $V$ , and for photon-assisted tunneling on the line  $P_{RL}$ . (From Fujisawa and Tarucha [266].)

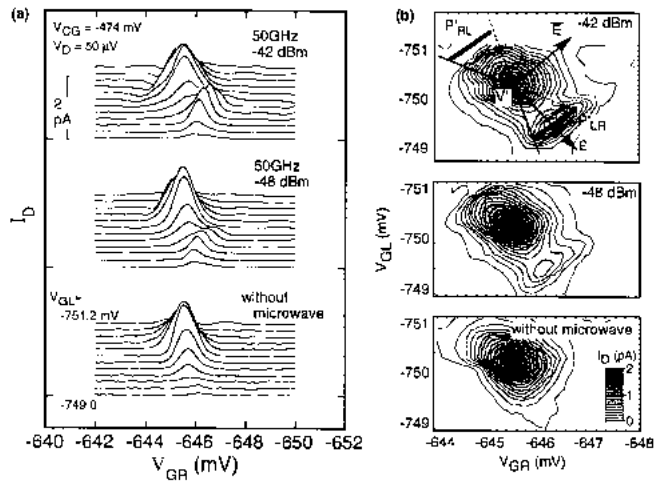


Figure 8.9. (a) Current vs. two gate voltages for increasing microwave power from bottom to top panel. On applying microwaves the photon sideband becomes visible. (b) Contour plot of the observed current near point  $V'$  in Fig. 8.8. Note the clear signature of photon-assisted tunneling along the segment  $P'_{LR}$ . (From Fujisawa and Tarucha [266].)

## 9. Conclusions and future directions.

The field of electron transport through quantum dots has progressed from its first tentative steps to maturity in less than ten years. This startling rate of progress might be attributed to a confluence of fabrication, refrigeration, and measurement technologies. It may be more honest, however, to attribute the rapid progress to the fundamental simplicity of the behavior of electrons in quantum dots. New experimental results have rarely waited more than a year or two to find satisfactory theoretical explanation. "What is that makes quantum dots so simple?" The answer is the strong separation of energy scales in dots. The largest relevant energy is the Coulomb interaction energy,  $\sim 1$  meV in lateral dots and  $\sim 10$  mV in vertical dots. (All energies larger than this, say the bandgap or intervalley energies of GaAs, are frozen out and play no role in the dynamics of the dot.) The next relevant energy scale is the single particle level spacing,  $\sim 0.1$  meV in lateral dots and  $\sim 1$  mV in vertical dots. Last is the coupling energy between the dot and the leads which for opaque tunnel barriers is  $\sim 0.01$  meV. The energy scale set by the temperature merely determines which of these other scales can be resolved in transport of electrons through the dot.

As a result of the separation of energy scales, the behavior of electrons in dots can often be understood in a simple hierarchical way: First, the number of electrons on the dot is determined by minimizing the direct Coulomb interaction energy. Second, the state of these electrons on the dot is determined by balancing their kinetic energy against the residual parts of the Coulomb interaction, including correlation and exchange effects. Finally, the transition rates among such states are determined by the small hybridization energy to the leads. When this hierarchical scheme applies, the agreement between experiment and theory is often startlingly good. The few outstanding experimental puzzles in transport through dots correspond to those cases when two or more energy scales are brought into competition. Examples that we have discussed include: charge fluctuations or co-tunneling events between dots and leads or between two dots when the tunnel coupling energy is equal to or larger than the single-particle energy separation; the formation of Landau levels at high magnetic field with a Zeeman energy or cyclotron energy of order either the single-particle energies or the Coulomb energy.

The overall simplicity of transport through dots may in the long run prove to be the field's greatest blessing. This simplicity has certainly permitted the accumulation of a core of well explored and well understood phenomena. While no single great discovery has characterized the study of electron transport in dots, many small discoveries coming in rapid succession have added up to a big advance. Today, researchers armed with fabrication

techniques developed over the past ten years, and also armed with a good understanding of the basic phenomenology of dots, are pursuing many new directions both technological and scientific. Dots are being used in the study of other systems, dots and other mesoscopic structures are combined into mini-laboratories on a chip, and the complex regimes where several energy scales compete in a dot are under exploration. Some of this current research has been touched on in the previous chapters. It seems appropriate in the remaining space to point to a few directions which seem most promising in the near and not so near future. The following sections briefly address (9.1) technological and (9.2) novel scientific applications of transport through quantum dots, and (9.3) quantum dot physics in other systems.

### 9.1. TECHNOLOGICAL APPLICATIONS.

The ability to measure and control current at the single-electron level has a number of potential uses, ranging from metrology to electrometry to computing [267]. In fact, both metal and semiconductor quantum dots are already finding niche applications, though their utility is limited because of the low temperatures required. To broaden their usage, devices must be developed that operate under ambient conditions, i.e. at room temperature. Ways of accomplishing this will be discussed in section 9.3.

One of the most important Coulomb blockade application is single-electrometry - the detection of single charges. As discussed already, these devices are very sensitive to small changes in their local electrostatic environment. Sensitivities of  $10^{-5} e/\text{Hz}^{1/2}$  are possible [268]. In other words, the electrometer can detect a charge  $e$  in one second if  $10^{-5}$  of the field lines leaving the charge terminate on the dot. These devices are the electrostatic counterpart to the SQUID, a superconducting device which is sensitive to extremely small magnetic fluxes. There are important differences, however [267]. SQUIDs can be used to measure macroscopic magnetic fields by utilizing flux transformers to couple the macroscopic magnetic field into the SQUID. No such transformer exists to date for electric charge, so the change in the charge over a large object cannot be carefully measured. Nevertheless, as a local electrometer, semiconductor as well as metallic dots may find many uses. Already, they have been used in scientific applications, mainly to monitor the behavior of single electrons in other circuits. We have discussed the semiconductor electrometers in section 4 (e.g. see Fig. 4.1), discussions of the metallic electrometers can be found in Refs. 93,268-270.

Another application is in the field of metrology. The single electron turnstile, and related devices in metal dots, are being investigated as current standards. They produce a standardized current from a standardized RF

frequency, with the conversion factor being the electronic charge  $e$ . Accuracies of 15 parts in  $10^9$  have been obtained in multi-dot metallic circuits [244]. These turnstiles would complete the solid-state device “metrology triangle” relating frequencies, currents and voltages [24]. Already, the quantum Hall effect is used to relate current to voltage, and the Josephson effect to relate frequency to voltage. The turnstile would fill in the last leg of the triangle by relating frequencies to currents.

Another application is the measurement and regulation of temperature. As discussed in section 3, the Coulomb blockade peak widths are proportional to  $k_B T$ , and can, once calibrated, be used to measure the temperature of the dot or its surroundings. Even at higher temperatures, where most of the Coulomb structure has been washed out, there are slight non-linearities in the  $I$ - $V$  characteristic that can be used to measure  $T$  [271]. Temperature gradients can also be detected, as thermopower measurements of dots have shown [272]. Quantum dots may be able to control the temperature as well as measure it. A quantum dot “refrigerator” that can cool a larger electronic system has been proposed [122]. The idea is to use tunneling through single quantum levels to skim off the hot electrons above  $E_F$ , thereby cooling the electron system.

The experiments discussed in section 8 showed that photon-assisted tunneling over the Coulomb gap can induce DC currents through a quantum dot. This suggests applications for dots as photon detectors in the microwave regime. The tunability of the dot potential relative to the source and drain means that the detector can be frequency-selective. It is even possible for a single photon to lead to a current of many electrons [273]. Photon-detection applications are not limited to the microwave region. For example, a metallic dot operating as a single-electrometer has been utilized to (indirectly) detect visible photons. The dot was fabricated on a semiconductor substrate, and was then used to electrostatically detect the presence of photoexcited electrons within the semiconductor [273].

One can also contemplate electronics applications for these devices - a field sometimes called single-electronics. It is in principle possible to perform calculations using quantum dot circuits, based on either charging [274] or quantum-coherent phenomena [88], although little experimental work has been done in this direction. Multi-dot circuits can also serve as static memory elements. This has been tested in the laboratory; for example, a single-electron memory with a hold time of several hours (at millikelvin temperatures) has been demonstrated [93]. One must exercise extreme caution in extrapolating these successes to a useful product, however. The technological barriers to creating complex circuits that work in the real world are enormous.

## 9.2. SCIENTIFIC APPLICATIONS.

One of the most promising scientific directions in quantum dot research is the use of dots as part of on-chip laboratories. The first steps have already been taken in this direction, with encouraging results. As discussed in section 4, combining two or more dots in close proximity has allowed an exploration of the crossover from a double dot to a single dot as the barrier between the dots is removed. An important question is: "How do charge fluctuations drive this crossover?" The systematic control offered by the double dot structure is a powerful tool for answering this question. Another phenomenon susceptible to study in double-dot structures is the coherent delocalization of single-particle levels between dots. In the presence of ac fields, this delocalization corresponds to the Rabi oscillations discussed in section 8. By extending delocalization to multiple dots, the formation of coherent bands is possible [37].

Multiple dot structures are only one possibility for on-chip laboratories. Dots, wires, rings, and gates can be integrated into more complex structures. A beautiful example of this kind of integrated structure was employed in a series of experiments on quantum coherence by researchers at the Weizmann Institute [126,127]. In the experiments, a quantum dot was embedded in one arm of an Aharonov-Bohm ring; see Fig. 4.10. By measuring the amplitude and phase of the resulting Aharonov-Bohm oscillations the coherent transmission amplitude of the dot, including the phase-shift, was determined. In addition to proving that transmission through dots can be coherent, the research uncovered an unexpected phase-slip between Coulomb-blockade conductance peaks. Perhaps most importantly the experiments have opened up the possibility of studying, in a controlled way, dephasing of quantum transport by the environment.

Fig. 9.1 contains a schematic of such an integrated on-chip laboratory for studying dephasing. The Aharonov-Bohm ring plus quantum dot is augmented by a quantum point contact in close proximity to the dot. This quantum point contact forms a controllable "environment" for electrons on the dot. An extra electron on the dot changes the transmission amplitude through the point contact. Hence the point contact acts as an electrometer for the number of electrons on the dot [94]. Since number and phase are conjugate variables, the quantum point contact results in dephasing of electron transport through the dot, and suppresses the Aharonov-Bohm oscillations [275,276].

The technological and scientific applications are of course connected. For example, we have mentioned in sections 4 and 9.1 the possibility of using quantum dots as elements in a quantum computer [87,88]. The construction of even a simple prototype quantum computer out of solid state elements is technologically extremely complicated and will not be accomplished during

this century. Nevertheless, the ideas around quantum computation do generate new scientific directions. One direction is the measurement and control of dephasing. The idea is that even though a quantum dot may be a non-dissipative system, the electrons on the dot interact with electrons, or more generally, with other degrees of freedom in the environment such as the nearby point contact in Fig. 9.1. In the ring-dot-point-contact geometry the interaction collapses the wavefunction and the interference between the amplitudes traveling along the two arms of the ring gets suppressed. Since a quantum computer should be fully coherent, dephasing simply implies an error. Therefore, control over the environment is a necessary requirement for successfully building a quantum computer. We foresee in the near future a research direction which could be described as *mesoscopic environmental engineering*. Another direction stimulated by the recent proposals on quantum computers is the control in time of bits. (For a quantum computer the bits are called *qubits*.) This control in time is called handshaking in ordinary computers and could be called *quantum handshaking* in quantum computers since the control needs to occur within the phase coherence time. For quantum dots it means that the single electron tunneling events are regulated on times scales as short as 1 ns to 1 ps. Experiments such as observing the predicted Rabi oscillations [261,262] and the control of tunneling using short pulses [246,247] would be a first step to accomplishing quantum handshaking.

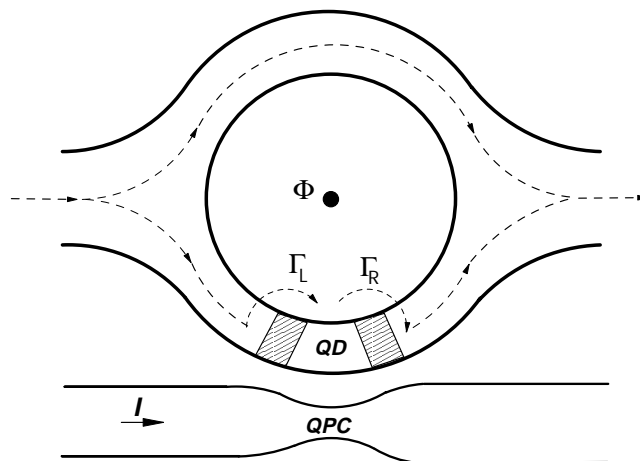


Figure 9.1. Schematic view of the "Which Path?" interferometer [275]. A quantum dot is built in one arm of an Aharonov-Bohm ring. The transmission amplitude of the nearby quantum point contact depends on the occupation number of the dot. Since number and phase are conjugate, the quantum point contact produces dephasing of electrons passing through the dot, and suppresses the Aharonov-Bohm oscillations. (From Aleiner *et al.* [276].)

### 9.3. OTHER SYSTEMS.

Quantum dots are really just a generic example of a small, confined structure containing electrons. There is no fundamental physical discontinuity between a quantum dot and a large molecule or even an atom. There should be no surprise then, that the physics of dots applies as well to small metallic particles, clusters, and molecules [277]. In this section, we point out a few recent examples where the ideas and measurement techniques developed in the study of quantum dots have been applied to ever-smaller systems.

The analogy to quantum dots is particularly clean in the case of metal nanoparticles. In experiments at Harvard, Al particles of a few nanometer size were studied in a Coulomb blockade geometry [29]. The charging energy  $\sim 10$  meV, and level spacings  $\sim 0.1$  meV, appear in  $I$ - $V$  traces in exactly the same fashion as in semiconductor dots. The larger separation between charging energy and level spacing and the Fermi liquid nature of the states on the nanoparticle in fact make the metallic case somewhat easier to understand in detail [278]. In addition, the rich behavior introduced by superconductivity in the dots and/or the leads makes these nanoparticles a topic of ongoing interest. [29, 279]

Another promising approach utilizes metal or semiconductor nanoparticles made by synthetic chemistry and subsequently incorporated into electrodes. Fig. 9.2 shows an example taken from Klein *et al.* [280]. Six nm diameter CdSe nanocrystals are bound to electrodes using a molecular linker. The conductance versus gate voltage shows Coulomb oscillations; nonlinear measurements reveal a charging energy of  $\sim 30$  meV.

The use of molecules as Coulomb blockade structures is not merely theoretical speculation. For example, Porath *et al.* [281], has recently used an STM to explore transport through  $C_{60}$  molecules deposited on a gold substrate. These measurements clearly show features associated with Coulomb blockade and level quantization [281]. Fig. 9.3(a) shows a schematic of the measurement geometry, and Fig. 9.3(b) shows  $dI/dV_{sd}$  as a function of  $V_{sd}$ . A large gap is observed, followed by a series of peaks associated with tunneling into the excited states of the molecule. The large gap is a combination of Coulomb charging ( $\sim 0.4$  eV) and the energy-level difference between the lowest unoccupied molecular orbital (LUMO) and highest occupied molecular orbital (HOMO) level. This HOMO/LUMO band gap is easily incorporated in standard models of the Coulomb blockade, and agreement with the experiment is good. Joachim and Gimzewski [282] have recently shown that single  $C_{60}$  molecules can operate as an amplifier through their electromechanical properties. Other molecules have also been studied, including a recent report of a gated single-electron transistor operating at room temperature [283].

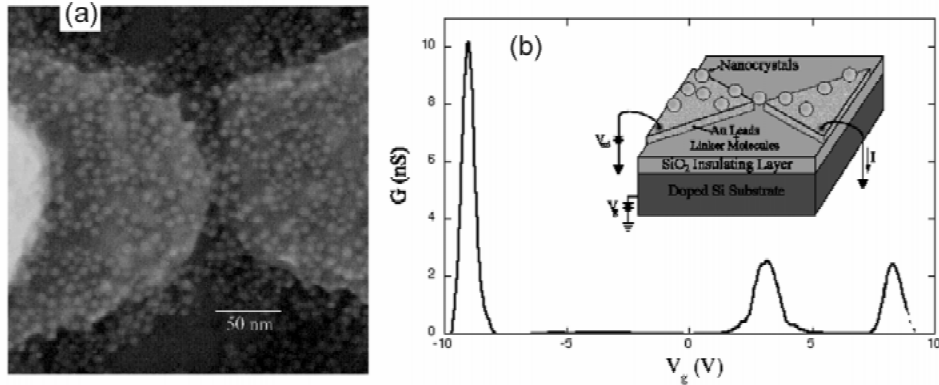


Figure 9.2. Single nanocrystal transistor. (a) SEM micrograph of 5.5 nm diameter CdSe nanocrystals bound to lithographically patterned gold electrodes. (b) Inset: Schematic of the device, showing a single nanocrystal bridging the leads. A gate voltage can be applied to the conducting substrate. Main Panel: Conductance versus gate voltage measured at 4.2 K showing three Coulomb oscillations. (From Klein *et al.* [280].)

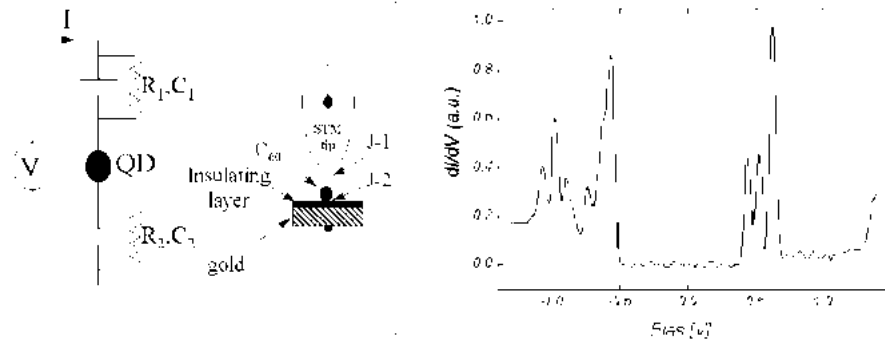


Figure 9.3. Left: Schematic diagram and equivalent circuit of a double-junction system realized by a  $C_{60}$  molecule weakly coupled to an STM tip and to a gold substrate. Right: Tunneling spectroscopy  $dI/dV_{sd}$  as a function of  $V_{sd}$  at 4.2 K. The first discrete state observed for negative bias corresponds to the HOMO and the first state for positive bias corresponds to the LUMO. (From Porath *et al* [281].)

Carbon nanotubes, the extended cousins of  $C_{60}$ , have also proven to be a system that can be understood using the ideas developed for dots [284,285]. The nanotube is predicted to act as a one-dimensional quantum wire, and a finite length turns it into a one-dimensional quantum dot. Fig. 9.4(a) shows a bundle of single walled carbon nanotubes to which electrical leads have been

patterned. The conductance on a 200 nm segment between two of the contacts versus gate voltage shows Coulomb oscillations, as is seen in Fig. 9.4(b). The inset shows the temperature dependence; the peak height decreases with increasing temperature, indicating resonant tunneling through a single quantum level delocalized over the entire length of the tube. Nonlinear transport measurements indicate that the charging energy is  $\sim 10$  meV and the level spacing is  $\sim 3$  meV, consistent with estimations for a 1D conductor of  $\sim 200$  nm in length.

Clearly, these molecular systems offer many exciting options for future research. Since the charging and level spacings are quite large, it is possible to investigate physics that lies at lower energy scales than is accessible in lithographically patterned quantum dots. For example, the long-standing prediction of a Kondo resonance between a localized spin on a quantum dot and the Fermi seas in the leads may finally succumb to experimental investigation. Of course, there are new phenomena in these systems as well: superconductivity in metal particles with level spacings as large as the superconducting gap, surface states and bandgap pinning in clusters, and strong electron-lattice interactions in molecules, etc. If the history of the field has been any guide, new surprises also await us in these systems in the years to come.

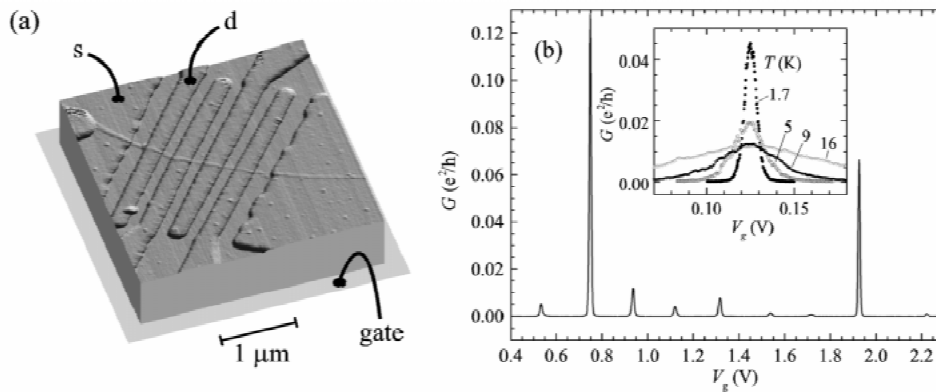


Figure 9.4. (a) AFM image of a single-walled nanotube bundle to which multiple electrical leads have been attached. A gate voltage can be applied to the conducting substrate to change the number of electrons on the tubes. (b) Main Panel: Measurement of the conductance versus gate voltage of the 200 nm segment between the leftmost leads. Dramatic Coulomb oscillations are observed. Inset: Temperature dependence of a selected peak. The peak height increases as the temperature is lowered, indicating coherent transport through a single quantum level. (From Bockrath *et al.* [284].)

**Acknowledgements:** We gratefully acknowledge our (numerous!) collaborators at UC Berkeley, Delft, Harvard, MIT, NEC, NTT, Philips, Stanford, and the University of Tokyo who, with the authors, performed most of the work presented here. We also thank our colleagues R. Ashoori, R. Akis, H. Bruus, C.W.J. Beenakker, A.M. Chang, D. Ferry, R.A. Jalabert, O. Klein, D.A. Wharam, T. Schmidt, U. Sivan, M. Stopa, H. Tamura, and A. Yacoby who graciously provided figures for this review.

## References.

- [1] M. Reed, *Scientific American* **268**, 118 (1993).
- [2] M. Kastner, *Physics Today* **46**, 24 (1993).
- [3] *Single Charge Tunneling*, edited by H. Grabert and M.H. Devoret (Plenum Press, 1991).
- [4] D.V. Averin and K.K. Likharev, *J. Low Temp. Phys.* **62**, 345, (1986); and in: *Mesoscopic Phenomena in Solids*, edited by B.L. Altshuler, P.A. Lee, and R.A. Webb (Elsevier, 1991).
- [5] G. Schön and A.D. Zaikin, *Physics Reports* **198**, 237 (1990); G.-L. Ingold and Yu. V. Nazarov, in Ref. 3; R. Fazio and G. Schön, in this volume.
- [6] C.W.J. Beenakker, *Phys. Rev. B* **44**, 1646 (1991).
- [7] H. van Houten, C.W.J. Beenakker, A.A.M. Staring, in Ref. 3.
- [8] U. Meirav and E.B. Foxman, *Semicond. Sci. Technol.* **10**, 255 (1995).
- [9] L.P. Kouwenhoven and P.L. McEuen, in *Nano-Science and Technology*, edited by G. Timp (AIP Press, 1997). Parts of the present introduction sections can also be found in this review.
- [10] Special issue on *Single Charge Tunneling*, edited by H. Grabert, in *Zeitschrift für Physik B* **85** (1991).
- [11] Special issue on *Few-Electron Nanostructures*, edited by L.J. Geerligs, C.J.P.M. Harmans, and L.P. Kouwenhoven, in *Physica B* **189** (1993).
- [12] C.J.P.M. Harmans, *Physics World* **5**, 50 (1992).
- [13] K.K. Likharev and T. Claeson, *Scientific American* **266**, 50 (1992).
- [14] M.H. Devoret, D. Esteve, and C. Urbina, *Nature* **360**, 547 (1992).
- [15] R.C. Ashoori, *Nature* **379**, 413 (1996).
- [16] Y. Nagamune, H. Sakaki, L.P. Kouwenhoven, L.C. Mur, C.J.P.M. Harmans, J. Motohisa, and H. Noge, *Appl. Phys. Lett.* **64**, 2379 (1994).
- [17] L.I. Glazman and R.I. Shekhter, *J. Phys.: Condens. Matter* **1**, 5811 (1989).
- [18] L. P. Kouwenhoven, N.C. van der Vaart, A.T. Johnson, W. Kool, C.J.P.M. Harmans, J.G. Williamson, A.A.M. Staring, and C.T. Foxon, *Z. Phys. B* **85**, 367 (1991).
- [19] R.A. Millikan, *Phys. Rev.* **32**, 349, (1911).
- [20] C.J. Gorter, *Physica* **17**, 777 (1951).
- [21] I. Giaever and H.R. Zeller, *Phys. Rev. Lett.* **20**, 1504 (1968).
- [22] J. Lambe and R.C. Jaklevic, *Phys. Rev. Lett.* **22**, 1371 (1969).
- [23] I.O. Kulik and R.I. Shekhter, *Zh. Eksp. Teor. Fiz.* **68**, 623 (1975) [*Sov. Phys. JETP* **41**, 308 (1975)].
- [24] K.K. Likharev, *IEEE Trans. Magn.* **23**, 1142 (1987); *IBM J. Res. Dev.* **32**, 144 (1988).
- [25] K. Mullen, E. Ben Jacob, R.C. Jaklevic, and Z. Schuss, *Phys. Rev. B* **37**, 98 (1988); M. Amman, K. Mullen, and E. Ben-Jacob, *J. Appl. Phys.* **65**, 339 (1989).

- [26] T.A. Fulton and G.J. Dolan, Phys. Rev. Lett. **59**, 109 (1987).
- [27] L.L. Sohn, M. Crommie, and H. Hess, in this volume.
- [28] C. Schönenberger, H. van Houten, H.C. Donkersloot, Europhys. Lett. **20**, 249 (1992).
- [29] D.C. Ralph, C.T. Black, J.M. Hergenrother, J.G. Lu, and M. Tinkham, in this volume.
- [30] D.L. Klein, P.L. McEuen, J.E. Bowen Katari, R. Roth, A.P. Alivisatos, Appl. Phys. Lett., **68**, 2574 (1996).
- [31] M.A. Reed, J.N. Randall, R.J. Aggarwall, R.J. Matyi, T.M. Moore, and A.E. Wetsel, Phys. Rev. Lett. **60**, 535 (1988).
- [32] L.P. Kouwenhoven, G. Schön, and L.L. Sohn, in this volume.
- [33] B.J. van Wees, H. van Houten, C.W.J. Beenakker, J.G. Williamson, L.P. Kouwenhoven, D. van der Marel, and C.T. Foxon, Phys. Rev. Lett. **60**, 848 (1988).
- [34] D.A. Wharam, T.J. Thornton, R. Newbury, M. Pepper, H. Ahmed, J.E.F. Frost, D.G. Hasko, D.C. Peacock, D.A. Ritchie, and G.A.C. Jones, J. Phys. C **21**, L209 (1988).
- [35] C.W.J. Beenakker and H. van Houten, Solid State Physics **44**, 1 (1991). This reviews transport in mesoscopic systems in which single electron charging is not important.
- [36] B.J. van Wees, L.P. Kouwenhoven, C.J.P.M. Harmans, J.G. Williamson, C.E. Timmering, M.E.I. Broekaart, C.T. Foxon, and J.J. Harris, Phys. Rev. Lett. **62**, 2523 (1989).
- [37] L.P. Kouwenhoven, F.W.J. Hekking, B.J. van Wees, C.J.P.M. Harmans, C.E. Timmering, and C.T. Foxon, Phys. Rev. Lett. **65**, 361 (1990).
- [38] J.H.F. Scott-Thomas, S.B. Field, M.A. Kastner, H.I. Smith, and D.A. Antonadis, Phys. Rev. Lett. **62**, 583 (1989).
- [39] H. van Houten and C.W.J. Beenakker, Phys. Rev. Lett. **63**, 1893 (1989).
- [40] U. Meirav, M.A. Kastner, H. Heiblum, and S.J. Wind, Phys. Rev. B **40**, 5871 (1989).
- [41] S.B. Field, M.A. Kastner, U. Meirav, J.H.F. Scott-Thomas, D.A. Antonadis, H.I. Smith, and S.J. Wind, Phys. Rev. B **42**, 3523 (1990).
- [42] A.A.M. Staring, H. van Houten, C.W.J. Beenakker, and C.T. Foxon, *High magnetic fields in semiconductor physics III*, edited by G. Landwehr (Springer, Berlin, 1990).
- [43] M.A. Kastner, Rev. Mod. Phys. **64**, 849 (1992).
- [44] T.H. Oosterkamp, L.P. Kouwenhoven, A.E.A. Koolen, N.C. van der Vaart, and C.J.P.M. Harmans, Phys. Rev. Lett. **78**, 1536 (1997).
- [45] M. Stopa, Phys. Rev. B **48**, 18340 (1993); and Phys. Rev. B **54**, 13767 (1996).
- [46] M. Macucci, K. Hess, and G.J. Iafrate, Phys. Rev. B **48**, 17354 (1993).
- [47] D. Jovanovic, and J.P. Leburton, Phys. Rev. B **49**, 7474 (1994).
- [48] B. Meurer, D. Heitmann, and K. Ploog, Phys. Rev. Lett. **68**, 1371 (1992).
- [49] W. Hansen, T.P. Smith, III, K.Y. Lee, J.A. Brum, C.M. Knoedler, J.M. Hong, and D.P. Kern, Phys. Rev. Lett. **62**, 2168 (1989).
- [50] R.C. Ashoori, H.L. Störmer, J.S. Weiner, L.N. Pfeiffer, K.W. Baldwin, and K.W. West, Phys. Rev. Lett. **68**, 3088 (1992); R.C. Ashoori, H.L. Störmer, J.S. Weiner, L.N. Pfeiffer, S.J. Pearton, K.W. Baldwin, and K.W. West, Phys. Rev. Lett. **71**, 613 (1993).
- [51] A.N. Korotkov, D.V. Averin, and K.K. Likharev, Physica B **165&166**, 927 (1990); D.V. Averin, A.N. Korotkov, and K.K. Likharev, Phys. Rev. B **44**, 6199 (1991).
- [52] Y. Meir, N.S. Wingreen, and P.A. Lee, Phys. Rev. Lett. **66**, 3048 (1991).
- [53] D.V. Averin and Yu.V. Nazarov, in Ref. 3.
- [54] Yu.V. Nazarov, J. Low Temp. Phys. **90**, 77 (1993).
- [55] D.V. Averin, Physica B **194-196**, 979 (1994).
- [56] H. Schoeller, Physica B **194-196**, 1057 (1994); H. Schoeller and G. Schön, Phys. Rev. B **50**, 18436 (1994)

- [57] A.D. Stone, and P.A. Lee, Phys. Rev. Lett. **54**, 1196 (1985).
- [58] L.J. Geerligs, D.V. Averin, and J.E. Mooij, Phys. Rev. Lett. **65**, 3037 (1990); and L.J. Geerligs, M. Matters, and J.E. Mooij, Physica B **194-196**, 1267 (1994).
- [59] T.M. Eiles, G. Zimmerli, H.D. Jensen, and J. Martinis, Phys. Rev. Lett. **69**, 148 (1992).
- [60] C. Pasquier, U. Meirav, F.I.B Williams, D.C. Glatli, Y. Jin, and B. Etienne, Phys. Rev. Lett. **70**, 69 (1993); and D.C. Glatli, Physica B **189**, 88 (1993).
- [61] L.I. Glazman and M.E. Raikh, Pis'ma Zh. Eksp. Teor. Fiz. **47**, 378 (1988) [JETP Lett. **47**, 452 (1988)].
- [62] T.K. Ng and P.A. Lee, Phys. Rev. Lett. **61**, 1768 (1988).
- [63] A. Kawabata, J. Phys. Soc. Jpn. **60**, 3222 (1991).
- [64] S. Hershfield, J.H. Davies, and J.W. Wilkins, Phys. Rev. Lett. **67**, 3720, (1991); Phys. Rev B **46**, 7046 (1992).
- [65] Y. Meir, N.S. Wingreen, and P.A. Lee, Phys.Rev. Lett. **70**, 2601 (1993).
- [66] T. Inoshita, A. Shimizu, Y. Kuramoto, H. Sakaki, Phys. Rev. B **48**, 14725 (1993).
- [67] J. König, H. Schoeller, and G. Schön, Phys. Rev. Lett. **76**, 1715 (1996); J. König, J. Schmid, H. Schoeller, and G. Schön, Phys. Rev. B **54**, 16820 (1996); H. Schoeller, in this volume.
- [68] D.C. Ralph and R.A. Buhrman, Phys. Rev. Lett. **72**, 3401 (1994).
- [69] I.K. Yanson, V.V. Fisun, R. Hesper, A.V. Khotkevich, J.M. Krans, J.A. Mydosh, and J.M. Ruitenbeek, Phys. Rev. Lett. **74**, 302 (1995).
- [70] A. Kumar, S.E. Laux, F. Stern, Phys. Rev. B **42**, 5166 (1990).
- [71] G.W. Bryant, Phys. Rev. B **39**, 3145 (1989).
- [72] D. van der Marel, in *Nanostructure Physics and Fabrication*, eds. M.A. Reed and W.P. Kirk (Academic Press 1989).
- [73] L. Wang, J.K. Zhang, and A.R. Bishop, Phys. Rev. Lett. **73**, 585 (1994).
- [74] U. Merkt, J. Huser, M. Wagner, Phys. Rev. B **43**, 7320 (1991).
- [75] D. Pfannkuche, R.R. Gerhardt, P.A. Maksym, and V. Gudmundsson, Physica B **189**, 6 (1993); see also references therein.
- [76] N.F. Johnson, J. Phys.: Condens. Matter **7**, 965 (1995).
- [77] M. Wagner, U. Merkt, and A.V. Chaplik, Phys. Rev. B **45**, 1951 (1992).
- [78] Bo Su; V.J. Goldman; J.E. Cunningham, Surface Science **305**, 566 (1994).
- [79] J.G. Williamson, A.A.M. Staring, L.P. Kouwenhoven, H. van Houten, C.W.J. Beenakker, C.E. Timmering, M. Mabesoone, and C.T. Foxon, in: *Nanostructures and Mesoscopic Systems*, edited by M.A. Reed, and W.P. Kirk (Academic Press, 1991).
- [80] E.B. Foxman, P.L. McEuen, U. Meirav, N.S. Wingreen, Y. Meir, P.A. Belk, N.R. Belk, M.A. Kastner, and S.J. Wind, Phys. Rev. B **47**, 10020 (1993).
- [81] E.B. Foxman, U. Meirav, P.L. McEuen, M.A. Kastner, O. Klein, P.A. Belk, D.M. Abusch, and S.J. Wind, Phys. Rev B **50**, 14193 (1994).
- [82] A.T. Johnson, L.P. Kouwenhoven, W. de Jong, N.C. van der Vaart, C.J.P.M. Harmans, and C.T. Foxon, Phys. Rev. Lett. **69**, 1592 (1992).
- [83] N.C. van der Vaart, A.T. Johnson, L.P. Kouwenhoven, D.J. Maas, W. de Jong, M.P. de Ruyter van Steveninck, A. van der Enden, C.J.P.M. Harmans, and C.T. Foxon, Physica B **189**, 99 (1993).
- [84] D. Weinmann, W. Hausler, W. Pfaff, B. Kramer, and U. Weiss, Europhys. Lett. **26**, 467 (1994); D. Weinmann, W. Hausler, B. Kramer, Phys. Rev. Lett. **74**, 984 (1995).
- [85] J. Weis, R.J. Haug, K. v. Klitzing, and K. Ploog, Phys. Rev. Lett. **71**, 4019 (1993).
- [86] L.P. Kouwenhoven, Science **268**, 1440 (1995).
- [87] R.P. Feynman, Foundations of Physics **16**, 507 (1986).

- [88] S. Lloyd, *Science* **261**, 1569 (1993).
- [89] L.J. Geerligs, V.F. Anderegg, P.A.M. Holweg, J.E. Mooij, H. Pothier, D. Esteve, C. Urbina, M.H. Devoret, *Phys. Rev. Lett.* **64**, 2691 (1990).
- [90] L.P. Kouwenhoven, A.T. Johnson, N.C. van der Vaart, A. van der Enden, and C.J.M.P. Harmans, *Phys. Rev. Lett.* **67**, 1626 (1991).
- [91] H. Pothier, P. Lafarge, P.F. Orfila, C. Urbina, D. Esteve and M.H. Devoret, *Physica B* **169**, 573 (1991).
- [92] H. Pothier, P. Lafarge, C. Urbina, D. Esteve, and M.H. Devoret, *Europhys. Lett.* **17**, 249 (1992).
- [93] P.D. Dresselhaus, L. Ji, S. Han, J.E. Lukens, and K.K. Likharev, *Phys. Rev. Lett.* **72**, 3226 (1994).
- [94] M. Field, C.G. Smith, M. Pepper, D.A. Ritchie, J.E.F. Frost, G.A.C. Jones, and D.G. Hasko, *Phys. Rev. Lett.* **70**, 1311 (1993).
- [95] F. Hoffmann, T. Heinzel, D.A. Wharam, J.P. Kotthaus, G. Böhm, W. Klein, G. Tränkel, and G. Weimann, *Phys. Rev. B* **51**, 13872 (1995).
- [96] C.H. Crouch, Ph.D. Thesis, Harvard University (1996).
- [97] M. Tinkham, *Superconductivity, 2nd Ed.* (McGraw-Hill, New York, 1996).
- [98] L.I. Glazman and V. Chandrasekhar, *Europhys. Lett.* **19**, 623 (1992).
- [99] I.M. Ruzin, V. Chandrasekhar, E.I. Levin, and L.I. Glazman, *Phys. Rev. B* **45**, 13469 (1992).
- [100] M. Kemerink, and L.W. Molenkamp, *Appl. Phys. Lett.* **65**, 1012 (1994).
- [101] F.R. Waugh, M.J. Berry, C.H. Crouch, C. Livermore, D.J. Mar, R.M. Westervelt, K.L. Campman, and A.C. Gossard, *Phys. Rev. B* **53**, 1413 (1996).
- [102] F.R. Waugh, M.J. Berry, D.J. Mar, R.M. Westervelt, K.L. Campman, and A.C. Gossard, *Phys. Rev. Lett.* **75**, 705 (1995).
- [103] N. C. van der Vaart, S.F. Godijn, Y.V. Nazarov, C.J.P.M. Harmans, J.E. Mooij, L.W. Molenkamp, and C.T. Foxon, *Phys. Rev. Lett.* **74**, 4702 (1995); and N. C. van der Vaart, Ph.D. Thesis, T.U. Delft (1995).
- [104] C. Livermore, C.H. Crouch, R.M. Westervelt, K.L. Campman, and A.C. Gossard, *Science* **274**, 1332 (1996).
- [105] A.S. Adourian, C. Livermore, R.M. Westervelt, K.L. Campman, and A.C. Gossard, *Superlattices and Microstructures* **20**, 411 (1996); and submitted to *Appl. Phys. Lett.* (1997).
- [106] R.H. Blick, R.J. Haug, J. Weis, D. Pfannkuche, K. v. Klitzing, K. Eberl, *Phys. Rev. B* **53**, 7899 (1996).
- [107] D. Dixon, L.P. Kouwenhoven, P.L. McEuen, Y. Nagamune, J. Motohisa, N. Sakaki, *Phys. Rev. B* **53**, 12625 (1996).
- [108] S.V. Panyukov and A.D. Zaikin, *Phys. Rev. Lett.* **67**, 3168 (1991).
- [109] D.S. Golubev and A.D. Zaikin, *Phys. Rev. B* **50**, 8736 (1994).
- [110] G. Falci, J. Heins, G. Schön, and G.T. Zimanyi, *Physica B* **203**, 409 (1994); G. Falci, G. Schön, and G.T. Zimanyi, *Phys. Rev. Lett.* **74**, 3257 (1995); J. König, H. Schoeller, and G. Schön, *Europhys. Lett.* **31**, 31 (1995).
- [111] H. Grabert, *Phys. Rev. B* **50**, 17364 (1994).
- [112] C.A. Stafford and S. Das Sarma, *Phys. Rev. Lett.* **72**, 3590 (1994).
- [113] G. Klimeck, Guanlong Chen, and S. Datta, *Phys. Rev. B* **50**, 2316 (1994).
- [114] Guanlong Chen, G. Klimeck, S. Datta, Guanha Chen, and W.A. Goddard III, *Phys. Rev. B* **50**, 8035 (1994).
- [115] K.A. Matveev, *Phys. Rev. B* **51**, 1743 (1995).

- [116] J.M. Golden and B.I. Halperin, *Phys. Rev. B* **53**, 3893 (1996).
- [117] K.A. Matveev, L.I. Glazman, and H.U. Baranger, *Phys. Rev. B* **53**, 1034 (1996).
- [118] J.M. Golden and B.I. Halperin, *Phys. Rev. B* **54**, 16757 (1996).
- [119] M. Stopa, private communication (1995).
- [120] L.W. Molenkamp, K. Flensberg, and M. Kemerink, *Phys. Rev. Lett.* **75**, 4282 (1995).
- [121] C.H. Crouch, C. Livermore, R.M. Westervelt, K.L. Campman, and A.C. Gossard, submitted to *Appl. Phys. Lett.* (1997).
- [122] H.L. Edwards, Q. Niu, and A.L. de Lozanne, *Appl. Phys. Lett.* **63**, 1815 (1993).
- [123] P.A. Lee and T.V. Ramakrishnan, *Rev. Mod. Phys.* **57**, 287 (1985).
- [124] B.L. Altshuler and A.G. Aronov, in *Electron-Electron Interaction in Disordered Systems*, eds. A.L. Efros and M. Pollak (Elsevier, Amsterdam, 1985).
- [125] S. Washburn and R.A. Webb, *Adv. Phys.* **35**, 375 (1986).
- [126] A. Yacoby, M. Heiblum, D. Mahalu, and Hadas Shtrikman, *Phys. Rev. Lett.* **74**, 4047 (1995).
- [127] R. Schuster, E. Buks, M. Heiblum, D. Mahalu, V. Umansky, H. Shtrikman, *Nature* **385**, 417 (1997).
- [128] C.J.B. Ford, M. Field, P.J. Simpson, M. Pepper, D. Popovic, D. Kern, J.E. Frost, D.A. Ritchie, and G.A.C. Jones, *Inst. Phys. Conf. Ser.* **127**, 235 (1992).
- [129] T. Fujisawa, T. Bever, Y. Hirayama, and S. Tarucha, *J. Vac. Sci. Technol. B* **12**(6), 3755 (1994).
- [130] S. Tarucha, D.G. Austing, and T. Honda, *Superlattices and Microstructures* **18**, 121 (1995).
- [131] S. Tarucha, D.G. Austing, T. Honda, R.J. van der Hage, and L.P. Kouwenhoven, *Phys. Rev. Lett.* **77**, 3613 (1996).
- [132] S. Tarucha, Y. Tokura, and Y. Hirayama, *Phys. Rev. B* **44**, 13815 (1991).
- [133] Bo Su, V.J. Goldman, and J.E. Cunningham, *Science* **255**, 313 (1992).
- [134] M. Tewordt, L. Martin-Moreno, J.T. Nicholls, M. Pepper, M.J. Kelly, V.J. Law, D.A. Ritchie, J.E.F. Frost, and G.A.C. Jones, *Phys. Rev. B* **45**, 14407 (1992).
- [135] S. Tarucha, T. Honda, T. Saku, and Y. Tokura, *Surf. Sci.* **305**, 547 (1994).
- [136] T. Schmidt, M. Tewordt, R.H. Blick, R.J. Haug, D. Pfannkuche, K. von Klitzing, A. Foerster, and H. Lueth, *Phys. Rev. B* **51**, 5570 (1995).
- [137] J.W. Sleight, E.S. Hornbeck, M.R. Deshpande, R.G. Wheeler, M.A. Reed, R.C. Bowen, W.R. Frensley, J.N. Randall, and R.J. Matyi, *Phys. Rev. B* **53**, 15727 (1996).
- [138] M.W. Dellow, P.H. Beton, M. Henini, P.C. Main, and L. Eaves, *Electron. Lett.* **27**, 134 (1991).
- [139] P. Gueret, N. Blanc, R. Germann, and H. Rothuizen, *Phys. Rev. Lett.* **68**, 1896 (1992).
- [140] C.J. Goodings, J.R.A. Cleaver, and H. Ahmed, *Electron. Lett.* **28**, 1535 (1992).
- [141] D.G. Austing, T. Honda, and S. Tarucha, *Semicond. Sci. Technol.* **11**, 388 (1996).
- [142] V.R. Kolagunta, D.B. Janes, G.L. Chen, K.J. Webb, and M.R. Melloch, *Superlattices and Microstructures* **17**, 339 (1995).
- [143] A. Groshev, T. Ivanov, and V. Valtchinov, *Phys. Rev. Lett.* **66**, 1082 (1991).
- [144] H. Liu and G. Ayers, *J. Appl. Phys.* **65**, 4908 (1989).
- [145] S. Tarucha, Y. Hirayama, T. Saku, and Y. Tokura, in *Science and Technology of Mesoscopic Structures*, edited by S. Namba, C. Hamaguchi, and T. Ando (Springer-Verlag, Tokyo 1992).
- [146] L.P. Kouwenhoven, R.J. van der Hage, S. Tarucha, D.G. Austing, and T. Honda, (unpublished, 1996).
- [147] M. Macucci, K. Hess, and G.J. Iafrate, *J. Appl. Phys.* **77**, 3267 (1995).

- [148] H. Tamura (private communications).
- [149] V. Fock, *Z. Phys.* **47**, 446 (1928).
- [150] C.G. Darwin, *Proc. Cambridge Philos. Soc.* **27**, 86 (1930).
- [151] L.I. Schiff, *Quantum Mechanics* (MacGraw-Hill, New York, 1949).
- [152] P.L. McEuen, E.B. Foxman, J. Kinaret, U. Meirav, M.A. Kastner, N.S. Wingreen, and S.J. Wind, *Phys. Rev. B* **45**, 11419 (1992).
- [153] R.H. Silsbee and R.C. Ashoori, *Phys. Rev. Lett.* **64**, 1991 (1990).
- [154] G.W. Bryant, *Phys. Rev. Lett.* **59**, 1140 (1987).
- [155] C. de C. Chamon and X.G. Wen, *Phys. Rev. B* **49**, 8227 (1994).
- [156] J.J. Palacios, L. Martin-Moreno, G. Chiappe, E. Louis, and C. Tejedor, *Phys. Rev. Lett.* **50**, 5760 (1994).
- [157] Y. Tanaka and H. Akera, *Phys. Rev. B* **53**, 3901 (1996).
- [158] P.A. Maksym and T. Chakraborty, *Phys. Rev. B* **45**, 180 (1992).
- [159] P.A. Maksym and T. Chakraborty, *Phys. Rev. Lett.* **65**, 108 (1990).
- [160] M. Eto, submitted to *Jpn. J. Appl. Phys.* (1997).
- [161] *Mesoscopic Phenomena in Solids*, edited by B. L. Altshuler, P. A. Lee, and R. Webb (North-Holland, Amsterdam, 1991).
- [162] *Mesoscopic Quantum Physics*, edited by E. Akkermans, G. Montambaux, J.-L. Pichard, and J. Zinn-Justin (Elsevier, Amsterdam, 1995).
- [163] S. Washburn and R. A. Webb, *Rep. Prog. Phys.* **55**, 1311 (1993).
- [164] B. L. Altshuler, *JETP Lett.* **41**, 648 (1985).
- [165] P. A. Lee, A. D. Stone, and H. Fukuyama, *Phys. Rev. B* **35**, 1039 (1987).
- [166] P. A. Lee and A. D. Stone, *Phys. Rev. Lett.* **55**, 1622 (1985).
- [167] B. L. Altshuler and B. I. Shklovskii, *Sov. Phys. JETP* **64**, 127 (1986).
- [168] K. B. Efetov, *Adv. in Phys.* **32**, 53 (1983).
- [169] Y. Imry, *Euro. Phys. Lett.* **1**, 249 (1986).
- [170] H. U. Baranger and P. A. Mello, *Phys. Rev. Lett.* **73**, 142 (1994).
- [171] C. W. J. Beenakker, *Phys. Rev. B* **47**, 15763 (1993).
- [172] R. A. Jalabert, J.-L. Pichard, and C. W. J. Beenakker, *Europhysics Letters* **27**, 255 (1994).
- [173] R. A. Jalabert, H. U. Baranger, and A. D. Stone, *Phys. Rev. Lett.* **65**, 2442 (1990).
- [174] R. V. Jensen, *Chaos* **1**, 101 (1991).
- [175] H. U. Baranger, R. A. Jalabert, and A. D. Stone, *Chaos* **3**, 665 (1993).
- [176] C. M. Marcus, A. J. Rimberg, R. M. Westervelt, P. F. Hopkins, and A. C. Gossard, *Phys. Rev. Lett.* **69**, 506 (1992).
- [177] M. W. Keller, O. Millo, A. Mittal, and D. E. Prober, *Surf. Sci.* **305**, 501 (1994).
- [178] J. P. Bird, A. D. C. Grassie, M. Lakrimi, K. M. Hutchings, J. J. Harris, and C. T. Foxon, *J. Phys. Cond. Matter* **2**, 7847 (1990).
- [179] I. H. Chan, R. M. Clarke, C. M. Marcus, K. Campman, and A. C. Gossard, *Phys. Rev. Lett.* **74**, 3876 (1995).
- [180] R. Ketzmerick, *Phys. Rev. B* **54**, 10841 (1996); H. Hegger, B. Huckestein, K. Hecker, M. Janssen, A. Freimuth, G. Reckziegel, and R. Tuzinski, *Phys. Rev. Lett.* **77**, 3885 (1996).
- [181] R. Akis and D. Ferry, unpublished (1996).
- [182] C.W.J. Beenakker, cond-mat/9612179 (1996); to appear in *Rev. Mod. Phys.*
- [183] K. Efetov, *Supersymmetry in Disorder and Chaos* (Cambridge University Press, Cambridge, 1997).
- [184] M. L. Mehta, *Random Matrices* (Academic Press, Boston, 1991).
- [185] A. D. Stone, P. A. Mello, K. A. Muttalib, and J. Pichard, in *Mesoscopic Phenomena in Solids*, edited by B. L. Altshuler, P. A. Lee, and R. A. Webb (Elsevier, Amsterdam, 1991).

- [186] B. L. Altshuler and B. D. Simons, in *Mesoscopic Quantum Physics*, edited by E. Akkermans, G. Montambaux, J.-L. Pichard, and J. Zinn-Justin (Elsevier, Amsterdam, 1995).
- [187] A. V. Andreev, O. Agam, B. D. Simons, and B. L. Altshuler, *Phys. Rev. Lett.* **76**, 3947 (1996).
- [188] R. A. Jalabert, A. D. Stone, and Y. Alhassid, *Phys. Rev. Lett.* **68**, 3468 (1992).
- [189] V. N. Prigodin, K. B. Efetov, and S. Iida, *Phys. Rev. Lett.* **71**, 1230 (1993).
- [190] E. R. Mucciolo, V. N. Prigodin, and B. L. Altshuler, *Phys. Rev. B* **51**, 1714 (1995).
- [191] Y. Alhassid and C. H. Lewenkopf, *Phys. Rev. Lett.* **75**, 3922 (1995).
- [192] H. Bruus and A. D. Stone, *Phys. Rev. B* **50**, 18275 (1994).
- [193] V. I. Fal'ko and K. B. Efetov, *Phys. Rev. B* **50**, 11267 (1994).
- [194] Y. Alhassid, J. N. Hormuzdiar, and N. D. Whelen, *cond-mat/9609115* (1996).
- [195] P. L. McEuen, N. S. Wingreen, E. B. Foxman, J. Kinaret, U. Meirav, M. A. Kastner, Y. Meir, and S. J. Wind, *Physica B* **189**, 70 (1993).
- [196] A. M. Chang, H. U. Baranger, L. N. Pfeiffer, K. W. West, and T. Y. Chang, *Phys. Rev. Lett.* **76**, 1695 (1996).
- [197] J. A. Folk, S. R. Patel, S. Godijn, A. G. Huibers, S. Cronenwett, C. M. Marcus, K. Campman, and A. C. Gossard, *Phys. Rev. Lett.* **76**, 1699 (1996).
- [198] Y. M. Blanter and A. D. Mirlin, *cond-mat/9604139* (1996).
- [199] S. R. Patel, S. M. Cronenwett, A. G. Huibers, M. Switkes, J. A. Folk, C. M. Marcus, K. Campman, and A. C. Gossard, *Superlattices and Microstructures*, to be published (1997).
- [200] B. D. Simons and B. L. Altshuler, *Phys. Rev. Lett.* **70**, 4063 (1993).
- [201] A. Szafer and B. A. Altshuler, *Phys. Rev. Lett.* **70**, 587 (1993).
- [202] Y. Alhassid and H. Attias, *Phys. Rev. Lett.* **76**, 1711 (1996).
- [203] H. Bruus, C. H. Lewenkopf, and E. R. Mucciolo, *Phys. Rev. B* **53**, 9968 (1996).
- [204] O. Agam, *J. Phys. I (Paris)* **4**, 697 (1994).
- [205] U. Sivan, F. P. Milliken, K. Milkove, S. Rishton, Y. Lee, J. M. Hong, V. Boegli, D. Kern, and M. DeFranza, *Europhys. Lett.* **25**, 605 (1994).
- [206] Y. Alhassid and H. Attias, *Phys. Rev. B* **54**, 2696 (1996).
- [207] K. B. Efetov, *Phys. Rev. Lett.* **74**, 2299 (1995).
- [208] P. L. McEuen, E. B. Foxman, U. Meirav, M. A. Kastner, Y. Meir, N. S. Wingreen, and S. J. Wind, *Phys. Rev. Lett.* **66**, 1926 (1991).
- [209] U. Sivan, R. Berkovits, Y. Aloni, O. Prus, A. Auerbach, and G. Ben-Yoseph, *Phys. Rev. Lett.* **77**, 1123 (1996).
- [210] O. Bohigas, in *Chaos and Quantum Physics*, edited by M. Giannoni, A. Voros, and J. Zinn-Justin (Elsevier, Amsterdam, 1991).
- [211] Y. M. Blanter, A. D. Mirlin, and B. A. Muzykantskii, *Phys. Rev. Lett.* **78**, 2449 (1997).
- [212] G. Montambaux, in *Les Houches, Session LXIII, Quantum Fluctuations*, edited by E. Giacobino, S. Reynaud, and J. Zinn-Justin (Elsevier, Amsterdam, 1996).
- [213] L. P. Levy, G. Dolan, J. Dunsmuir, and H. Bouchiat, *Phys. Rev. Lett.* **64**, 2074 (1990).
- [214] V. Chandrasekhar, R. A. Webb, M. J. Brady, M. B. Ketchen, W. J. Gallagher, and A. Kleinsasser, *Phys. Rev. Lett.* **67**, 3578 (1991).
- [215] D. Mailly, C. Chapelier, and A. Benoit, *Phys. Rev. Lett.* **70**, 2020 (1993).
- [216] K. Richter, D. Ullmo, and R. A. Jalabert, *Physics Reports*, (in press) (1996).
- [217] L. P. Levy, D. H. Reich, L. Pfeiffer, and K. West, *Physica B* **189**, 204 (1993).
- [218] K. Nakamura and H. Ishio, *J. Phys. Soc. Japan* **61**, 3939 (1992).
- [219] F. von Oppen, *Phys. Rev. B* **50**, 17151 (1994).
- [220] D. Ullmo, K. Richter, and R. A. Jalabert, *Phys. Rev. Lett.* **74**, 383 (1995).

- [221] D. V. Averin and Y. Nazarov, Phys. Rev. Lett. **65**, 2446 (1990).
- [222] D. C. Glatli, C. Pasquier, U. Meirav, F. I. B. Williams, Y. Jin, and B. Etienne, Z. Phys. B **85**, 375 (1991).
- [223] I. L. Aleiner and L. I. Glazman, Phys. Rev. Lett. **77**, 2057 (1996).
- [224] S. M. Cronenwett, S. R. Patel, A. G. Huibers, C. M. Marcus, K. Campman, and A. C. Gossard, unpublished (1996).
- [225] E. H. Hauge and J. A. Stovneng, Rev. Mod. Phys. **61**, 917 (1989).
- [226] R. M. Clarke, I. H. Chan, C. M. Marcus, C. I. Duruöz, J. S. Harris, K. Campman, and A. C. Gossard, Phys. Rev. B **52**, 2656 (1994).
- [227] P. Hawrylak, Phys. Rev. Lett. **71**, 3347 (1993).
- [228] I. K. Marmorosk and C. W. J. Beenakker, Phys. Rev. B **46**, 15562 (1992).
- [229] J.M. Kinaret and N.S. Wingreen, Phys. Rev. B **48**, 11113 (1993).
- [230] M. Stopa, unpublished. Note that in this simulation, the two LLs are two *orbital* LLs,  $n = 0$  and  $n = 1$ . The spin splitting is too small to be clearly seen.
- [231] A.A.M. Staring, B.W. Alphenaar, H. van Houten, L.W. Molenkamp, O.J.A. Buyk, M.A.A. Mabesoone, and C.T. Foxon, Phys. Rev. B **46**, 12869 (1992).
- [232] T. Heinzl, D.A. Wharam, J.P. Kotthaus, G. Böhm, W. Klein, G. Tränkle, and G. Weimann, Phys. Rev. B **50**, 15113 (1994).
- [233] N.C. van der Vaart, M.P. de Ruyter van Steveninck, L.P. Kouwenhoven, A.T. Johnson, Y.V. Nazarov, C.P.J.M. Harmans, and C.T. Foxon, Phys. Rev. Lett. **73**, 320 (1994).
- [234] S. R. Eric Yang, A.H. MacDonald, and M.D. Johnson, Phys. Rev. Lett. **71**, 3194 (1993); A.H. MacDonald, S.R. Eric Yang, and M.D. Johnson, Aust. J. Phys. **46**, 345 (1993).
- [235] O. Klein, C. de C. Chamon, D. Tang, D.M. Abusch-Magder, U. Meirav, X.-G. Wen, M.A. Kastner, and S.J. Wind, Phys. Rev. Lett. **74**, 785 (1995).
- [236] J. H. Oaknin, L. Martin-Moreno, J.J. Palacios, and C. Tejedor, Phys. Rev. Lett. **74**, 5120 (1995).
- [237] J.K. Jain and T. Kawamura, Europhys. Lett. **29**, 321 (1995).
- [238] S.E. Barrett, G. Dabbagh, L.N. Pfeiffer, K.W. West, R. Tycko, Phys. Rev. Lett. **74**, 5112 (1995).
- [239] A. Karlhede, S.A. Kivelson, K. Lejnell, and S.L. Sondhi, Phys. Rev. Lett. **77**, 2061 (1996).
- [240] J.H. Oaknin, L. Martin-Moreno, and C. Tejedor, Phys. Rev. B **54**, 16850 (1996).
- [241] O. Klein, D. Goldhaber-Gordon, C. de Chamon, and M.A. Kastner, Phys. Rev. B **53**, 4221 (1996).
- [242] Y.V. Nazarov and A.V. Khaetskii, Phys. Rev. B **49**, 5077 (1994).
- [243] L.P. Kouwenhoven, A.T. Johnson, N.C. van der Vaart, A. van der Enden, C.J.P.M. Harmans, and C.T. Foxon, Z. Phys. B **85**, 381 (1991).
- [244] M. W. Keller, J. M. Martinis, N. M. Zimmerman, A. H. Steinbach, Appl. Phys. Lett. **69**, 1804 (1996).
- [245] P.K. Tien, and J.R. Gordon, Phys. Rev. **129**, 647 (1963).
- [246] N.S. Wingreen, A.P. Jauho, and Y. Meir, Phys. Rev. B **48**, 8487 (1993).
- [247] A. P. Jauho, N. S. Wingreen, and Y. Meir, Phys. Rev. B **50**, 5528 (1994).
- [248] Y. Fu and S. C. Dudley, Phys. Rev. Lett. **70**, 65 (1993).
- [249] L.P. Kouwenhoven, S. Jauhar, K. McCormick, D. Dixon, P.L. McEuen, Yu. V. Nazarov, N.C. van der Vaart, and C.T. Foxon, Phys. Rev. B **50**, 2019 (1994).
- [250] L.P. Kouwenhoven, S. Jauhar, J. Orenstein, P.L. McEuen, Y. Nagamune, J. Motohisa, and H. Sakaki, Phys. Rev. Lett. **73**, 3443 (1994).
- [251] H. Akiyama, H. Sugawara, Y. Kadoya, A. Lorke, S. Tsujino, and H. Sakaki, Appl. Phys. Lett. **65**, 424 (1994).

- [252] H. Drexler, A. J. S. Scott, S. J. Allen, Jr., K. L. Campman, and A.C. Gossard, *Appl. Phys. Lett.* **67**, 2816 (1995).
- [253] B. J. Keay, S. J. Allen, Jr., J. Galan, J. P. Kaminski, K. L. Campman, A. C. Gossard, U. Bhattacharya, and M. J. W. Rodwell, *Phys. Rev. Lett.* **75**, 4098 (1995).
- [254] B. J. Keay, S. Zeuner, S. J. Allen, Jr., K. D. Maranowski, A. C. Gossard, U. Bhattacharya, and M. J. W. Rodwell, *Phys. Rev. Lett.* **75**, 4102 (1995).
- [255] C. Bruder and H. Schoeller, *Phys. Rev. Lett.* **72**, 1076 (1994).
- [256] J.M. Hergenrother, M.T. Tuominen, J.G. Lu, D.C. Ralph, and M. Tinkham, *Physica B* **203**, 327 (1994).
- [257] D. Vion, P.F. Orfila, P. Joyez, D. Esteve, and M.H. Devoret, *J. of Appl. Phys.* **77**, 2519 (1995).
- [258] M.H. Devoret, D. Esteve, H. Grabert, G.-L. Ingold, H. Pothier, and C. Urbina, *Phys. Rev. Lett.* **64**, 1824 (1990).
- [259] T. Holst, D. Esteve, C. Urbina, M.H. Devoret, *Phys. Rev. Lett.* **73**, 3455 (1994).
- [260] Y.B. Zeldovich, *Sov. Phys. JETP* **24**, 1006 (1967).
- [261] C.A. Stafford and N.S. Wingreen, *Phys. Rev. Lett.* **76**, 1916 (1996).
- [262] T. H. Stoof and Yu. V. Nazarov, *Phys. Rev. B* **53**, 1050 (1996).
- [263] M. Holthaus and D. Hone, *Phys. Rev. B* **47**, 6499 (1993).
- [264] M. Yu. Sumetskii and M. L. Fel'shtyn, *JETP Lett.* **53**, 24 (1991).
- [265] R.H. Blick, R.J. Haug, K. v. Klitzing, and K. Eberl, *Surf. Science* **361**, 595 (1996).
- [266] T. Fujisawa and S. Tarucha, *Superlattices and Microstructures*, **21**, 247 (1997).
- [267] D.V. Averin and K.K. Likharev, in *Ref. 3*.
- [268] E.H. Visscher, S.M. Verbrugh, J. Lindeman, P. Hadley, and J.E. Mooij, *Appl. Phys. Lett.* **66**, 305 (1994).
- [269] P. Lafarge, H. Pothier, E.R. Williams, D. Esteve, C. Urbina, and M.H. Devoret, *Z. Phys. B* **85**, 327 (1991).
- [270] J.M. Martinis, M. Nahum, and H.D. Jensen, *Phys. Rev. Lett.* **72**, 904 (1994).
- [271] J.P. Pekola, K.P. Hirvi, J.P. Kauppinen, and M.A. Paalanen, *Phys. Rev. Lett.* **73**, 2903 (1994).
- [272] A.M.M. Staring, L.W. Molenkamp, B.W. Alphenaar, H. van Houten, O.J.A. Buyk, M.A.A. Mabesoone, C.W.J. Beenakker, C.T. Foxon, *Europhys. Lett.* **22**, 57 (1993).
- [273] A.N. Cleland, D. Esteve, C. Urbina, M.H. Devoret, *Appl. Phys. Lett.* **61**, 2820 (1992).
- [274] C.S. Lent, P.D. Tougaw, and W. Porod, *Appl. Phys. Lett.* **62**, 714 (1993).
- [275] E. Buks and M. Heiblum, unpublished (1997).
- [276] I.L. Aleiner, N.S. Wingreen and Y. Meir, *cond-mat/9702001* (1997).
- [277] L.P. Kouwenhoven, *Science* **275**, 1896 (1997);
- [278] O. Agam, N.S. Wingreen, B.L. Altshuler, D.C. Ralph, and M. Tinkham, *Phys. Rev. Lett.* **78**, 1956 (1997).
- [279] J. von Delft, A.D. Zaikin, D.S. Golubev, and W. Tichy, *Phys. Rev. Lett.* **77**, 3189 (1996).
- [280] D.L. Klein and P.L. McEuen, unpublished (1997).
- [281] D. Porath and O. Millo, *J. Appl. Phys.* **81**, 2241 (1996).
- [282] C. Joachim, and J.M. Gimzewski, *Chem. Phys. Lett.* **265**, 353 (1997).
- [283] E.S. Soldatov, V.V. Khanin, A.S. Trifonov, S.P. Gubin, V.V. Kolesov, D.E. Presnov, S.A. Iakovenko, G.B. Khomutov, and A.N. Korotkov, *cond-matter* 9610155 (1996).
- [284] M. Bockrath, D.H. Cobden, P.L. McEuen, N.G. Chopra, A. Zettl, A. Thess, and R.E. Smalley, *Science* **275**, 1922 (1997); and unpublished.
- [285] S.J. Tans, M.H. Devoret, H. Dai, A. Thess, R.E. Smalley, L.J. Geerligs, and C. Dekker, *Nature* **386**, 474 (1997).